Doctoral Dissertation
Doctoral Program in Materials Science and Technology (33th Cycle)

Preparation and characterization of UV-LED curable composite systems based on carbon fillers

Valentina Strongone

* * * * * *

Supervisors
Prof. Giulio Malucelli, Supervisor
Prof. Alberto Tagliaferro, Co-Supervisor

Doctoral Examination Committee:
Prof. ssa Veronica Ambrogi, Referee, University Federico II of Napoli
Prof. Daniele Caretti, Referee, University of Bologna
Prof. ssa Emma Angelini, Referee, Politecnico di Torino
Prof. Jean Marc Tulliani, Referee, Politecnico di Torino
Prof. Andrea Castrovinci, Referee, Scuola universitaria professionale della Svizzera italiana (SUPSI)

Politecnico di Torino
February 16, 2021

I hereby declare that, the contents and organisation of this dissertation constitute my own original work and does not compromise in any way the rights of third parties, including those relating to the security of personal data.

……………………………….....

Valentina Strongone

Turin, February 16, 2021

Abstract

In the present dissertation, UV-LED curing technology is exploited to design coating composites with advanced properties. As eco-friendly, inexpensive and high operating efficiency process, UV-LED curing technique represents a valid alternative to conventional thermal curing methods. In fact, UV-LED photo-induced polymerization shows several advantages, such as low operational costs and time and energy saving, notwithstanding that UV-LED units emit "cold" radiation. Since its innovative features, UV-LED curing technology is exploited for producing added-value composite coatings obtained by the incorporation of carbon fillers in epoxy-acrylate curable resin containing a specific photo-initiator. Thanks to their physical and chemical characteristics, carbon fillers provide advanced properties to insulating acrylic resin. Among carbonaceous materials, Biochar and multi walled carbon nanotubes (MWCNTs) are selected to improve the rheological, thermal, electrical and optical properties of the thermosetting matrix. As bio-sourced product, Biochar is an inexpensive and environmentally-friendly material that has a remarkable importance within the circular economy, based on recovery and reuse of biomass wastes at the end of their life. Among biomass residues, spent coffee grounds are the main industry waste worldwide. Besides, as the most popular beverage in the world, its consumption increases year by year with a consequent huge amount of generated solid waste. Spent coffee ground constitutes about 90% of brewed coffee: because of its high lignocellulosic composition, exhausted coffee residue may become a resource when it is converted into Biochar through pyrolysis. The use of the Biochar as a filler in polymeric composites is due to its high carbon content that has a significant effect on the mechanical, thermal and electrical properties of the host material. Furthermore, thanks to its morphology and structure, the Biochar is suitable to promote the dispersion of MWCNTs in a polymer matrix. As the low level of dispersion of MWCNTs in thermosetting resin limits the application of these nanofillers, the shuttle effect of Biochar was exploited for obtaining acrylic composite coatings. The combination of Biochar and MWCNTs in acrylic resin

may results into a synergistic effect: the Biochar promotes the dispersion of MWCNTs, hence allowing the optimization of the overall performances of the composite materials.

In order to design the UV-LED composite films, a suitable curable mixture, containing the photo-initiator and the epoxy acrylic resin, was prepared. Then Biochar and/or MWCNTs were incorporated, both as single and mixed fillers, through sonication at different loadings, ranging from 0.01 to 1.0 wt.%. The liquid dispersions, coated on a glass plate, were subjected to the UV-LED curing to obtain a three-dimensional fully cured network in few seconds.

The UV-LED composite films were characterized to investigate the effect of the filler type and loading on the effectiveness of the UV-LED curing process and on the rheological, thermal and optical properties of the cured composite films. While the fillers did not compromise the effectiveness of the curing process, leading to the obtainment of fully cured composite networks, the properties of the UV-LED composite films were strictly dependent on the filler size and shape. In particular, the morphology of Biochar and MWCNTs affected the filler-polymer interface, which the properties of composite films depend on. For this reason, in this dissertation, the morphological and rheological analyses were fundamental to investigate the correlation between the structure and properties of the UV-LED composite films, as well as the shuttle effect provided by Biochar.

Acknowledgment

I would like to thank my supervisor, Professor Giulio Malucelli, his knowledges and ideas have been fundamental to carry out this research project. I am grateful to the Carbon Group of Politecnico of Turin for the contribution apporting to the experimental part of this work.

Great thanks to all my colleagues at Politecnico for their scientific suggestions during these years. Last, but not least, I would like to express deep gratitude to my boyfriend Alessandro and my family, whom support was essential to achieve this result.

Alla mia Famiglia

Contents

List of Tables

List of Figures

Chapter 1

State of the art

1.1 Introduction to UV-LED curing

Ultraviolet (UV) curing technique represents an important transformation process for thermosetting polymers, which, apart from thermal curing processes performed in the presence of selected curing agents, can be successfully converted into a 3D network through the exposure to UV-light, necessary to trigger photo-polymerization reactions. A key component of an UV-curable formulation is the photo-initiator (PI) that, through the absorption of UV-radiation, gives rise to some activated species, from which the polymerization reactions can take place. It results from above any UV-curing system consists of just few components, namely: UV-lamp, base liquid thermosetting resin, photo-initiator and possible additives to give some targeted properties. The simplicity and compactness are two mainly characteristics of a UV-curing system that offers many other advantages related to costs, performance and environmental impact [1,2].

The curing by UV radiation is a consolidated technology both at laboratory and industrial scale; it has been established over the last decades as it keeps up to date in comparison with the thermal curing technique. The success of light-induced technology, as compared to the thermal one, refers to some advantages in terms of saving time, as photo-induced reactions take place in few seconds, and saving money, as the UV-curing process needs low energy consumption since photo-polymerization occurs at ambient temperature and doesn't require the removal of volatile organic solvents (VOC) [2,3]. In this context, UV-curing is considered an effective process to obtain high cross-linked networks using the least waste of energy and avoiding the release of VOC in the atmosphere. This latter aspect is important: in fact, UV-curing doesn't cause significant harm to environmental and human health; the amount of solvent that enters in atmosphere is close to zero, hence preventing the operator from the inhalation and contact with dangerous volatile organic compounds [2].

Over the years, the UV-curing technique has undergone changes connected to the evolution of light sources as chemical excitation for the curing of the resin system. The recent development of LEDs (light emitted diodes) has involved the lighting technology, where traditional high-power arc light sources, such as ultraviolet (UV) mercury (Hg) lamp, were replaced with novel *ultraviolet light emitted diodes* (UV-LEDs), a solid state sources. Many advantages are connected with the introduction of UV-LEDs in photo-curing processes: indeed, they combine the long operating lifetime and more stable light intensity with the concept of environmental and human health protection [4-6].

Although early Hg arc lamps match the spectral output features of equipment (namely, radiation power, wavelength output, dose, efficiency, depth cure) to PI absorbance mechanism, LEDs marked a real innovation in UV-curing technology and allow overcoming several limitations of pressure vapor lamps [5,7,8].

The generation of UV energy is based on the emission of photons through the decay of electrons from an exited higher energy state to their original ground state orbital. While, in traditional UV-lamps, the generation of photons is due to the excitation of Hg electrons by an electric arc inside the ionized gas in a quartz tube, in UV-LEDs the energy is produced by an electric current that moves through a semiconductor device (diode). Therefore, LEDs are safety devices because they don’t contain mercury that is conversely present in arc lamp and is excited by electrodes, which in turn are subjected to deterioration during the switching on-off. Besides, this process is responsible for the reduction of lifespan of the bulb, together with the high temperature reached inside the tube: when the gas is ionized and the arc is struck, the operating temperature is between 600 and 800°C. This means that much of the energy produced by the lamp (about 50%) is wasted as heat, which could affect the final cured product, especially in sensitive substrate causing degradation, distortion and curl in plastics [5,9].

The generation of heat is an undesirable effect not only for photo-curing process but it is also harmful for human and environmental health, as the heat generated is in form of infrared (IR) energy: in fact, the emitted light covers a wide range of electromagnetic spectrum including short wave (below 250nm) that could irradiate the oxygen present in the air and generate ozone, a toxic gas.

Thanks to LEDs technology, the desired properties of the final products are combined with a higher energy efficiency, more constant light intensity, longer lifetime and no heat production.

These advantages are connected to LEDs construction: the diode is a p-n junction (positive-negative junction) made of a thick semiconductor, whose selection determines the light emission. While a traditional UV lamp emits in a broad wavelength range, LEDs output have narrow wavelength focused in UV-A range [9,10]. The monochromatic output line in UV-A range is, at the same time, advantageous for UV-curing purpose, as it is responsible for depth cure; it is safe both for the operator, and for environment as well, as it doesn’t produce ozone. This is beneficial for LEDs devices because the light emission at long waves doesn’t lead to an overheating of the lamp [3,5]. For these reasons, UV-LEDs, unlike traditional UV-lamps, don’t require complex cooling systems, have long lifetime, low power consumption and can be used for curing on heat-sensitive substrates. Furthermore, the complete curing, associated with the lack of tackiness in cured surfaces, suggest that UV-LEDs can be used as alternative to conventional light sources both in medical and industrial applications, getting ease, efficiency and productivity in curing process.

1.2 UV-LED curing applications

1.2.1 Medical application

UV-LEDs have recently had success in dentistry, a medical area in which the introduction of photo-curing dental material, in the middle of last century, was considered a revolution. UV curing in dentistry is a valid technology to restore caries and to repair tooth fracture, promoting the "cure on demand" feature with respect to the early self-cure system [11]. The first photo-curing system was based on UV high pressure mercury lamps as light source operating in the visible range and benzoin ether-type compounds as photo-initiating systems. Although its remarkably success, this process had some drawbacks related to light source: the light from Hg lamp doesn't allow the depth cure and its short wavelength energy can have harmful effect on eyes and on oral micro-flora. Over the years many changes have involved both light sources and curable formulations, but just with the introduction of LEDs few decades ago safety and depth cure requirements are fulfilled: the use of a "cold source" minimizes the heating of the tooth and the pulp, at same time leading to an effective curing and promoting "photo-bleaching" (the products are more transparent than initial PI) that is advantageous for esthetic effects. Curable formulation contains most often camphorquinone (CQ) as photo-initiator, an amine (A) as co-initiator and an acrylate mixture as dental binder resin [1,12-14].

Furthermore, in the medical field, particular attention is paid to the curable formulation, aiming at increasing the mechanical properties and biocompatibility between tissue and light curable resins, reducing shrinkage, promoting re-mineralization and inhibiting bacterial growth [15-19].

Studies have demonstrated that inorganic particles like silica added to dental composites can be exploited for increasing curing rate by light scattering and for reducing the shrinkage. Nano-silica and porous silanized diatomite as co-filler can improve mechanical properties (mechanical strength, elastic modulus and micro-hardness) of cured mixture [18]. Ag nano-crystals functionalized with oleic acid allow overcoming poor dispersion of inorganic antibacterial agents like TiO_2-particles into acrylate resins [18,19]. A challenging issue is to find an equilibrium among components in order to get mechanical, optical and antibacterial properties in a cured composite [15-20].

1.2.2 Industrial applications: coatings, printings, inks, adhesives

Thermosetting polymers are widely used in curing for coatings, printing inks and adhesives in engineering and industrial applications.

The advantages associate with LEDs in curing technology are significantly evident at an industrial scale, where the goal of saving money and time combined with environmental and human safety is pursued daily; therefore, UV-LED curing has a commercial relevance as it allows extending the photo-induced process to heat sensitive substrates, e.g. wood and glued veneers.

The quickly diffusion of thermosetting polymers derives from some intrinsic properties (e.g. easy processing, solvent, creep and high temperature resistance) and, at the same time, thanks to the affinity for heterogeneous materials, the possibility to get particular properties, hence tailored products: the base resin can be modified on purpose [21-27].

Coatings

The role of coatings is crucial in finishes with the aim to protect, decorate or make functional the surface of a final product for the automotive, electronic industries and domestic appliance.

Polymer-based nanocoatings attract great attention for their targeted properties and are subjected to continuous developments to improve mechanical, physical, thermal and chemical characteristics. To this aim, the addition of inorganic fillers (from macro-size to nano-size level) in polymeric resins can lead to the design of multi-functional coatings that perform different activities and are employed for anti-bacterial, optical and energy applications.

Wang et al. in a recent work designed and fabricated a long-term antibacterial wall coating for interior decoration. To this aim, silver nanoparticles (AgNPs) were added to the coating formulation consisting of acrylate resin, photo-initiator and reactive diluents. This precursor composite solution was first subjected to a stirring process, then was coated on the wall surface and exposed to the fast UV-LED curing (emission at 365 nm) for 6 s. As compared with the unfilled system, the coating with AgNPs showed a high antibacterial rate beyond 99.5% for *S. aureus* and 97.0% for *E. coli*. The long-term antibacterial activity was proved repeating the experiment at 12 h intervals, replacing fresh bacterial solution for 15 weeks: it was demonstrated that AgNPs nanocoatings are suitable for the application in wall base coatings [3].

The use of AgNPs as antimicrobial agent in nano-coatings was also investigated by *Asmussen et Vallo*, who exploited the *in-situ* generation of metal nanoparticles method in the polymer matrix in order to avoid AgNPs aggregation sites. The AgNPs synthesis was carried out through a two-phase method, in which a solution of silver nitrate ($AgNO_3$) in ethanol was mixed with a solution of pentaerythritol tetra (3-mercaptopropionate) (PETMP) and 2,6-di-tert-butyl-p-cresol (BHT). The resulting colloidal dispersion was stirred and placed in an oven at 70°C to ensure the evaporation of volatiles: when the reaction started, the silver cations were reduced by BHT. After 24 h, AgNPs in tetrafunctional thiol PETMP were mixed with a bi-functional methacrylate monomer (BisEMA); the final system had a stoichiometric ratio of 2:1 between thiol (-SH) and ene (-C=C) functional groups. For the purpose of obtaining silver-based nanocomposite coating, AgNPs thiol-ene system was subjected to a UV-LED curing using 1% of 2,2-dimethoxy-2-phenylacetophenone (DMPA) or 1% camphorquinone (CQ) as photo-initiators. According to the type of photo-initiator, two LED lamps emitting at 365 nm and 470 nm were employed respectively for DMPA and CQ. Before the exposure to UV-LED radiation the uncured composite resin was placed in a rubber gasket material between two glass plates so that the thickness of the final coating was set at 2 mm. The cured coatings were characterized through Raman analysis to investigate the effect of photo-initiator on curing process: the AgNPs coating with CQ was more cured than the system obtained with DMPA. This behavior was ascribed to the presence of AgNPs whose surface resonance (< 400 nm) overlapped with UV-LED band emission at 365 nm: this way, a part of UV-LED radiation was absorbed by AgNPs and was not available for the curing process. Conversely, when CQ was selected as photo-initiator, the UV-LED spectral emission at 470 nm was greater than AgNPs absorption band: in this case, the photo-initiator, absorbing most of the visible wavelength range, allowed the curing process to reach completeness. Despite the antimicrobial effect provided by AgNPs, the final nano-coating showed limited applications due to the instability and strong odor of thiols contained in starting curable system. In this context, much interest is being drawn towards thiol-ene photo-induced polymerization, thanks to some related advantages [28]. *Hoyle et al.*, in an interesting work, extensively investigated the curing reactions of thiol-ene mixtures, which do not require the use of a photo-initiator to trigger the photocuring process [29]; as explained by *Zonca et al.*, the photo-induced reactions, in which thiol-ene groups participate are both efficient and fast also in presence of oxygen, which can inhibit this type of reactions. Therefore, as compared with thiols and enes, the hybrid group can undergo more reactions, hence resulting versatile towards different substrates and applications. The same authors studied, in particular, a hybrid system based on acrylate and ester monomers, demonstrating that the use of long wavelength UV-LEDs as light source and Irgacure 784 as photoinitiator are the best conditions for the thiol-ene photo-curing reaction [30].

The interest in “smart coatings” is growing quickly in engineering field where polymeric composite materials are already used in manufacturing of complex components to replace metals.

Electrical conductivity is a requirement of coating films that arouses increasing interest in the engineering sector. For this reason, carbonaceous materials are frequently chosen as filler in polymeric matrix in order to make an insulating film electrically conductive. In particular, *Loginos et al.* studied coating films obtained by the combination of two different carbonaceous fillers (Graphene and CNTs) with poly (ethylene glycol) di-acrylate (PEGDA). The curable mixture, consisting of photo-initiator (Irgacure D2959), PEGDA and carbon nanofiller, was stirred for

3 h and cured using UV radiation at 365nm. Despite 2D graphene is more conductive than 1D CNTs, measurements of electrical conductivity revealed that in general PEGDA/CNTs is more conductive than PEGDA/graphene: the latter is prevented in movements within the curable system, hindering the formation of interconnections that, at variance, are present in CNTs composites [31].

In addition to energy goals, some coatings have the purpose of protecting surfaces from oxidation. This object was investigated by *Malucelli* that in a recent work designed a smart nanocomposite coating with oxygen barrier properties using the UV-LED radiation: the addition of cloisite 30B to an acrylic curable system was effective not only for increasing oxygen barrier properties but also for enhancing the thermal stability of the obtained coatings [32].

Printings, inks and adhesives

The conversion from a standard mercury arc lamp system to LED technology can involve other industrial sectors for the production of printings, inks and adhesives. The application of UV-LED curing for the production of adhesives was recently investigated by *Hubert et al.* that pointed out the effectiveness of UV-LED radiation on the curing of acrylic adhesives [33].

UV-LED radiation is also suitable for curing low-viscosity resins such as UV and water-based inks considered by *Zhang et al.* as a “new green printing material” because of low content of VOCs and the use of ethanol and water as solvents. The authors in particular studied a curing system consisting of a UV-LED machine and epoxy acrylate resin whose gloss, viscosity, adhesion and UV curing time revealed its suitability as ink-jet ink [34].

1.2.3 UV-LEDs curing: up to date technologies

UV curing is a process behind “3D printing”, a technology that allows obtaining, by digital control, three-dimensional objects through the layer-by-layer deposition of an UV curable resin [35].

Among the Additive Manufacturing (AM) techniques, stereo-lithography (SL) is being widespread applied. It is based on rapid prototype of a 3D manufacture that is first digitally sectioned into thin layers and then fabricated depositing and UV-curing each layer of resin that makes up the object [36].

The benefits connected to the use of LEDs radiation in SL curing process have been investigated by *Xie and Li*: they evaluated the advantages of LEDs device in terms of running cost and performance. The authors employed a SL system that consists of a LED lamp emitting at 365 nm, whose high radiance ensures a depth cure comparable to that of the lasers, whereas low energy consumption of LEDs allows conforming SL to the *Green Manufacturing* concept [37]. Another study by *Kang and Shin* on micro-stereolithography highlighted the effectiveness of LEDs as alternative to expensive lasers in curing 3D structures [38].

In the last two decades, novel AM techniques based on curing process of composite materials have been developed. Few years ago, *Cunico and Carvalho* have defined a new technology for the production of 3D acrylic-cellulose based products. This innovative method relies on the deposition of different laminated cellulose layers that, coated with a curable resin, are irradiated by UV-LED radiation so that each substrate can adhere to the previous one. Every layer is a composite, whose deposition process ends when the final 3D product is obtained. The study revealed that the exposure to LEDs radiation with an intensity of 120 mW for 60s was sufficient to convert the acrylic polymer, whereas residual material was removed [39].

The innovation in 3D technology has allowed processing, in addition to thermoplastic and thermosetting polymers, ceramic materials such as carbides, borides and oxides. Thanks to their thermal and chemical properties, ceramic components are frequently required in various sectors, from aerospace to biomedical applications. In these areas complex 3D parts are often needed, such as scaffolds with specific porosity and structure. To meet these requirements AM techniques have been developed in order to obtain tailored ceramic elements with significant advantageous also in terms of fabrication costs by shortening the production chain. The evaluation of AM as alternative to conventional techniques such as Gel Casting and Ceramic Injection Molding (CIM) was carried out by *Faes et al.*, who proposed a novel AM for the processing of zirconium dioxide (ZrO_2). This innovative technique combines the extrusion process with UV-LED curing: a mixture of ceramic powder in a UV curable resin was deposited by means of syringe extrusion and then was cured using a UV-LED source at 400 nm [40].

Similarly to AM techniques, also the synthesis of monoliths has been affected by the introduction of UV-LED lamps. The latter were employed for the first time to fabricate a monolithic micro-column in a section of chip by *Abele et al.*: to this aim, a UV-LED lamp emitting at 255 or 370 nm was utilized for curing monoliths methacrylic based within channel of microfluid chips and capillaries made of silica [41].

1.3 UV-LEDs coating line

Coating of commercial end-products is one of UV curing applications where the introduction of LEDs lamps has found more success.

The type and the thickness of the substrate depends on its functionality and can affect the overall UV-curing process. Besides, thanks to LEDs lamps, the cure can involve different types of material such as paper, plastics, circuit boards and more heat sensitive substrates such as wood [2,42].

UV curing systems stand out from other conventional coatings techniques for the efficiency of their coating line, where multiple operations can be automated and performed simultaneously, hence increasing productivity and saving time. The automation takes place in production lines using spray guns, curtain coaters or electrostatic system that are able to dose the exact amount of curable material to cover a specific surface substrate of finishes. In general, robotic systems, frequently used in automotive industry, are equipped with a UV-LEDs lamp in order to cure also 3D objects with some complex components otherwise difficult to produce [43].

The 2D curing line, typical of coating for wood panel industry, consists of one or more units of UV-LEDs lamps connected to a conveyor belt, on which the panel, coated with a chemical formulation, rolls and at the same time, is exposed to UV radiation. The latter affects the depth and the degree of cure: the wavelength, irradiance and energy density are radiation outputs, which the curing performance depends on [2].

1.4 Exposure process

UV-LEDs light exposure factors through radiometric measurements allow evaluating the deposition and the interaction of light at the surface and within of the curable film. The physical factors of UV radiation play an important role in the absorption process of PI and they affect the final characteristics of resulting coatings [44].

During the curing process, UV-LEDs radiation outputs to consider comprise:

- **Wavelength (nm)**, a narrow monochromatic peak focused between 365 nm and 405 nm;
- **Irradiance (Watt/cm^2)**, the radiant power that reaches the curable surface and starts the photo-polymerization reactions; it depends on the distance of the lamp from the coating material;
- **Energy density (Joules/cm^2)**, i.e. the radiant energy that reaches the coating surface; it increases with increasing the number of diodes of the LEDs lamp or the overall irradiation time.

These parameters, together with the spectral absorbance of PI, the thickness of coating film and the presence of filler, influence the UV energy absorption process. The latter is the first step of photo-induced reactions; it consists of a series of energetic states, from which free radicals are generated after the absorption of UV radiation by the PI. The most efficient conversion of UV energy by a PI corresponds in the absorbance spectrum to one or more absorption peaks at different wavelengths: one of these peaks needs to match with that of the LEDs lamp. After the absorption of UV light, PI generates free radicals from a triplet state obtained in turn from a decay process of high-energy singlet state [44,45].

The absorbance of UV energy at long wavelengths is associated with the excitation from n to $\pi *$ bonding orbitals and it is proportional to concentration (c), film thickness (d) and molar absorption coefficient (ε) according to the Lambert-Beer law:

$$A = \varepsilon \, c \, d$$

Since the equation correlates the light penetration depth with the composition of the curable mixture, it allows verifying the output wavelengths suitable to ensure the complete cure of the coating mixture. Indeed, the penetration depth of the light through the film depends on the additives (i.e. pigments, fillers, binders) that, present in the curable mixture, could compromise the completeness and effectiveness of the curing reaction [45].

1.5 Mechanism of UV curing reactions

From the chemical point of view, the UV curing process is based on a chain polymerization mechanism that begins with the absorption of UV energy by the chromophore contained in the structure of the photo-initiator.
The most common chromophore is the aryl ketone group shown in figure 1.1, which generates free radicals from a triplet excited species.

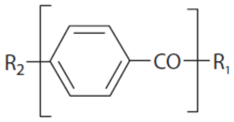

Figure 1.1. Aryl ketone group. Reprinted with permission from [5]. Copyright (2010) with permission from Taylor & Francis Group LLC.

The reaction mechanisms, from which the radicals are formed, depend on the R_1 substituent of PI: when R_1 is an alkyl group, the first type of PI forms two radicals through the cleavage of C-C bond in α or β position; when R_1 is an aryl group, the Type II of PI generates radicals through an abstraction process. The reason is that while in the first case, UV light energy (70-80 kcal/mol) can split C-C bond of CO-alkyl group (65–70 kcals/mol), in the second case it is insufficient to cleave CO-aryl bond energy (80–90 kcal/mol). In this process, PI forms radicals only when the excited triplet species react with a hydrogen donors from ethers, thiols, tertiary amines, producing a ketyl radical at low reactivity and a donor radical at high reactivity.
In both mechanisms, the formation of radicals can be hindered by the oxygen that reduces the exited species to a ground state with loss of energy. Type II PI is more subjected to the oxygen deactivating process, since the longer lifetime of exited state allows the reaction with hydrogen donor but at same time increases the probability of quenching reactions.

$$P^* + O_2 \rightarrow P + O_2^* \rightarrow O_2 + \text{heat}$$

The generation of free radicals corresponds to the initiation process of photopolymerization. This step includes both the absorption of UV radiation by PI and the reaction of free radicals with monomers and oligomers. The latter, in turn, become reactive species and part of growing polymer chain in the subsequent propagation step. The polymer chain stops growing when the radicals interact to form neutral species in the termination process [5].

Chapter 2

Fillers

2.1 Introduction to fillers

The development of composite materials with advanced properties has great relevance especially in the industrial field. Inorganic fillers are added to thermosets aiming to enhance specific properties of polymer matrix and extend its potential applications [24,46]. A wide range of fillers including silica, alumina, zinc oxide, graphene, carbon fibers and metallic filler can be employed for enhancing thermal [48] and electrical [49] conductivity, mechanical [50,51] and flame retardant properties [52,53] of thermosets. The final characteristics of composites are mainly affected by interfacial interactions occurring between filler and polymer matrix. As particle size decreases, the interaction between polymer and filler increases with consequent improvement of dispersion and reinforcement properties [54-58]. The interaction region is defined as the interphase [24], whose thickness depends on the flexibility of polymeric chains. On one hand, a thin interphase region could be attributed to the high flexibility of polymeric chain that are able to form many anchor sites on particle surfaces. On the other hand, rigid polymer chain could form entanglements sites that increase the thickness of the interphase around the fillers [24]. In addition to the size, also morphology [59], geometric arrangement [60] and dispersion state [61] affect the physical interactions, the structures at microscopic level and therefore the final performance of the thermosetting composites. Furthermore, the control of microstructure also depends on the techniques employed for dispersing the fillers in thermosets [24]. The compounding techniques of thermosets can be divided in top-down and bottom up approaches. The top-down procedure consists of reducing of particle size before dispersing the filler in thermosetting resin by shear forces, aiming at prevent the formation of agglomerates. The bottom-up approach leads to the formation of a second phase directly in the thermosetting matrix, this method ensures a greater control on the interaction between polymer chain and filler surface [24].

The top-down approach is exploited in the *solution intercalation* method, where a soluble polymer is added to a liquid medium containing the filler. After the solvent evaporation, the mixture is subjected to the curing process.

In situ polymerization method involves the bottom-up approach: in this case, the dispersion of the filler in a polymeric resin is provided by the reaction of oligomers and monomers with the active centres located on the filler surface. After the addition of PI to the mixture, the photopolymerization process is induced [24,62].

In both approaches, the preparation of curable composites involves the use of calendering, ultrasonication and high-speed stirring techniques that are able to generate shear forces sufficient to disperse the fillers in the thermosetting resin. Depending on the type of filler, the processing techniques may exert a significant role on the final properties of composites [63,64]. In other cases, the contact between carbon fillers is necessary to form a percolated structure, where an electric conductive path between nanoparticles is necessary to increase the electrical conductivity of thermosetting resin [65].

The addition of carbon nanofillers, such as carbon nanofibers (CNFs), could bring to a rise in viscosity leaving the curable mixture difficult to process; thus, a dilution step of the prepolymer in a solvent before dispersing the nanofiller in the curable mixture becomes necessary [24].

Carbon fillers with high surface/volume ratio like carbon nanotubes (CNTs) can be chemically functionalized to prevent the formation of aggregates and to facilitate the dispersion within the curable mixture [66,67]. Ultrasonication, thanks to the high shear forces generated by ultrasound waves, is proposes as technique for dispersing MWCNTs in thermosetting resin [68].

An intercalative polymerization can be adopted for dispersing graphene in curable resin; sonication or mechanical mixing techniques are employed to facilitate the intercalation of prepolymer between graphene sheets [69].

2.1 Carbon based materials

Carbon-based materials adopted as filler in thermosetting resins allow designing tailored materials with advanced properties [70]. Such carbon-based composites combine the advantages of both thermoset and carbon filler and are now widely applied to materials engineering and several industrial fields. In electronic industry, thermosets reinforced with carbon fillers are exploited to fabricate high flexible sensors, hardware components or semiconductor encapsulated devices [70,71].

The mechanical, thermal and electrical properties of carbon materials depend on the atomic surface tension that involves the change of bond lengths in the crystalline structure [70].

Carbon-based materials, classified according to the structural dimension, are briefly presented below.

Graphene has two dimensional (2D) hexagonal honeycomb structure formed by carbon atoms sp^2 hybridized, with a C-C bond length of 0.142 nm [71]. Graphene can be rolled and stacked respectively into one-dimensional (1D) nanotubes and three-dimensional (3D) graphite. The use of graphene in engineering applications is due to its high thermal conductivity (5000 W/m K) [72], high Young modulus (1 TPa) [73], high carrier mobility (250000 cm^2/V s) [74] and high surface/volume ratio [75].

Graphite is obtained by stacking layer-by-layer graphene sheets and is characterized by interlayer spacing of 0.335 nm, smaller than graphene (0.34 nm) [71]. Since the presence of metal bonding, each stacked layer has excellent thermal and electrical conductivity in plane and poor electrical and thermal conductivity across the plane due to the van der Waals forces between the layers [76].

Carbon nanotubes (CNTs) are nanomaterials, in which carbon sp^2 hybridized atoms arrange in hexagonal shape to form a cylindrical structure, in which hexagonal graphene sheets are packed. Depending on the single or multi rolled graphene layer, CNTs can be classified as single walled carbon nanotubes (SWCNTs) and multi walled carbon nanotubes (MWCNTs), respectively.
The strong covalent bond between carbon atoms into graphene packed sheet and the weak van der Walls interactions between graphene layers are responsible for excellent mechanical properties such as tensile strength. The delocalization of valence electrons in π orbitals justifies the high electrical conductivity of CNTs [71].

Carbon nanofibers (CNFs) are characterized by stacked graphene layers to form conic structures. Due to high aspect ratio (250-2000), CNFs form a conductive path also at low percolation threshold. In addition to the electrical conductivity, CNFs show high thermal conductivity (1950 W/m K) and excellent mechanical properties with high tensile modulus and tensile strength, respectively of 240 and 2.92 GPa [71,77].

Carbon black (CB) is a carbonaceous material and derives from the incomplete combustion of liquid and gaseous hydrocarbons. The particles of carbon black, thanks to their high surface area (1000 m^2/g) and density close to 2.25 g/cm^3 are widely employed as additives for some commercial products such as sensors, tires, pigments, supercapacitors and batteries [71].

Biochar is a carbon-based material obtained by pyrolysis or carbonization of lignocellulosic biomass at high temperatures. Biochar is a porous and chemically stable material characterized by high percentage of carbon that arranges from graphite-like structure to aromatic hydrocarbons rings. The electrical conductivity of Biochar depends on carbon content that in turn is affected by the type of biomass, pyrolysis condition and the degree of carbonization [78-84].

Among carbon materials, Biochar exhibited a rising scientific interest in the last decade due to its eco-friendly and inexpensive nature [85]. However, the application of Biochar-based composites is still marginal to develop value-added material. In the following sections, Biochar and MWCNTs will be argued with the aim to compare an emerging sustainable material to a conventional carbon filler obtained from non-renewable sources.

2.2 Biochar

Biochar is an eco-friendly and low-cost carbon-rich material obtained by thermochemical conversion of biomass, an energy and carbon clean source. Nowadays, biomasses are considered as renewable resources as they derive from horticultural, agricultural, forest and food waste [77,79-81]. As a recovery product, any biomass has significant role in the implementation of the circular economy concept, based on the recycle and reuse of resources at the end of their life. The reuse of biomass allows reducing volume waste and producing renewables combining the environmental sustainability to the economic benefits [82-84].

Biomass is a sustainable alternative to fossil fuel for the production of chemicals (bio-diesel) and energy (bio-syngas) by pyrolysis, a thermochemical process, from which Biochar is obtained as co-product. Pyrolysis occurs at high temperatures and leads to the thermal decomposition of biomolecules (cellulose, hemicellulose and lignin) that compose the biomass. Since feedstock material has a lignocellulosic composition, Biochar is characterized by high carbon content and some percentage of hydrogen, oxygen and minerals [77,82-84]. For its chemical and physical properties, Biochar can be used for different purposes, ranging from energetic applications to environmental protection. Biochar is widely applied on soil amendment thanks to alkaline pH, cation exchange capacity (CEC) and the presence of nutrients like potassium (K), calcium (Ca), sodium (Na), magnesium (Mg). Recently, Biochar is employed also in environmental mitigation field, as it is effective in removal of organic and inorganic contaminants in water for its sorption capacity. Besides, thanks to electrical conductivity, Biochar is investigated as alternative to graphene and carbon nanotubes in energy storage [86-94].

Biochar is a high value material whose application strictly depends on process parameters, including heating rate and temperature. For this reason, the evolution of Biochar during pyrolysis process is important to define the application field. At the end of pyrolysis process, Biochar is different from the feedstock material in terms of physical and chemical properties: surface area, morphology and crystallinity considerably change during thermochemical conversion [77,95].

The physical structure of Biochar is significantly affected by pyrolysis temperature: surface area of Biochar may increase dramatically up to two orders of magnitude with respect to feedstock material. Before pyrolysis process, surface area of biomass ranges from 0.1 to 3.2 m^2/g, due to the presence of natural channel pores for the transmission of nutrients in the plants [96,97]. From 400 to 900°C Biochar is subjected to significant increase of surface area. At these temperatures, the high surface area of Biochar is connected to the increasing of porosity due to the removal of volatiles at higher temperature: surface area can reach 500 m^2/g, depending on the type of biomass and operating temperature [85]. Above 900°C melted ash may occlude pores and causes the decrease of surface area. *Chen et al.* investigated the structural evolution of cotton stalk during pyrolysis process: above 950°C, the decrease of surface area is due to the release of vegetable tar and plasticity of solid char that cause the occlusion of micropores. Furthermore, Raman analysis revealed that the decreasing of surface area at high temperature is mainly due to the conversion of Biochar from amorphous structure to crystalline graphite, characterized by low porosity and low surface area [98]. These results were consistent with those reported by *Zeng et al.*, who studied the surface area of beech wood during pyrolysis process from 600 to 2000°C. They named *"intensifying volatile released"* the process from 800 to 1200°C that caused the increase of surface area up to 110.2 m^2/g. Above 1200°C, "*thermal deactivation process*" led to the decrease of surface area up to a minimum value of 22.2 m^2/g at 2000°C, as small grains emerged and macropores on char surface disappeared [99].

Fu et al. investigated the structural evolution of maize stalk during pyrolysis process from 200 to 900°C. They found that the deactivation process occurred at lower temperatures: from 250 to 500°C the removal of volatiles created micropores (pore diameter < 2.0 nm) and mesopores (pore diameter 2.0-50.0 nm) with consequent increase of porosity and surface area of solid char as shown in figure 2.1.

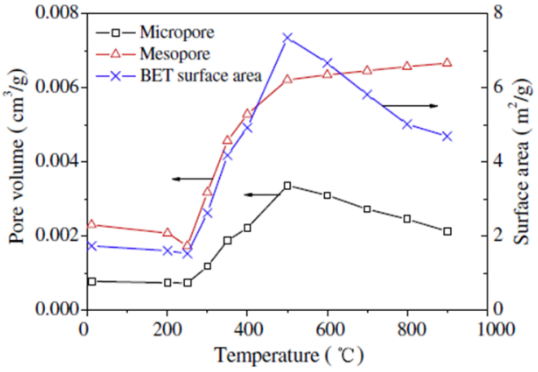

Figure 2.1. Variation of volume and BET surface area with temperature. Reprinted with permission from [97]. Copyright (2009) with permission from Elsevier.

At 500°C deactivation process led to micropore coalescence in char, whereas the carbonization, melting, fusion and softening might occlude the pores, hence preventing the absorption of gas on the particle surface.

The authors also investigated the chemical structure of Biochar during the pyrolysis process. FTIR spectroscopy analysis revealed that the chemical structure started to change above 200°C: characteristic signals of biomass referred to aliphatic groups (2800-3000 cm^{-1}), hydroxyl group (3200-3700 cm^{-1}) and olefinic group (1610-1680 cm^{-1}) disappeared when the temperature reached 250°C. As the temperature raised, carbonyl group (1650-1770 cm^{-1}) and ether structures gradually disappeared, meanwhile the aromatic structure developed, as confirmed by the shift of ν(C=C) and ν(C=O) vibration at lower frequencies. Over 500°C, the chemical structure became polyaromatic and ordered because of the decrease of oxygen and hydrogen content as well as ether groups, unstable at high temperatures. Furthermore, when the temperature increased, FTIR peak referred to aromatic ring C-O stretching vibration decreased due to the weakness of C-O bonds. These latter were broken when large aromatic ring systems were formed: in this case, the volatilization of the oxygen and the combination of active carbons led to the poly-condensation of the aromatic structure with six or more aromatic rings [97].

The analysis of *chemical structure* is fundamental to classify Biochar. It is noteworthy the evolution of Biochar as a function of pyrolysis temperature, reported in Van Krevelen diagram in figure 2.2. The latter describes the decreasing of H/C and O/C atomic ratio with increasing temperature from room temperature (RT) to 900°C. In the diagram, the highest H/C and O/C atomic ratio values refer to aliphatic nature and low aromaticity of biomass. During pyrolysis, H/C and O/C ratio decrease since carbon content and aromatic character of Biochar increase. The peaks referred to hydroxyl, ether, carbonyl and olefinic groups disappear in FTIR spectra of Biochar, meanwhile the signals of aromatic skeletal vibration and aromatic C-H deformation become sharper [82, 85, 88, 100, 101].

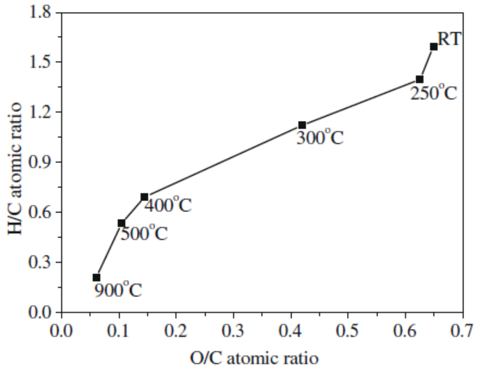

Figure 2.2. Van Krevelen diagram. Reprinted with permission from [97]. Copyright (2009) with permission from Elsevier.

Giorcelli et al. have proved the dependence of final Biochar properties from the operating pyrolysis temperature. In this work, Biochar was obtained by pyrolysis of residues miscanthus at three different temperature (650, 700 and 750°C). The research showed that pyrolysis temperature affected elemental composition, graphitization grade and electrical properties of Biochar: in relation to temperature, carbon content increased, meanwhile mineral components decreased. The electrical conductivity was evaluated on compressed Biochar powder to minimize the voids between the particles. According to the carbon content, electrical conductivity increased up to 2.75±0.85 S/m [102].

Electrical properties are connected to structural phases of carbonaceous materials. Carbon phases can be classified in *crystalline* (graphite), *disordered* (nanocrystalline carbon) or *molecular* (related materials, graphenes). Since graphite is the most stable at low temperatures, thermal treatment during pyrolysis process transforms carbon phase from amorphous structure into ordered graphitic one. Cristallinity of graphite structure depends on pyrolysis temperature: the formation of graphitic sheets occurs between 600 and 1200°C; above 1200°C graphitic sheets became layered and ordered (*graphitization*) and they may arrange in a 3D crystalline lattice. Raman spectroscopy represents a valid analytical tool for examining the disordered forms and crystalline phases in solid carbon. Raman spectra of carbon material show two main peaks related to graphitic crystalline order: G peak or E_{2g} mode, within 1550 and 1651cm^{-1} range, corresponds to π-π^* transitions and D peak or A_{1g} mode, between 1300 and 1400 cm^{-1}, refers to edge disordered of carbonaceous structure. The ratio between the peak intensities (I_D/I_G) allows evaluating the correlation between the disordered of carbon structure and its graphitization degree [103]. The correlation between Raman parameters and pyrolysis temperature of Biochar was studied by *Giorcelli et al.* proving the increasing of disordered carbon structure from 650 to 750°C [102]. *Zhao et al.* explained that the increase of I_D/I_G ratio with temperature was due to dehydrogenation reactions that favored the increasing of condensed aromatic rings. Above 750°C, I_D/I_G ratio decreased since the enlargement of aromatic benzene system with six or more fused rings. Below 750°C, an amorphous carbon structure was prevalent, whose aromatic ring system was represented by three characteristic bands located in a region between G and D band: G_R (G right) related to aromatics with 2–5 rings, V_R (valley right) related to methyl group and V_L (valley left) related to methylene or methyl. All these bands (G_R+V_R+V_L) corresponded to the semi-circle breathing mode of the aromatic ring system with two or more condensed benzene rings. The $I_D/I_{GR+VL+VR}$ ratio takes into account the rate between large aromatic ring system with more than six rings and aromatic ring system in amorphous carbon with 2-8 or more rings. As pyrolysis temperature increases, the $I_D/I_{GR+VL+VR}$ ratio decreases as well, due to the transition from small to large aromatic ring system in Biochar structure [104,105].

Biochar, thanks to its electrical conductivity, is exploited also as energy storage. *Gabhi et al.*, in a recent work, explored monolithic Biochar as electrode in supercapacitor device. The authors pointed out the relation between degree of carbonization and electrical conductivity. After the carbonization process ended at 950°C, Biochar lost 70% of hydrogen and 92% of oxygen, while carbon content ranged from 75 to 95 wt.%. However, it was necessary a minimum carbon content (i.e. 85 wt.%) to make Biochar conductive (> 5.0×10^{-6} S/m): from 83 to 95 wt.% conductivity increased up to 400 S/m. The electrical conductivity was also affected by the presence of volatile species, absorbed on particle surface of porous Biochar and providing an insulation effect. To remove volatiles, Biochar was subjected to a heat treatment that increased carbon content as well as electrical conductivity. The effect of heat treatment was showed in X-Ray spectra as an increase of 2θ peak of graphite crystals at 25° for (002), the plane perpendicular to graphite basal plane and 42° for (100), the graphite basal plane. The higher intensity of two peaks was attributed to the increase of structural order in graphite crystal as well as to the increase of graphite particles in microcrystallites. Furthermore, (002) corresponds to crystalline size of 0.36 nm, close to the spacing between graphite fringe of 0.34 nm that proved the presence of an aromatic ring system in microcrystallites. The increase of graphitic crystals as consequence of heat treatment might be correlated to the increase of electrical conductivity. However, Biochar was still amorphous since the heat treatment was insufficient to complete the graphitization process that required temperatures >1500°C [84]. In 2015, *Zeng et al.* investigated the effect of pyrolysis temperature on crystallinity of Biochar. As the temperature increased from 600 to 2000°C, peaks related to (002) and (100) became sharper due to the increasing of orientation degree of aromatic lamellae as well as the condensation degree of aromatic rings. Both of effects were correlated to formation of crystallites of Biochar whose structure is more ordered and aromatic [100]. *Bourke et al.* asserts that the increased of crystallinity with temperature consisted of a gradual stacking of graphene and its lateral plane growth that led the formation of crystallites [106].

The study of Biochar on nanometric scale provides more detailed information on the structure of Biochar. Recently, *Surup et al.* investigated the nanostructure of pinewood with variation in pyrolysis temperature from 1300 to 2800°C. Transmission electron microscopy (TEM) analyses showed that carbon structure of pinewood char changed from amorphous at 1300°C to a mixture of amorphous and nanocrystalline graphite at 1600°C. The arrangement to onion-like carbon structure became prevalent with the increasing of residence time at 1600°C or with the increasing of temperature at 2400°C. Biochar at 2800°C had a nano-crystalline carbon structure characterized by an increased number of graphene segments and the elongation of graphene-like layers. At this temperature, the graphitization grade was the highest: the distance between graphene segments in char was 0.33 nm, close to graphite spacing (0.34 nm). From 1600 to 2400°C graphite spacing was 0.35 nm that corresponded to a less ordered in char structure [107]. These results supported the nanostructural analysis by TEM that *Surup et al.* carried out in another work on spruce and oak chars derived from pyrolysis at 800, 1200 and 1600°C. TEM images showed that at 800 and 1200°C both of charcoals had an amorphous carbon structure that at 1600°C converted into a mixture of nanocrystalline graphite and amorphous carbon structure. In particular, the authors found that at 1600°C spruce chars had two amorphous carbon structures. An amorphous carbon with a large number of crystallites in which short graphene sheets formed a continuous surface and another amorphous structure in which nano-crystalline graphite was mixed with curved graphene layers with interplanar distance of 0.35 nm.

The nanostructure of oak chars at 1600°C is characterized by nano-crystalline graphite in which the straight graphene layers had interplanar distance of 0.33 nm. The higher graphitization grade of oak chars at 1600°C indicated that the char properties were significant affected by the type of feedstock material [100].

Since the amount of carbon in structure, Biochar might be used in polymer composites to replace petroleum-based fillers like carbon fiber, carbon nanotubes and graphene. *Li et al.* used Biochar carbonized at 1100°C to improve mechanical, electrical and electromagnetic interference (EMI) shielding properties of polymeric composite. This latter was obtained processing in twin-screw extruder a blend of thermoplastic polymer in which were added Biochar particles at 60wt%, 70wt%, 80wt%. XRD and Raman spectra revealed the presence of graphitic structure in Biochar from which depended the electrical conductivity of polymeric composite. Increasing Biochar content, electrical conductivity ranged from 5.3 S/m to 107.6 S/m as well as the EMI shield effectiveness increased up to 48.7 dB at 1500 Hz, they were the highest values among conductive composites. The adding of Biochar improved also mechanical properties of polymer composites: the good affinity between polymer matrix and Biochar promoted the homogeneous dispersion of Biochar and contributed to the improvement of tensile strength, Young's modulus and hardness of composites [111].

Giorcelli et al. investigated the effect of Biochar on mechanical properties of epoxy-based composites. Biochar and Biochar heat treated (Biochar HT), used as filler, were obtained by pyrolysis of maple tree in inert atmosphere respectively at 600 and 1000°C. Both types of Biochar were first grinded and then were dispersed by sonication in a low viscosity epoxy resin. The mixture containing the hardener, previously molded in dog-bone shape, was then cured in oven. The two types of Biochar, at different loadings (i.e. 1, 2, 3, 4, 20 wt.%), significantly affected mechanical properties of the resulting composites. It was observed that from 2 to 4 wt.% of Biochar, composites changed mechanical behavior from brittle to ductile. In addition, 2 wt.% of Biochar was the composition for which tensile strength and elongation of composites were the highest: 48 and 500% respectively for Biochar and Biochar HT. In general, the addition of Biochar improved the stiffness of epoxy composites: 1 wt.% of Biochar and Biochar HT enhanced Young's modulus respectively by 63 and 50%. In small percentage, Biochar increased resilience and tensile toughness: 1 wt.% of Biochar HT improved 100% of the resilience compared to the unfilled cured resin, while 2 wt.% of Biochar and Biochar HT in composite resulted in 11-fold increase of toughness with respect to the unfilled cured resin [112]. In addition to mechanical properties, electrical conductivity measurements were carried out by *Khan et al.*, who evaluated complex permittivity in microwave range (1-4 GHz) of previously analyzed samples containing 2 and 20 wt.% of Biochar. The authors found that both dielectric constant and electrical conductivity in the microwaves increased with filler content but the percolation threshold was higher as compared to the epoxy-based composite containing MWCNTs; in fact, a similar permittivity and conductivity between the composite with 20 wt.% of Biochar and that with 4 wt.% of MWCNTs was observed. The raised percolation threshold was attributed to the three-dimensional structure of Biochar that led to a worse interconnection between particles and hindered the formation of a conductive path throughout the composite. Permittivity of composites with Biochar showed a decreasing trend with the increase of frequency, due to the presence of polar organic groups. In addition, the incorporation of Biochar HT into the epoxy resin showed a lower conductivity at the microwave frequencies due to the removal of thiols at high temperature. However, permittivity results suggested that Biochar at higher content might replace effectively MWCNTs in epoxy resin, with additional advantages: unlike MWCNTs, Biochar is an eco-friendly and low-cost material, easy to disperse in polymer matrices [113].

Recently, spent coffee ground has gained much attention as carbon source. Because of the high content of organic compounds, spent coffee grounds is a valuable source for producing Biochar. Biochar from pyrolysis of spent coffee ground was investigated by *Jagdale et al.* to develop a humidity sensor [114].

Giorcelli et al. evaluated coffee Biochar as conductive filler in epoxy resin. Biochar was obtained through pyrolysis process of spent coffee grounds at 1000°C. Biochar, previously grinded, was dispersed in an epoxy resin using an ultrasonication apparatus. After the addition of the hardener, the mixtures with 5, 10, 15 and 20 wt.% of Biochar were thermally cured and then they were characterized. The authors found that the electrical conductivity of the composite with 20 wt.% of Biochar was the highest (i.e. achieving 2.02 S/m) also in comparison with the composite containing 20 wt.% of carbon black (5.4×10^{-8} S/m). The lower value of electrical conductivity was ascribed to the tendency of carbon black to form aggregates, unlike Biochar that was well dispersed in the epoxy network [115].

2.3 MWCNTs

MWCNTs were studied for the first time about thirty years ago by *Iijima* who discovered, through electron microscopy, a new type of graphitic structure containing sp^2 hybridized carbons [116]. MWCNTs, synthetized by arc-discharge method, had a coaxial tubular structure (needle) of graphitic sheets that ranged in number from 2 to 50 [116]. Since Iijima's studies, the production of MWCNTs had an exponential growth also at commercial scale and many other synthesis methods have been developed [117]. Today, the catalytic chemical vapour deposition (CVD) process is the most widespread method to produce MWCNTs for the advantages connected to the low temperature (500-800°C), cost efficiency, easy control of process parameters and yield up to 95-99% [118]. In CVD synthesis, volatile precursors (generally hydrocarbons) used as carbon source, are placed in a tubular reactor and absorbed on the surface of metal catalyst at high temperature. The carbon, formed during the decomposition of precursor, recrystallizes to form MWCNTs, for which physical (e.g., diameter, length, shape) and chemical (e.g., graphitization, number defect) properties are dependent on set operating conditions (e.g., temperature, hydrocarbons source, reaction time). However, compared to arc discharge technique, the main drawback of CVD method is the lower quality of MWCNTs that need to be purified in a post synthetic step to eliminate carbonaceous contamination [117,119].

The degree of purity can be determined by the use of scanning electron microscopy (SEM) that allows quantifying the percentage of unwanted materials per unit area; at certain magnifications it is possible to distinguish tubular material from spherical particles and irregular objects. In addition to morphology, SEM analysis is an effective tool to provide information about geometrical parameters including diameter and length of MWCNTs. In particular, the diameter can be estimated as average value from multiple SEM images at magnification greater than 20,000× up to a lower resolution point ranging from 1 to 20 nm. However, transmission electron microscopy (TEM) and high resolution TEM (HRTEM) allow collecting more detailed information on the inner morphology of CNTs [120]. HRTEM at resolution of 20 nm was used by *Guadagno et al.* to estimate some morphological details of MWCNTs to functionalize with 1-pyrenebutyric acid. Pristine MWCNTs had a diameter ranging from 9 to 19 nm, a length from 100×10^{-9} to 1×10^{-6}m and number of walls from 4 to 11 [121].

Besides, HRTEM provides information about the arrangement of tubular structures: tubes that constitutes MWCNTs can be scrolled sheets, nested or concentric, herringbone-type or stacked cup arrays. In addition, HRTEM coupled to fast Fourier transform (FFT) is a valuable instrument to estimate the degree of crystallinity of MWCNTs. In FFT images, highly crystalline material shows sharp spot and narrow peak, conversely blurred spot and broad peaks correspond to a lower crystalline material [120,122].

In addition to morphology, optical characterization including Raman and reflectance spectroscopy provides useful information about defects, purity and colour of MWCNTs. The reflectance spectroscopy allows measuring the absorption of a particulate material. Since the dependence on electronic structure and molecular topology, absorption spectrum allows distinguishing MWCNTs from SWCNTs, graphite from amorphous carbon. Compared to wavelength, the absorbance is dependent on the qualities of colour that is connected to the electronic structure and topology of MWCNTs. The absorption spectrum of MWCNTs is characterized by uniform reflectance in the visible and infrared with a near peak at 248 nm, similar to graphite and SWCNTs [120]. Unlike SWCNTs, optical absorbance in visible and infrared region of MWCNTs does not depend on chiral angle of the carbon nanotube outermost shell but on the polarization orientation with respect to the direction on the electric field or nanotube position [117].

The infrared spectrum of MWCNTs is produced by FTIR spectroscopy that provides information about functional groups bonded on the carbon surface of

MWCNTs. FTIR spectrum of MWCNTs, from 400 to 4000 cm^{-1}, shows the presence of characteristic signals at 1640 cm^{-1} and 1543 cm^{-1}, due to C-C stretch referred to the skeletal vibration. *Guadagno et al.*, in addition to unoxidized domains, detected also the peaks associated to oxygenated functional groups, i.e. O-H, C-OH, C-O stretching vibration, respectively at 3460 cm^{-1}, 1220 cm^{-1}, 1024 cm^{-1} [121]. *Osswald et al.* identified two main peaks at 1600 cm^{-1} and 3450 cm^{-1} ascribed to O-H stretching vibration and another peak at 1450 cm^{-1} considered as unique to MWNTs.

The FTIR Raman spectrum shows two signals, at 1350 cm^{-1} and at 1586 cm^{-1}. The first band is D mode relative to double resonance effect of disordered amorphous carbon and is affected by defect and structural modification of carbon nanotube; the second band is G mode that corresponds to tangential stretching of graphitic carbon atom. The $R=I_D/I_G$ ratio between D and G band intensities allows quantifying structural defects and the order of graphitic layer [123].

Since the limited amount of studies about Raman spectroscopy, the interpretation of MWCNTs spectra is usually focused on the analysis of SWCNTs. Raman spectra of SWCNTs have some typical features that can be extended also to MWCNTs. The main signature of SWCNTs is the band at low frequency (< 200 cm^{-1}) that is ascribed to A_{1g} radial breathing mode (RBM), whose signal, completely absent in graphite, can be detected only when the diameter of carbon nanotube is below 2 nm [120,124].

The radial breathing mode was found also by *Zhao et al.* in MWCNTs at lower frequencies (100-600 cm^{-1}) assigned to the narrow innermost sheets, whose diameter depends on the growth method [125]. However, as published by *Donato et al.*, in some cases the signals detected at lower frequencies are not ascribed to RBMs but to iron catalyst and defects in MWCNTs [126].

G band has also a significant relevance in the interpretation of Raman spectra. While in graphite spectra it appears as a single peak at 1582 cm^{-1}, G band in carbon nanotubes is composed of two peaks (G^+ and G^-) in the 1550-1600 cm^{-1} range. In particular, G^+ band refers to longitudinal-optical (LO) phonon mode, in which the atom vibration is along nanotube axis, in contrast with G^- feature that corresponds to the atomic displacement along circumferential direction of carbon nanotube [120,121]. *Guadagno et al.* observed in MWCNTs spectrum a single G peak close to that of graphite (1582 cm^{-1}), as well as a lower intensity of G^+ and G^- splitting and asymmetric characteristics line shape [121].

In carbon nanotubes spectra, the signals at 2600 cm^{-1} refer to G', the second-order harmonic of D mode. As explained by *DiLeo and co-workers*, G' band is an alternative to I_D/I_G ratio to evaluate quality and purity of MWCNTs since the two-phonon process is affected by the presence of defects in the samples [127].

In the range 1700-1800 cm^{-1}, peaks of second order mode are usually neglected for their low intensity [120].

In addition to spectroscopic techniques, thermogravimetric analysis (TGA) could be taken into account to evaluate the quality of MWCNTs. Since the residual masses, thermal decomposition and thermal stability are connected to the presence of impurities, TGA is an effective alternative to identify the quality of MWCNTs for bulk samples [120]. Thermal stability is connected to the presence of aromatic bonds in the structure of MWCNTs but is also affected by the presence of metals, number of walls or amorphous and graphitic carbon forms. The number of oxidation peaks, as derivative of weight loss curve, provides information about the purity and crystallinity of MWCNTs [128]. With respect to other carbon structures, MWCNTs have higher oxidation temperatures generally in the range of 400-650°C [120]. Annealing process has the effect to increase the crystallinity of MWCNTs samples and their oxidation temperature. As observed by *Endo et al.,* annealing process on MWCNTs caused the decrease of interlayer spacing and mass density, due to the conversion from amorphous to graphitic structure. In particular, the authors compared, by using Raman spectroscopy, as-grown MWCNTs with graphitized MWCNTs at 2000°C and 2800°C. They observed that graphitization process was effective only at 2800°C, since at this temperature significant changes appeared in Raman spectra. The main feature of graphitized MWCNTs is the increased intensity of G band at 1580 cm^{-1} and the decreased intensity of D band at 1355 cm^{-1}, which indicate a significant reduction of defects in the sample [129]. *Andrews et al.* studied the effect of graphitization on structural properties of MWCNTs, subjected to heat treatment at annealing temperature between 1600 and 3000°C. The authors demonstrated that, at the vaporization temperature of iron (beyond 1800° C), the annealing process removes residual catalyst both at the tip and on the core of MWCNTs: iron content decreased from 7.10 wt.% at 1600°C to <0.01wt% at 3000°C. The annealing treatment also caused the development of graphitic structure since the higher temperatures determined the decrease of d-spacing and the increase of peak intensities at (002), (100) and (110) as proved by XRD analysis. Micro-diffraction analysis confirmed the increase of graphitization degree as the reflection spots at (004), (006) and (008) planes demonstrated. Besides, the higher annealing temperatures had also the effect of removing microstructure defects [130]. *Kim et al.* pointed out the transformation from disordered to ordered structure of MWCNTs as a result of thermal annealing. The structural change was confirmed by the reduction of R value (I_D/I_G) from 0.98 to 0.23 and the growth of crystallites. Nevertheless, the development of tug formation on the surface of annealed carbon nanotube has a reinforcement effect, helpful especially for nanotube-polymer system [131]. The graphitization process aims at increasing graphitic perfection by removing microstructural defects. In MWCNTs, defects are related to the presence of highly reactive carbon atoms such as vacancies, interstitials, edges and carbon chains. In the structure of MWCNTs pentagons, heptagons or octagons, embedded in sp^2 hexagonal lattice, distort the curvature of carbon nanotube [120]. Such defects as those generated by bond rotations do not lead to a large curvature distortion of carbon nanotube. These, known as 5-7-7-5 or Thrower–Stone–Wales defects, occur in tube surface where four hexagons are transformed in two pentagons and two heptagons embedded in hexagonal lattice [132,133].

Since many phenomena occur at the surface of MWCNTs, BET (Brunauer-Emmet-Teller) theory is widely applied to determine specific surface area, from which the catalytic activity, toxicity and gas absorption depend. Specific surface area plays an important role in the interaction of MWCNTs with host material in a composite material; surface area has relevance to evaluate the adsorption capability and catalytic activity and it is subjected to modifications during purification and functionalization process of MWCNTs [120]. The main contribution to the determination of specific surface area came from *Peigney et al.*, who calculated the theoretical external surface area in relation to diameter and number of walls of MWCNTs. The theoretical surface was found ranging from 50 to 1315 m^2/g, mainly dependent on the number of walls of carbon nanotubes; these results were in agreement with the literature values for the measured specific area in microscopic characteristics [134]. *Yang et al.* studied the capillary condensation of capped MWCNTs. They divided pores in the inner hollow cavities with diameter of 3.0-4.0 nm and aggregated with diameter of 20-40 nm. They demonstrated that the aggregated pores between attached carbon nanotubes contributed for the absorption and capillarity more than the inner cavities. The authors estimated that absorption by aggregated pores is about 78.5% (590 mg N_2/g) of the total absorption (750 mg/g) [135]. Molecular absorption is used to measure the bulk density; pycnometry is employed for measuring skeletal density. MWCNTs are a mesoporous material, whose skeletal density is about 2.0 g/cm^3 and bulk density ranges in general from 0.03 to 0.22 g/cm^3 [117].

As MWCNTs are subjected to thermal and chemical activation treatments, the specific surface area increases by 50-380% due to the removal of both capped ends of nanotubes. *Kukovecz et al.* demonstrated that the surface area of opened MWCNTs can be estimated as 2360/N (m^2/g) where N is the number of walls [117]. Ball milling method was employed as mechanical process by *Kònya et al.* to cut long MWCNTs, whose tips, as the effect of high-pressure, collapsed and an open tube structure with symmetrical ends was generated. As a result of ball milling process, surface area increased from 254 to 290 m^2/g due to the opening of capped ends. The high pressure (2-6 GPa) generated during ball milling process was not sufficient for breaking MWCNTs [136]. *Shen et al.* estimated with scanning probe microscopy that compressive strength of MWCNTs was about 5.3 GPa [137]. In addition, MWCNTs have exceptional Young's modulus that in the axial direction reached terapascal order (TPa) and tensile strength of 60 GPa as explained by *Treacy et al.*, who investigated the mechanical properties of individual carbon nanotubes [138]. *Palaci et al.* found that Young's modulus and stiffness decreased with radius of MWCNTs up to an asymptotic value of 30±10 GPa for external radius >5 nm [139]. *Yu et al.* found that the tensile strength of the outermost layer of individual MWCNTs does not depend on the outer shell diameter. Tensile strength ranged from 11 to 63 GPa, higher than graphite whiskers (20 GPa). The analysis of stress-strain curve allowed evaluating the Young's modulus of the outermost layer that represents a measure of stiffness. The Young's modulus ranged from 270 to 950 GPa with strain at failure higher than 0.12%. The values of nominal tensile strength and Young's modulus of cross-sectional area were lower and varied respectively in the range of 1.4-2.9 GPa and 18-68 GPa. In addition, a wavelike structure, visible in TEM, was probably due to the elastic energy that, as a stress wave, reached the outer surface of MWCNTs and caused its deformation [140].

For their unique properties, MWCNTs are attractive materials for the development of nanoscale electronic devices. The high thermal and electrical properties of MWCNTs are related to phonon conduction and high current carrying capability in carbon sp^2 network [141]. *Ando et al.* found that the electrical conductivity of individual purified MWCNTs, with inner and outer diameter respectively of 1 and 31 nm, was about $1.85\times10^5\ \Omega^{-1}m^{-1}$ [142]. *Yang et al.* determined thermal and electrical conductivity of MWCNTs films (thickness from 10 to 15 μm). They found that the average thermal conductivity in growth direction does not depend on film thickness and was about 15 W/mK. When the authors considered the filling volume fraction of 7-8%, the effective thermal conductivity in longitudinal direction was found of about 200 W/mK [143]. The value was in accordance to *Gaillard et al.*, who measured thermal conductivity values of 180 and 220 W/mK for MWCNTs film [144]. *Yang et al.* pointed out that, with respect to MWCNTs array and film, thermal conductivity of single tube is significantly higher and ranges from 600 to 6000 W/mK, these values are overestimated due to the heat loss outside carbon nanotube. Conversely, in bulk, the high density of MWCNTs lowers air gap among tubes and the heat loss is reduced. The lower thermal conductivity can be also ascribed to high defect density and inter-tube coupling that are responsible of phonon scattering [145]. Inter-tube coupling or tube-tube interaction, characterized by van der Waals forces, increase with packing density and cause the decrease of thermal transport in single carbon nanotube, hindered by the interaction of carbon nanotubes [146].

Unlike thermal transport, the electrical resistance increases with the thickness of MWCNTs films, according to Ohm's law. This behaviour indicates a diffusive rather than ballistic electron transport in nanotubes. The effective electrical conductivity in longitudinal and transverse directions were respectively of $\sigma_\parallel= (1\text{-}4)\times10^4\Omega^{-1}m^{-1}$ and $\sigma_\perp=(5\text{-}25)\times10^2\Omega^{-1}m^{-1}$; the $\sigma_\parallel/\sigma_\perp$ ratio ranged from 20 to 30, confirming the anisotropy of electrical conductivity. The higher value in longitudinal direction can be ascribed to the fewer tube-tube contact in axis direction and the dependence of $\sigma_\perp$ from the filling fraction of MWCNTs [143].

Yang et al. proposed a model that describes the electric transverse transport both across MWCNTs and in MWCNTs arrays. In a single carbon nanotube, electrons move from shell to shell by tunnelling effect and along circumference by circumnavigated process [143]. Furthermore, the electron transfer between π orbitals in radial direction contributes to ballistic electron transport in circumnavigating process that can explain the higher electrical conductance in the outmost shell of MWCNTs.

In MWCNTs array, the transverse electron transport is reduced by the presence of tube-tube junctions that hinder the electron mean free path by inter-tube hopping process. Circumnavigating and inter-tube hopping process contribute to total transverse electron transport, resulted higher than out of plane transport in 3D graphite, dominated only by the inter-plane hopping process and weak interplane coupling interaction [143].

While electrical properties of MWCNTs are investigated extensively in mesoscopic scale, thermal conductivity of single nanotube has remained a challenge. Besides, some disadvantages are connected to the extraction of single nanotube thermal properties from bulk measurements, where tube-tube junctions act as barrier to thermal transport. For the sake of comparison, theoretical studies have proved that a SWCNT could exhibit higher thermal conductivity (2980 W/mK) than graphite and diamond, known for their excellent thermal conductivity [145]. Recently, *Kim et al.* observed that thermal conductivity at room temperature of single carbon nanotube was about 3000 W/mK, higher than two order of magnitude than macroscopic estimation [147]. Thermal conductivity of individual carbon nanotube with outer diameter of 45 nm was measured by *Choi et al.* and resulted about 650 and 830 W/mK [148]. *Prasher*, studying thermal conductivity of MWCNTs in the temperature range of 10-100 K, noted a thermal behaviour similar to graphite [149].

Xie et al. measured thermal conductivity of carbon nanotube array using laser flash technique in the range from -55 to +200°C. They proved the dependence of thermal diffusivity of carbon nanotube on temperature within -55 and +70°C; conversely, from 75 to 200°C no significant changes were measured. Besides, they found that thermal diffusivity determined at ambient temperature was about 4.6 cm^2s^{-1}, higher than that of copper (1.2 cm^2s^{-1}). According to the relation $\lambda=\alpha\times\rho\times Cp$, mean thermal conductivity (λ) was estimated as product between thermal diffusivity (α), density (ρ) and specific heat (Cp). Thermal conductivity of individual carbon nanotube increased with temperature and reached 750 W/mK at room temperature. The effective thermal conductivity (λeff) of carbon nanotube array was determined using the correlation between thermal conductivity of individual carbon nanotube (λ), carbon nanotube per unit area (N) and average area of single carbon nanotube (A), according to

$$\lambda eff=\lambda\times N\times A$$

λeff estimated at room temperature and 200°C was 60 and 100 W/mK, respectively [150].

The exceptional electronic, mechanical and thermal performance of MWCNTs attract great interest to develop nanoscale technologies based on conversion, conservation or energy harvesting [144,151]. MWCNTs are widely exploited as carbon filler in polymers to produce high value composite material with such advanced properties as thermal and electrical conductivities, electromagnetic shielding and even fire retardancy. Despite this premise, in recent investigation, MWCNTs are not employed as primary filler but with the role of transferring the load from the matrix to the reinforcement in composites [117]. In literature, the main drawback connected to the use of MWCNTs as reinforcement is the heterogeneous quality of polymer nanocomposite. The reason is the difficult to match and control some criteria: pre-treatment [152], disentanglement [153] and orientation [154] of MWCNTs are the key factors for developing high-performance nanocomposites.

2.4 Aim of the work

The previous evaluations, focused on the Biochar and MWCNTs, revealed that the composition and the chemical structure are determinant to assess the properties of the two carbon materials. The ordered graphitic structure of carbon sp^2 hybridized atoms is responsible for the superior thermal, electrical and mechanical properties of both Biochar and MWCNTs, whose morphologies are strictly connected to the different nature of the precursors from which they derive. The Biochar, obtained by pyrolysis of renewable resources, is an emergent material, whose particles, characterized by sponge like structure, have micrometric size. On the other hand, the MWCNTs represent a consolidate material used as filler to design composites with advanced properties in order to develop engineering materials addressed to several industrial sectors.

In this thesis, MWCNTs and Biochar are exploited as carbon fillers in acrylic UV-LED curable coating to design high value-added composite with enhanced thermal, mechanical and electrical properties.

This is a completely new approach (to the best of the author's knowledge, it has never been reported in the scientific literature yet), because of the use either of Biochar in thermosetting matrices, or of the UV-LED curing technique as a robust, reliable method for producing functional coatings and films. This is the reason, for which UV-LED curing, in the last years, is partially replacing the "standard" UV-curing processes for the production of advanced functional materials. In addition, another challenge is associated to the improvement of the naturally heterogeneous dispersion of MWCNTs in a thermosetting matrix. Indeed, the entanglement of polymeric chains and the poor interfacial interaction between MWCNTs and polymeric chains affect significantly the performance of resulting nanocomposite coating. Since the low quality of MWCNTs composites, this work also aims at studying and exploiting the shuttle effect provided by the Biochar that can improve the dispersion of the MWCNTs in the polymer matrix, as well as the property performance of the resulting composite films. Furthermore, as emerged from literature, the Biochar can be considered a valuable alternative to the MWCNTs: thanks to its high graphitization grade, strictly connected to the processing conditions of biomass, the Biochar is comparable with the conventional carbon fillers. In particular, among the widespread range of the biomasses, the spent coffee grounds are selected as precursor of the Biochar used in the present work. As the most popular beverage in the world, the production of coffee is about millions of tons per year and its consumption increases by annual with consequent huge amount of generated solid waste. Characterized by a lignocellulosic composition, spent coffee grounds can be recovered and pyrolyzed to convert the biomass into a high value resource. Moreover, the use of Biochar as alternative to conventional carbon fillers is advantageous in terms of environmental and economic benefit since it is a sustainable and low-cost alternative to the expensive MWCNTs for designing thermosetting UV-LED curable coating with advanced properties.

As eco-friendly, inexpensive and high operating efficiency process, the UV-LED curing technique is investigated as transformation process of thermosetting resins since it benefits of several advantages, among which saving money, time and energy are noteworthy. Therefore, since its innovative features, UV-LED curing technology has been selected to produce value-added coating composites obtained by the incorporation of the carbon fillers in epoxy-acrylate curable resin containing a specific photo-initiator. In addition to prove the efficiency of the UV-LED curing technique as innovative transformation process, the present study also explores the presence of Biochar and MWCNTs on the effectiveness and completeness of the photo-induced process.

Chapter 3

Experimental part

Characterization techniques

Characterization techniques are crucial to investigate the physical and chemical properties of different types of materials. In academic and industrial fields characterization tools are widely used to test and optimize the performance of polymeric composites. The characterization techniques provide information on structure-property relationship of filler within a polymeric matrix, as molecular interaction, molecular structure and morphology affect the final properties of composites materials.

Thermal analyses are used to investigate macroscopic properties such as heat capacity, glass transition temperature and viscoelastic behaviour of polymeric materials. A huge range of spectroscopic techniques, including Ultraviolet-Visible (UV-VIS) and Fourier transform infrared (FT-IR) spectroscopy, provide information on chemical composition and structure of polymeric composites. Scanning electron microscopy (SEM) techniques allow probing the surface and structure of composites at microscopic level. Rheological measurements are used to characterize the nanostructure of composite system since the polymer-filler interaction affects the performance properties of the materials.

In this chapter thermal, spectroscopic, microscopic and rheological techniques will be discussed in detail as well as transient plane source (TPS) and electrical resistivity probes methods used to measure respectively thermal and electrical conductivity of polymeric materials.

3.1 Thermal analysis

Thermal analysis comprises different techniques based on the response of the material to heating or cooling processes. These techniques are commonly applied in the characterization of polymeric material. The thermal techniques discussed in this section are differential scanning calorimetry (DSC), thermogravimetric analysis (TGA) and dynamic mechanical thermal analysis (DMTA).

3.1.1 Differential scanning calorimetry (DSC)

Differential scanning calorimetry (DSC) provides information on the physical transitions that involve materials when heat is absorbed or released. DSC technique measures the heat flow difference inside encapsulated high-purity aluminum DSC pan, between a reference sample and a testing sample (such as a polymeric material), when subjected to the same temperature program. The modes of operation of DSC depend on the temperature that can be held constant during the test or can be lowered or raised at a certain preselected rate. The classical DSC operation mode provides that the heating rate is constant and temperature program is controlled by the following relation:

$$T(t) = T_0 + \beta_0 \cdot t \tag{3.1}$$

where T_0 is the starting temperature and β_0 is the heating or cooling rate. Depending on the heating rate, the operation temperature program can be distinguished in isothermal and scanning mode.

In the isothermal mode, the heating rate is zero and T_0 is a constant. Although the heating rate is zero, the heating flow is not equal to zero due to the asymmetry of exchange heat that involves the reference and the sample with the surroundings.

In scanning mode, the temperature changes with time and the heat flow rate Φ_{C_p} is proportional to temperature rate $\frac{dT}{dt}$ through the heat capacity C_p, according to the relation:

$$\Phi_{C_p} = C_p \cdot \frac{dT}{dt} \tag{3.2}$$

The measured heat flow is composed by three parts as depicted in the following relation:

$$\Phi(T,t) = \Phi_0(T) + \Phi_{Cp}(T) + \Phi_r(T,t) \tag{3.3}$$

$\Phi_0(T)$ is determined by the asymmetry of the DSC, $\Phi_{Cp}(T)$ is determined by the difference in heat capacity between the sample and the reference and $\Phi_r(T,t)$ is the contribution from the latent heat of the sample.

The instrument output is a thermogram, in which the heat flow rate (φ_m) or the temperature (K) is reported as a function of time, allowing to study kinetic events and thermodynamic processes. In particular, kinetic events of thermosetting composites are related to cure and enthalpic relaxation; conversely, thermodynamic processes refer to specific heat capacity and glass transition temperature of polymeric matrix.

DSC system belongs to heat-exchange calorimeters when they operate in heat flux mode. In heat flux mode, both DSC pans (reference sample and composite material) are heated from the same source and the signal, measured as temperature difference, is converted into power difference. In this setup, the heat exchange can be dominated by turret type measuring feature where the sample crucibles are placed onto hollow cylinders. The heat flux, from the furnace, reaches the jacket of two cylinders that acts as a support of the test sample and the reference sample. The differential temperature (ΔT) between the test sample (T_S) and reference sample (T_R) is detected by nickel alloy (Chromel®) area thermocouples integrated on top of two cylinders. ΔT signal is a characteristic of the sample and is proportional to the measured heat flow rate (φ_m), expressed in mW, through the instrumental constant k', according to the relation 3.4.

$$\varphi_m = -k' \times \Delta T \tag{3.4}$$

Besides, turret type system is characterized by a third Chromel®-constantan thermocouple located in the middle of the bottom plate (made of constantan) to detect the furnace temperature (T_0) and thus, to measure the thermal inertia [155,156].

3.1.2 Thermogravimetric analysis (TGA)

Thermogravimetric analysis (TGA) is a useful technique to investigate the changes that occurs in mass of materials when subjected to a specific temperature program. TGA instrument is a thermo-balance, consisting of a heating furnace and a high accuracy analytical balance that are electronically managed. Depending on the furnace wending material, the temperature furnace ranges from room temperature up to 2000°C. The furnace temperature can be programmed to ramp up from 1 to 20°C/min as the heating rate or even kept constant for isothermal analysis.

Since endothermic and exothermic process occur, relatively during absorption or release of heat, the sample temperature is measured by thermocouples integrated to one of the ends of the furnace. Few milligrams of the sample, placed inside a refractory crucible made of alumina, quartz, aluminum or platinum, are subjected to a heating run in static or dynamic gaseous atmosphere. The common static atmosphere is a gas with low pressure as 10^{-3}-10^{-4} Pa.

The dynamic condition involves the use of a flowing gas that could be inert (nitrogen) or reactive (synthetic air) around the sample with a fixed rate, usually ranging from 50 to 100 ml/min. From one hand, the adoption of inert gas allows to remove from the furnace, through a specific valve, the corrosion gaseous products that are formed during the decomposition process. On the other hand, reactive atmosphere is created into the furnace to study the mass variation due to the reaction between gaseous reactants and the sample. In this latter case, a positive variation of mass is connected to adsorption, oxidation or reduction process occurring between the sample and the atmosphere. Conversely, thermal decomposition, combustion or desorption are related to a negative variation of the sample mass. The instrument output is a thermogravimetric curve plotted in the integral or in the differential form. The integral curve (TG) represents the mass (mg) or percentage weight loss (%) as a function of the time or temperature, the differential form corresponds to derivative of TG curve (DTG) as a function of the time. The DTG curve, expressed in mg/min and plotted as a function of time or temperature, allows to identify through the upward and downward peaks, respectively, the mass gain and mass loss steps that involve the sample during the heating run.

The position and the shape of TG curve are correlated to temperature (T) and extent conversion (α) according to the kinetic relation 3.5:

$$\frac{\partial \alpha}{\partial t} = k(T)f(\alpha) \tag{3.5}$$

where $k(T)$ represents the dependence of constant rate from temperature and $f(\alpha)$ represent the dependence of reaction model from extent conversion defined as a fraction of total mass loss for any current mass m

$$\alpha = \frac{mi-m}{mi-mf} \tag{3.6}$$

with mi and mf respectively the initial and final mass of the sample [157,158].

3.1.3 Dynamic mechanical thermal analysis (DMTA)

Dynamic mechanical thermal analysis (DMTA) is a polymer characterization technique based on measure of deformation response as result of oscillatory stress applied to the material at controlled frequency or temperature. As the oscillatory stress is applied, the sample deforms sinusoidally according to equation 3.7:

$$\sigma = \sigma_0 sin\omega t \tag{3.7}$$

where σ represents the stress, $\sigma_0$the maximum stress, ω the frequency oscillatory and t is the time. The strain response of the sample depends on extreme material behaviours, the sum of viscous and elastic components provides the strain wave. The Hookean limit corresponds to an oscillatory elastic strain of the material according to equation 3.8:

$$\varepsilon(t) = E\sigma_0 \sin(\omega t) \tag{3.8}$$

where $\varepsilon(t)$ is the strain at time t, E is the modulus, σ_0 is the maximum stress and ω is the frequency. Since the strain at maximum stress (ε_0) is linearly dependent on the modulus E, according to the relation $\varepsilon_0 = E\sigma_0$, equation 3.8 becomes equation 3.9:

$$\varepsilon(t) = \varepsilon_0 \sin(\omega t) \tag{3.9}$$

in this case, the elastic response contributes to in-phase wave as shown in figure 3.1 (a).

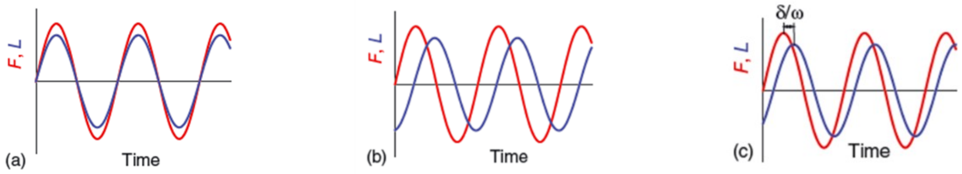

Figure 3.1. Elastic response, in-phase curve (a), viscous response, out of phase curve (b), viscoelastic behaviour (c). Reprinted with permission from [160]. Copyright (2017) with permission from John Wiley and Sons

The viscous contribution is represented by the out of phase curve in figure 3.1 (b) and corresponds to the first derivative of the strain according to the equation:

$$\varepsilon(t) = \frac{\eta \partial \sigma_0}{\partial t} = \omega\sigma_0 \sin(\omega t + \frac{\pi}{2}) \tag{3.10}$$

where η is the viscosity.

The viscoelastic behaviour of material is thus the sum of elastic and viscous contribution represented in figure 3.1 (c) and expressed by the equation:

$$\varepsilon(t) = \varepsilon_0[\sin(\omega t) cos\delta + \cos(\omega t)\, sin\delta] \tag{3.11}$$

with δ the angle resulted from the difference between the stress applied and the response strain.

The graph depicted in figure 3.1 (c) can be split into the two components: $\varepsilon' = \varepsilon_0 sin\delta$ and $\varepsilon'' = \varepsilon_0 cos\delta$, respectively the in-phase and out of phase curve, the sum of which is the complex strain vector $\varepsilon^* = \varepsilon' + i\varepsilon''$.

The DMTA technique allows studying both molecular relaxation and macroscopic process that involve the material subjected to a sinusoidal load. Dynamic mechanical test provides information about viscoelastic behaviour of polymers since it allows to obtain storage, or in-phase modulus (E′), and loss, or out of phase modulus (E″), that correspond to the elastic and viscous behaviours of the material, respectively. The ratio between loss and storage modulus (E″/E′) represents the loss tangent or tanδ: as E″ increases, tanδ increases as well since microscopic events (molecular relaxation) and macroscopic factors (interfacial failure and phase boundary motion) occur during the deformation. Furthermore, this analysis is frequently used to determine the glass transition temperature Tg of the polymeric material. When polymers are subjected to the heating rate, the mobility of molecular chain is sufficient for the transition from glass-like condition to mobile system [159,160].

3.2 Spectroscopic analysis

Spectroscopy is a qualitative and quantitative analysis based on the interaction of electromagnetic radiation with the matter. Spectroscopic methods differ for the species to analyse, the type of radiation-matter interaction and the electromagnetic range adopted during the analysis. Spectroscopic method can be distinguished on the base of frequency range where the absorption of radiation occurs, typically ultraviolet (UV), visible (VIS) or infrared (IR) frequency ranges.

3.2.1 UV-Visible Spectroscopy

Ultraviolet (UV)-visible (VIS) spectroscopy is quantitative and qualitative tool based on the absorption of UV-VIS radiation frequencies by absorbing species. The spectrophotometer is the instrument able to record the absorption spectra in the UV-VIS range, since it measures and compares the intensities of light before and after passing through the sample.

The main aspect of UV-VIS spectroscopy is the interaction of the phonon as probing particle of radiation and the electrons of the matter. The wavelength and particulate properties of radiation is expressed by equation 3.12:

$$E = h\upsilon = \frac{hc}{\lambda} = hc\tilde{\upsilon} \tag{3.12}$$

where E is the energy of the phonon, h is the Plank's constant (6.626×10^{-34}Js), υ is the frequency of radiation, c is the speed of light in vacuum, λ is the wavelength of light expressed in units of nm and $\tilde{\upsilon}$ is its reciprocal, proportional to the energy, is in units of cm^{-1}. Equation 3.12 points out that photons transport monochromatic light characterized by single frequency waves with equivalent energy and single wavelength. The absorption spectroscopy interests the wavelengths within the UV range from 200 to 400 nm and the visible range from 400 to 800 nm, in which the interaction between matter and the electromagnetic radiation is manifested as colour.

The absorption process involves the transfer of photon energy to the absorbing species that, from a ground state (the lower energy state), evolves to an excited state. Since the quantization of energy, the absorption process is quantitative when the photon energy matches the difference between the energies across transition levels. The absorbance of photon energy leads to a series of molecular transitions due to the changes in vibrational and rotational energy levels. The absorption spectrum obtained by plotting the photon energy versus the radiation absorbance indicates the proportionality between the absorbing species concentration to its measured absorbance. This fact is known as the Lambert-Beer law (3.13):

$$A = \log\left(\frac{I_0}{I}\right) = \varepsilon Cl = -\log\left(T\right) \tag{3.13}$$

where A is the absorbance, I_0 is the intensity of monochromatic light before the sample, I is the intensity after passing the sample; C is the concentration, ε the extinction coefficient and l is the path length of light. On the right, T is the transmittance and represents the ratio $\frac{I}{I_0}$ that is expressed in percentage [161,162].

3.2.2 Attenuated Total Reflection Fourier Transform Infrared (ATR-FTIR) Spectroscopy

Attenuated total reflection Fourier transform infrared (ATR-FTIR) spectroscopy is the most common FTIR sampling technique applied in mid-infrared (MIR) region spectroscopy, ranging from 4000 to 400 cm^{-1}. ATR is a non-destructive technique based on the optical properties of rare and dense medium. As the IR light travels inside an optically denser medium, it is totally reflected at the interface created with the optically rarer medium. At the interface, an internal reflection element (IRE), typically diamond crystals, germanium or ZnSe, featured by high refractive index, forms an evanescent field. The radiation, through the evanescent field, reaches the interface where it is absorbed by the sample. ATR technique, based on reflection phenomena, provides spectral information about functional groups of the surfaces, thick or highly absorbing material. The sampling depth depends both on the angle of incident light and refractive index of the crystal that should be higher than that of the sample. Germanium, with refraction index of 4, ensures a penetration depth of 0.65 μm; diamond with a refraction index of 2.40, leads a deeper light penetration of 1.66 μm.

If compared to conventional spectroscopy techniques, ATR is characterized by the total internal reflectance since the angle of incidence is greater than the "critical" angle θ_c, respect to which the radiation is totally reflected. In this case, the light is not transmitted in lower index medium. Since the reflected light provides spectral information about the sample at the interface crystal-sample, ATR is equipped with a single reflection crystal or a multiple reflectance crystal respectively for micro-ATR and bulk samples. The real parts of the refractive indices of crystal (η_1) and sample (η_2) affect the critical angle according to equation 3.14:

$$\theta_c = sin^{-1}\left(\frac{\eta_2}{\eta_1}\right) \tag{3.14}$$

The refractive index of the sample is composed by a real part (n) and an imaginary part (ik) where k is the extinction absorption coefficient:

$$\eta = n + ik \tag{3.15}$$

The real component is the regular refractive index that corresponds to the lack of absorption. The imaginary part of the equation 3.15 is comprised within an absorption band, from which the anomalous dispersion results. This effect influences significantly the reflectance spectra when the incident angle is close to a critical angle.

The total absorption can be expressed as function of θ the incident angle according to the equation 3.16:

$$A(\theta) = \int_0^{\infty} \alpha(z) e^{-z/dp}\, dz \tag{3.16}$$

where z is the depth into the sample and $\alpha(z)$ is the absorption coefficient as a function of z. The reflected radiation assumes into the sample the aspect of evanescent wave, whose effective penetration dp depends on the electric field amplitude and is depicted by equation 3.17:

$$dp = \frac{\lambda}{2\pi n_p (sin^2\theta - n_{sp}^2)^{1/2}} \tag{3.17}$$

where λ is the wavelength of radiation, θ is the incidence angle, n_p is the refractive index of crystal, n_{sp} represents the ratio between the refractive index of the sample and that of crystal.
From the equation above results that:

- ATR method has a sampling depth of 2-15 μm and is dependent on the wavelength, in particular it increases as wave number decreases;
- the sampling depth can be controlled through the refractive index of the crystal and the incidence angle of the light;
- to collect IR spectra, it is necessary a tight contact between the sample, soft or liquid material, and the crystal;
- since the penetration depth depends on the wavelength number, the absorbance loses proportionality at high frequency;
- an anomalous dispersion of the spectrum, including peak shift, distortion of peak intensities, lowering of peak symmetries, occurs when the refractive index of the IRE is close to that of the sample [163,164].

3.3 Morphological analysis

3.3.1 Field emission scanning electron microscopy (FESEM)

Field emission scanning electron microscope (FESEM) is used for the morphological characterization of specimens. The microscope is based on high resolution imaging technology to highlight morphological details down to 1 nm. FESEM apparatus is constituted of a vacuum column, in which a field emitter gun (FEG), a type of field emission source, produces a current beam. The FEG, also known as cathode field emitter, is characterized by a tungsten wire with a diameter of 100 nm. The tip of gun, close to an anode set at 2-6 kV, produces an electronic field of 10^{10} V/m. As result, the primary electrons are generated and are concentrated to an electron beam of 2 nm. The current emission is controlled by an extraction voltage placed near the field emission tip. The speed of electrons in the column is controlled by the accelerating voltage that in combination with the diameter of current beam determines the resolution.

Within the vacuum column, the electron beam is focused on the surface of the object by an electronic lens. The lens has the aim to collide the electronic beam, whose diameter needs to be smaller than the feature, to process a high-resolution image. As the electron beam impacts on the sample surface, a secondary electron beam is generated. Secondary electrons, collected by a detector, produce a series of electronic signals that are converted into an image and thus displayed to a monitor. The signals derived by the interaction of electronic beam with the sample depend on both elastic and inelastic scattering. While the elastic events do not affect the electron kinetic events, the inelastic events are due to the energy loss from electron beam to the atoms of the sample. Both the scattering events provide information about surface characteristic, crystallography and topography of the sample. Any morphological study is preceded by the surface treatment of the sample in order to make it electrically conductive. The treatment consists of a coating the sample surface, using a separate device, with a thin layer of gold or gold palladium to prevent that the energy from the electron beam charges up the sample surface [165,166].

3.4 Rheometry

Rheometry is an experimental technique to study the rheological properties of materials. The technique allows measuring the response of liquid and solid materials to the deformation applied by external forces. The mechanical response of an ideal viscous fluid to the application of a force is expressed by Newton's law (equation 3.18).

$$\tau = \mu \frac{d\gamma}{dt} \tag{3.18}$$

According to Newton's law, the deformation rate of an ideal viscous fluid $\frac{d\gamma}{dt}$ is proportional to the applied tension τ through a viscosity coefficient μ.

Conversely, the response of non-Newtonian fluids to the applied tension is not linear and the viscosity of fluid is dependent on temperature and pressure.

In rheology, the most common deformation is the shear deformation for the study of rheological properties including steady and complex viscosities, viscous, elastic and complex moduli. An instrument adopted to measure viscosity is the rotational rheometer. It is composed by two parallel plates, between which the sample is located. The sample then is subjected to a controlled stress as a torque, applied by the plates to generate and measure the rotational speed or it is subjected to a controlled rate to measure the torque necessary to maintain a certain rotational speed. In particular, when the rheometer works in controlled stress mode, an oscillating torque applied to the upper plate is converted into a force that acts as a shear stress on a liquid like sample. As the shear stress is applied, the sample flows with a shear rate $\dot{\gamma}$ determined as the product between the angular velocity Ω and the strain constant K_γ, a factor dependent on the measurement of upper plate radius r and the gap between the plates h. The ratio between the applied stress (σ) and the measured strain (γ) is the complex modulus that represents the resistance to deformation or the measure of material stiffness:

$$G^* = \frac{\sigma}{\gamma} \tag{3.19}$$

When the maximum stress and strain are in phase, the phase angle δ is 0°, stress is proportional to strain and the material is purely elastic, as shown in figure 3.2 (a). In figure 3.2 (b) the stress is proportional to strain rate; the material is purely viscous, since stress and strain are out of phase of 90°. A material exhibits a viscoelastic behaviour when 0°< δ< 90°, between the viscous and the elastic modes as reported in figure 3.2 (c).

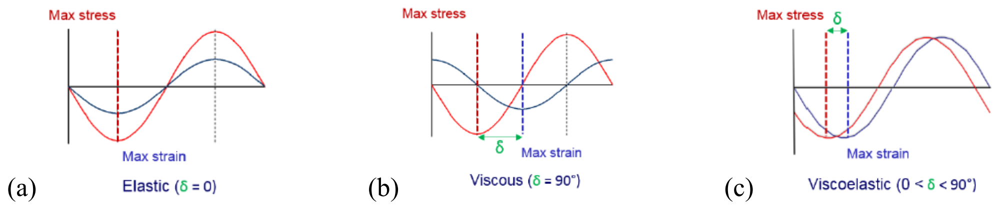

Figure 3.2. Stress and strain relationship for (a) purely elastic, (b) purely viscous and (c) viscoelastic material

The complex shear modulus G* can be defined as the sum of storage modulus G′ that represents the elastic contribution and loss modulus G″, the viscous component that represents the energy loss.

$$G^* = G' + iG'' \tag{3.20}$$

The oscillatory test provides the complex viscosity η* and is expressed as a function of the angular frequency. It represents the total resistance to flow defined as the ratio between the maximum stress applied and maximum strain rate amplitude.

$$\eta^* = \frac{G^*}{\omega} \tag{3.21}$$

Besides, the complex viscosity can be divided in real and imaginary components that are respectively the dynamic (η′) and storage viscosity (η″).

$$\eta^* = \eta' + i\eta'' \tag{3.22}$$

The viscoelastic measurements are performed within the linear viscoelastic region, determined by applying stress or strain in sweep tests. The point, at which G′ becomes dependent on strain or stress, corresponds to the point, at which the structure starts to yield. Above yield stress, the measurement cannot be correlated to microstructural events since the linearity disappears [167].

3.5 Thermal conductivity

3.5.1 Transient plane source (TPS) method

Transient plane source (TPS) or Hot Disk method is a recent technology applied for testing thermal conductivity and thermal diffusivity of thin film specimens with thickness comprised between 10 μm and 1 mm. TPS thin film method involves the use of sensor, named kapton7280, that acts both as heat source and dynamic temperature sensor. The sensor consists of double spiral heating element made of nickel that is covered on both sides by an electric insulating film made of polyimide (Kapton). The probe is then stacked between two thin film samples that are packed on both of sides of a background material with high thermal conductivity. As the sensor is heated electrically by a current pulse, the electrical resistanceas a function of time t (s) increases according to the equation 3.23:

$$R(t) = R_0[1 + \alpha \Delta T_i + \alpha \Delta T(\tau)] \qquad (3.23)$$

R_0 is the initial electrical resistance of sensor at t=0, before the heating, (Ω)

τ is dimensionless time expressed as $\tau = \sqrt{\frac{t}{\Theta}}$ where:

Θ is the characteristic time, defined as $\Theta = \frac{r^2}{a}$,

r (mm) is the radius of sensor and a (mm^2s^{-1}) is the thermal diffusivity of background material.

α is the temperature coefficient of resistivity, (1/K)

ΔT_i is the main temperature across the film, (K)

$\Delta T(\tau)$ is the temperature across the background material (K) as a function of τ.

It is estimated that ΔT_i is constant after very short time $\Delta t_i = \frac{\delta^2}{\kappa_i}$ providing that the film thickness δ is small and the thermal diffusivity κ_i is constant. In addition, assuming that the probe consists of certain circular line sources, the temperature increase of the sample surface can be expressed as reported by equation 3.24:

$$\Delta T(\tau) = \frac{P_0}{\pi^{\frac{3}{2}} r\lambda} E(\tau) \qquad (3.24)$$

where P_0 is the power output of the sensor (W)

λ is the thermal conductivity of the material sample, ($Wm^{-1}K^{-1}$)

r the outer radius of the sensor, (mm)

E(τ) is the dimensionless time function.

From the plot of the temperature increase vs. $E(\tau)$, a straight line is obtained, with the temperature difference across the film ΔT_i as intercept and $\frac{P_0}{\pi^{\frac{3}{2}} r\lambda}$ as the slope of the line. The thermal conductivity can then be according the equation 3.25:

$$\lambda_i = \frac{P_0\,\delta}{(2A\,\Delta T_i)} \qquad (3.25)$$

where δ the thickness of the film and A is the area of the probe [168,169].

3.6 Electrical resistivity measurements

Electrical resistivity is an indicator of the chemical binding changes in the materials and is a parameter inversely proportional to carrier mobility. The method used to detect electrical resistivity depends on the shape and contact resistance of the sample. In this section two probe and four probe point method are discussed.

3.6.1 Two-point probe method

The two-point probe method is a simple technique to measure the electrical resistivity of high resistive sample by the use of a voltmeter as shown in figure 3.3. The electrical resistivity of a specimen with the cross-sectional area A and the length L is determined by the measuring of voltage drop (V) and the current (I) across the sample according to the Ohm's law 3.26 [170-172]:

$$\rho = \frac{VA}{IL} \qquad (3.26)$$

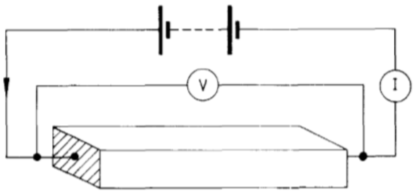

Figure 3.3. Electrical resistivity by two probe method [170].

3.7 Materials

3.7.1 UV-LED curable resin

Ebecryl 150 is the trade name of bisphenol-A-ethoxylate-diacrylate, a bifunctional resin supplied by Allnex (Brussels, Belgium), hereafter coded as EB150; its chemical structure is reported in figure 3.4. It appears as a clear liquid whose density at 25°C is about 1.14 g/ml.

The cured EB150 is a solid 3D network with glass transition temperature of 41°C, tensile strength of 43 MPa, elongation at break of 9% and Young's modulus of 1241 MPa according to the technical datasheet.

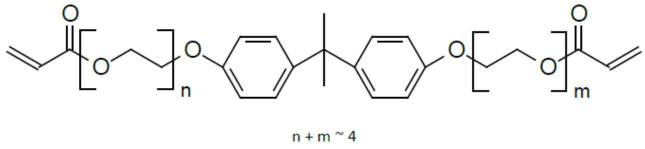

Figure 3.4. Chemical structure of EB150.

3.7.2 Photo-initiator

The photo-initiator, supplied by IGM Resin (Mortara, Italy), is 2,4,6-trimethylbenzoyl-diphenylphosphineoxide, hereafter coded as TPO. It is a phosphine oxide bearing the aryl ketone group that, as a chromophore, is responsible of absorbing the radiation in UV-VIS range, from 370 to 420 nm as shown in the absorbance spectrum of TPO in figure 3.5.

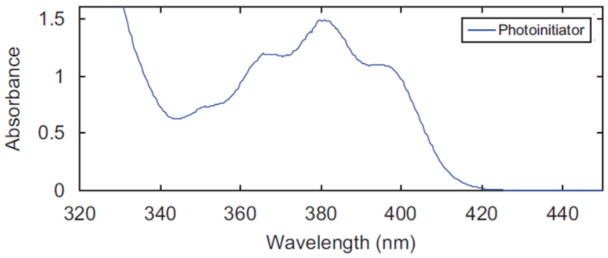

Figure 3.5. Absorbance spectrum of TPO. Reprinted with permission from [10]. Copyright (2008) with permission from Elsevier

Phosphine oxides appear as a yellow powder but, as exposed to the UV light, they become colourless due to the photo-bleaching effect. Since this property provides a further penetration of the radiation in the resin, phosphine oxides are particularly suitable for the depth cure of thick films.

TPO belongs to the Type I phosphine oxides since the absorption of UV radiation involves the cleavage of the weakest carbon-phosphorus bond of the photoinitiator chemical structure, producing two active photoproducts, namely benzoyl and phosphinyl radicals as shown in figure 3.6. As high reactive species, the two radicals are able to trigger efficiently the polymerization with the acrylate species of thermosets in the curable formulations.

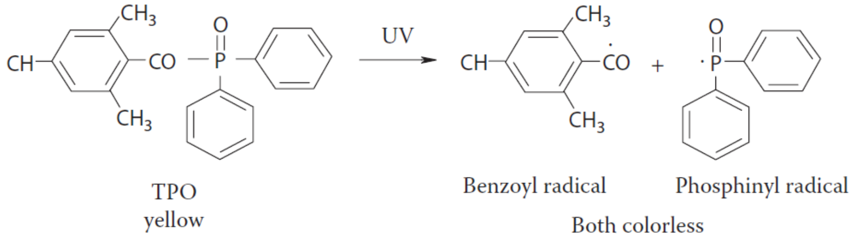

Figure 3.6. Scission of TPO photo-initiator by the absorption of UV radiation. Reprinted with permission from [5]. Copyright (2010) with permission from Taylor & Francis Group LLC.

The photobleancing is attributed to the disappearance of chromophoric group during the absorption of the radiation by the photoinitiator.

3.7.3 Biochar

The Biochar (BC) was obtained through pyrolysis of exhausted coffee powder. Spent coffee grounds, collected from Bar Katia (Turin, Italy), were supplied by Vergnano Spa (Turin, Italy) and correspond to Arabica mixture.

More specifically, the exhausted coffee powder, dried at 105°C for 72h, was pyrolyzed using a vertical furnace and quartz reactor at heating rate of 15°C/min. Then, it was kept at 800°C for 30 min in argon atmosphere.

The carbon and ash contents, evaluated using a static furnace set at 550 or 800°C for 6 h, were of 90 and 8.9 wt.%, respectively [115].

3.7.4 Multi walled carbon nanotubes (MWCNTs)

MWCNTs, NANOCYL®NC7000™, supplied by Nanocyl SA (Sambreville, Belgium), were produced via the Catalytic Chemical Vapor Deposition process. The specific characteristics of NC7000™ are collected in table 3.1.

Table 3.1. Specific characterization of MWCNTs

MWCNTs	Properties	Unit	Value
NC7000™	Average diameter	10^{-9} m	9.5
	Average length	µm	1.5
	Carbon purity	%	90
	Transition metal oxides	%	<1%
	Surface area	m^2/g	250-300
	Volume resistivity	Ω·cm	10^{-4}

3.8 Preparation of UV-LED curable films

The preparation of UV-LED cured films employs a photo-polymerization system that exploits a UV-LED lamp. The exposure array, used in this thesis, is Heraeus Noblelight UV-LED NC1 unit connected to the coating line equipment by a conveyor belt that works in dynamic conditions at a preselected velocity. The selection of belt speed and of the exposure parameters (i.e. irradiance, energy density and wavelength) of the UV-LED lamp depends on the composition and thickness of final product. Belt velocity is a process parameter connected to the energy density or dose that represents the radiant energy emitted by the lamp on the film surface per unit area. As the product between the irradiance and exposure time, energy density is related to the curing time and consequently to the belt speed. This dependence is shown in figure 3.7, in which the energy density is reported, as a function of radiant power, for three selected belt speeds: 100, 150 and 200 cm/min. Since the energy density is linearly dependent on the radiant power, the graph is a straight line, whose slope increases as the belt speed decreases. The data, plotted in figure 3.7, are collected by the use of a radiometer in order to measure the total energy that arrives on the coating surface, exposed to a UV square irradiance level. Since in most cases exposures are not square as in ideal world, probably the energy density, as function of the irradiance power in figure 3.7, are not symmetrically plotted each other according to the different belt speeds.

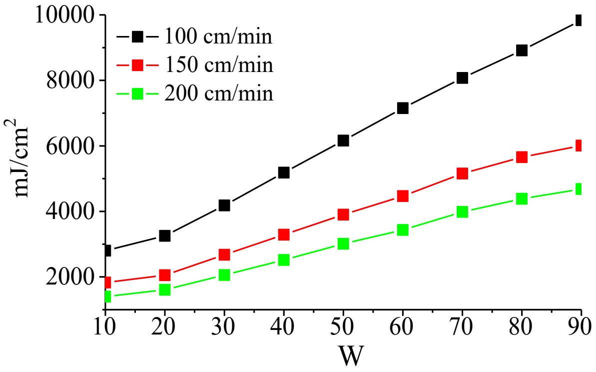

Figure 3.7. Energy density as a function of radiant power at different belt speeds (100, 150 and 200 cm/min).

As it depends on the radiation wavelength of UV-LED lamp, the energy density has a determining role in the curing process since it is absorbed by the photo-initiating species in order to start the radical polymerization. In addition to the energy density, radiant power, wavelength and irradiance contribute to the effectiveness of the curing process. Table 3.2 shows the values of the exposure features selected for the Heraeus Noblelight UV-LED system.

Table 3.2. Specifics of Heraeus Noblelight UV-LED NC1

Specific of UV-LED lamp	Unit	Value
Speed conveyor belt	cm/min	100
Wavelength	nm	395
Radiant power	W	100
Irradiance	W/cm^2	4.8
Energy density (Dose)	J/cm^2	10

Since the spectral output of the UV-LED lamp needs to match with the photo-initiator absorption spectrum, the wavelength at 395 nm is appropriate to generate radical species through the absorption of the incoming radiation by TPO.

The belt speed, at which the energy density is the highest (10 J/cm^2) corresponds to 100 cm/min according to the graph in figure 3.7.

As shown in figure 3.8, the irradiance is linearly dependent on the radiant power.

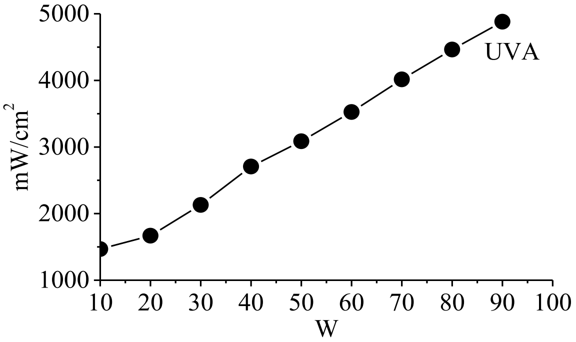

Figure 3.8. Linear relationship between the irradiance and the radiant power.

In order to optimize the desired properties of coating films, the exposure parameters need to be correlated with the content of photo-initiator. On one hand, an excess of TPO in the curable mixture could hinder the penetration of the light through the film, preventing the generation of reactive species and the complete conversion of the acrylic double bonds. On the other hand, an incomplete cure could be caused by a lack of TPO in the curable mixture. Since the conversion of acrylate groups affects the final properties of the coating, a sort of equilibrium can be reached between the content of TPO and the thickness of coating. For a given energy density D, the relation between film thickness Δ_x and TPO concentration at zero time $[TPO]_0$ is expressed by equation 3.27:

$$D = I_0 \Delta t = \frac{\Delta_x}{\Phi \cdot [TPO]_0} \tag{3.27}$$

where Φ is a constant factor [174].

As the energy density of the system is about 10 J/cm^2 and the film thickness of about 150 μm, the complete conversion of curable mixture is reached at 8 wt.% of TPO loading. This loading was identified after several trials performed on UV-LED curable systems containing lower TPO concentrations; 8 wt.% was the optimum photoinitiator content that ensured the obtainment of coating film completely cured and tack-free.

Therefore, the curable mixture is prepared by adding 8 wt.% of TPO to EB150. In order to promote the dissolution of the photo-initiator, the mixture is heated at 80°C for 60 minutes in an oven. Hereinafter, the acrylic resin containing 8 wt.% of TPO will be coded as EB150.

EB150 is then exploited for preparing the curable systems containing the two carbon fillers, Biochar and MWCNTs. With the aim to decrease the particle size, Biochar is previously grinded using a mechanical mixer (Savatec BB90E) at 300 rpm for 10 min [115]. Each single carbon filler is dispersed in EB150 at different loadings (namely, 0.01, 0.10, 0.50 and 1.0 wt.%) using a tip Sonics Vibra-cell ultrasonicator (Sonics and Materials, Inc., Newtown, CT, USA) for 15 min. Since the continuous sonication causes the abrupt increase of mixture temperature, ultrasounds pulse with cycle of 10 s alternating to 10 s pause is imposed.

The procedure is repeated to prepare another set of samples in which Biochar and MWCNTs are added to the EB150 as a mixture of 1:1 weight ratio in order to reach, as total amount, the filler loadings employed for the previous curable formulations: 0.01, 0.10, 0.50 and 1.0 wt.% represent the total amount of the mixed fillers consisting of 50% of Biochar and 50% of MWCNTs. As an example, a total loading of 1.0 wt.% consists of 0.50% of Biochar and 0.50% of MWCNTs.

The three composite systems (EB150 + Biochar, EB150 + MWCNTs and EB150+Biochar/MWCNTs) are stable after four days, since no sedimentation of filler is observed during this time.

All the prepared curable systems are coated on glass plates by using a wire-wound applicator that allows obtaining a film thickness of about 150 μm. The coated film is placed on a conveyor belt of curing line system and subjected to the UV-LED photo-induced process using Heraeus Noblelight UV-LED NC1 unit. The irradiation at 395 nm reaches any point of the sample and in few seconds the liquid curable mixture is converted in a cross-linked 3D solid network.

The type of filler, the loadings in coating films and their corresponding codes are listed in table 3.3. Due to the photobleaching effect, cured EB150 appears as an optically reflective film, whilst composites appear as optically absorbing films because of the presence of the fillers. Furthermore, the lack of microcracks in polymeric structure is index of integrity of the coating films.

Table 3.3. Type of filler and its loading in UV-LED film composites

Filler	Filler loading (wt.%)	UV-LED film coatings
-	-	EB150
Biochar	0.01	EB150+0.01% Biochar
	0.10	EB150+0.10% Biochar
	0.50	EB150+0.50% Biochar
	1.00	EB150+1.00% Biochar
MWCNTs	0.01	EB150+0.01% MWCNTs
	0.10	EB150+0.10% MWCNTs
	0.50	EB150+0.50% MWCNTs
	1.00	EB150+1.00% MWCNTs
Biochar/MWCNTs	0.01	EB150+0.01% Biochar/MWCNTs
	0.10	EB150+0.10% Biochar/MWCNTs
	0.50	EB150+0.50% Biochar/MWCNTs
	1.00	EB150+1.00% Biochar/MWCNTs

3.9 Characterization techniques

In order to evaluate the effectiveness of the curing process and the influence of Biochar and MWCNTs on morphology, thermal, mechanical, optical and electrical properties, the liquid dispersions or the obtained films were subjected to different characterization techniques as detailed in the following.

3.9.1 ATR-FTIR spectroscopy

ATR-FTIR spectroscopy was performed to evaluate the conversion of double bonds, characteristic of the acrylic groups of the resin.

This analysis provided the absorption spectrum both of the liquid resin, before the exposure to the UV-LED light, and of the cured coating films. ATR-FTIR spectroscopy does not require a specific preparation of the samples: small amount of the curable liquid resin or of the coating film are placed in contact with the crystal, from which the wavenumber range of the absorption spectrum and penetration depth of radiation are dependent on.

The analysis, performed by the use of a Perkin Elmer Spectrum 100 spectrophotometer (Shelton, Connecticut, USA), involved a MIR source and a diamond probe crystal with a depth penetration at 45° of 1.66 μm. The FTIR spectra of both uncured resin and cured film composites were collected at wavelengths from 700 to 4000 cm^{-1}, with 4 cm^{-1} resolution and 16 scans, aiming at comparing the peak intensities of acrylic double bonds in the systems, before and after the curing process.

3.9.2 Field Emission Scanning Electrical Microscopy (FE-SEM)

FESEM technique allowed investigating the degree of fillers dispersion in the polymer networks. Since the morphological analysis involved the fractured surface of the cured films, it requires a specific preparation of the samples: some strips of coating films are cooled in liquid nitrogen in order to avoid structural damage by plastic deformation and then subjected to fragile fracture, transversely to the length of the strips. The fractured surface of film samples was then coated with a thin layer of Au to be able to conductive for current and, placed on adhesive tape, it was studied using a Zeiss Supra-40 (Carl Zeiss IMT, Oberkochen, Germany) apparatus.

3.9.3 Rheological measurements

An ARES (TA Instrument, New Castle, DE, USA) apparatus was used to investigate the effect of the different fillers on the rheological properties of the acrylic resin.

The selected operating conditions take into account the features of the uncured thermosetting resin subjected to rheological study. As the viscosity of the ethoxy-acrylate resin was assessed, the geometry size and diameter of the plates was selected appropriately. Moreover, the working range of the operating conditions, frequency and strain, were optimized in order to perform the measurement within the linear viscoelasticity of the sample.

Rheological measurements, performed in strain-controlled mode, provided information about complex viscosity, storage and loss moduli. The rheometer worked with a parallel plate (diameter: 25 mm) geometry. As the composite resin was placed on the lower plate, the upper plate was moved downward and the strain sweep test was completed at angular frequency ω=1 rad/s and 30°C.

In order to determine the variation of complex viscosity, storage modulus and loss modulus, frequency sweep tests were performed from 10^{-1} to 10^{-2} rad/s. Each measurement run, repeated two times, was carried on within linear viscoelastic region at a selected strain amplitude. The data, collected and averaged by a software, had a standard deviation below 5%.

3.9.4 Differential scanning calorimetry (DSC)

Differential scanning calorimetry measurements were performed by means of a QA 1000 TA Instrument apparatus (TA Instrument Inc.,Waters LLC, New Castle, DE, USA), using sealed aluminum pans. The analysis has the aim to provide information about the phase transition of the cured film subjected to a controlled thermal program. The operating conditions were selected according the available knowledge about the neat cured resin: as acrylic thermosetting materials, the samples are characterized by a glass transition temperature, expected between 50 and 70°C. In order to eliminate the contribution of the relaxation enthalpy, attributed to the speed of curing process, the samples were subjected to the following thermal cycle: after the first heating, the cured films were cooled and heated again. In the second heating run, the variation of the heat capacity corresponds only to the glass transition temperature since the molecules rearranged in a lower and more stable energy conformation.

As the operating condition were assessed, the thermal analysis was performed. About 8 mg of samples were analyzed under dry N_2 gas flow at 50 mL/min, according to the following cycle:

(1) heating from 0 to 160°C at 10°C/min;
(2) cooling down to 0°C at 10°C/min;
(3) heating from 0 to 160°C at 10°C/min.

Tg was calculated as the midpoint of the specific heat step.

3.9.5 Thermogravimetric analyses (TGA)

Thermogravimetric analyses (TGA) were performed using a Pyris1TGA apparatus (Perkin Elmer, Waltham, MA, USA; experimental error: ± 0.5 wt.%, ± 1°C). This analysis aims at investigating the thermal or thermo-oxidative stability of the cured film monitoring the mass variation of the sample that, under a stable flux of gas, is subjected to a temperature ramp. The analysis was carried both under inert and oxidative condition: the decomposition of the sample occurs as the temperature increases. The comparison between the neat sample and the composite films allows investigating the effect of the fillers on the thermal and thermo-oxidative stability of polymer network. To this aim, small amounts of the cured films (about 11 mg), placed in alumina pans, were subjected to the thermal program ranging from 50 to 700°C with a heating rate of 10°C/min under both N_2 (35 mL/min) and air (25 mL/min) flow.

The thermogravimetric curves allowed determining $T_{5\%}$ and $T_{10\%}$, i.e. the temperatures, at which 5 and 10% weight loss occurs, respectively, the T_{max} values (corresponding to the peaks in dTG curves) and the residues at 700°C.

3.9.6 Dynamic mechanical thermal analysis (DMTA)

The dynamic mechanical thermal analyses were performed using DMTA Q800 from TA Instruments (New Castle, DE). The analysis was carried out on the specimens obtained cutting, from the cured films, some strips of rectangular bar shaped having the same size (6 mm width and 30 cm length). For each material, four tests were performed, working in multi frequency-strain operation mode. In order to deform the material within its linear viscoelastic region, frequency, thermal program and strain, were selected suitably and applied to all the samples. The average of the four specimens processed provides the viscoelastic behavior of each material.

The multi-frequency mode was employed for assessing viscoelastic properties as a function of frequency. The samples were subjected to a strain of 0.05% while the oscillating amplitude was held constant at 1 Hz; the analyses were performed from room temperature to 120°C, with a heating rate of 3°C/min.

3.9.7 Thermal conductivity

Thermal conductivity measurements were performed using transient plane source (TPS) method with TPS 2500S apparatus (Hot Disk AB, Göteborg, Sweden) consisting of a Kapton as insulated disk elements (radius of 3.189 mm) and a double spiral of nickel as sensor element. The test temperature was held constant (23°C ± 0.01°C) using a silicon oil bath (Haake A40, Thermo Scientific Inc., Austin, TX, USA) with a temperature controller (Haake AC200, Thermo Scientific Inc., Austin, TX, USA). The accuracy of the test, related to the operating conditions, was improved matching the applied electrical power and the measurement time respectively at 0.5 W and 40 s. The TPS method does not require the pretreatment of the samples, as the hot disk sensor heated electrically was sandwiched between two identical coating films. When the samples reached the thermal stability, after about 15 minutes, the analysis was performed: the sensor heated the specimens, whose temperature variation was monitored over the imposed time by the software. The thermal conductivity of the sample resulted from the average of four measurement points, collected on the same specimens.

3.9.8 Electrical conductivity

The electrical measurements were carried out using “Two Point Probe (TPP)” method. To this aim, insulated copper micro-wires were used to connect Ag paste to the cured film samples of rectangular bar shaped. A Keithley-238 High Current Source Measure Unit was used as nano-amperometer at high voltage source.

3.9.9 UV-vis spectroscopy

A Shimadzu UV-Vis spectrophotometer UV2600 series (Shimadzu Italia S.r.l., Milano, Italy) was employed to perform the UV-vis spectroscopy measurements, in order to verify the UV transparency of the cured film samples in wavelength range between 200 and 1200 nm. The analysis was performed in transmittance mode: the samples (thickness about 150 microns) of rectangular bar shaped were directly placed in the cell compartment of the instrument without pretreatment, using air as reference.

Chapter 4

Results and discussion

Preliminary investigations

4.1 Photo-polymerization process

The curing process of the acrylic system is dominated by a radical driven polymerization mode. Radicals have a determining role to convert a low molecular weight liquid monomer into high molecular weight polymer network. The principle of photo-activated process is described in figure 4.1 where TPO, by the absorption of UV-LED radiation, generates free radicals that promote the polymerization reaction with monomer molecules of EB150. The reaction ends when a cured network is obtained as result of the conversion of characteristic double C=C bonds in the chemical structure of acrylic resin into a new single C-C bond in the polymeric cross-linking structure.

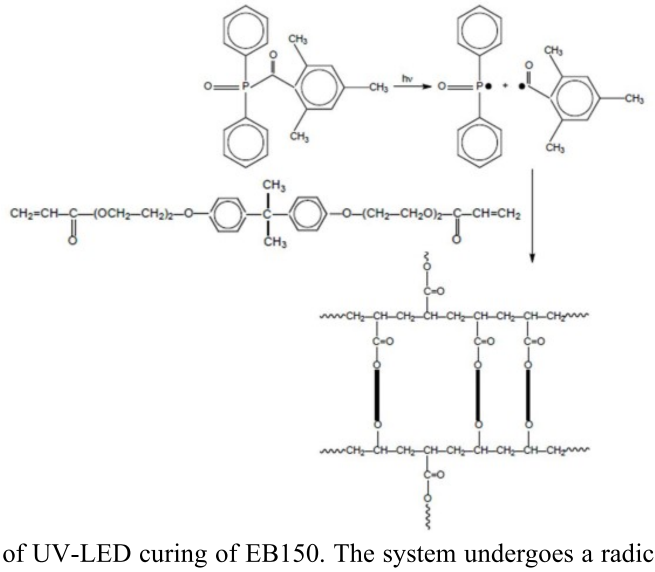

Figure 4.1. Scheme of UV-LED curing of EB150. The system undergoes a radical polymerization promoted by the generation of primary radicals derived from the photolysis of the photo-initiator as a consequence of the exposure to the UV-LED radiation.

The effectiveness of the curing process, in terms of double bond conversion and polymerization rate, is dependent on the synergic correlation between the chemical composition of curable formulation (i.e. TPO concentration and filler loading) and exposure factors (i.e. energy density and wavelength of UV-LED lamp). As the amount of unsaturated acrylic groups corresponds to unreacted species, the effectiveness of light-induced process can be considered proportional to the conversion of double bond acrylic group. Among analytic methods, FTIR-ATR spectroscopy is suitable to estimate the completeness of curing process as it is effective to detect the changing of functional groups in the chemical structure.

In the absorbance spectrum, the characteristic band of acrylic group at 1635 cm^{-1} was considered to evaluate the conversion of curable mixture, from liquid resin to highly cross-linked network. Figure 4.2 shows the FTIR-ATR spectra of EB150 containing 0.50% of Biochar before (A) and after (B) the UV-LED curing process: the peak at 1635 cm^{-1}completely disappears after the exposure to the UV-LED radiation, proving the completeness of double bond conversion and, therefore, the effectiveness of the operating conditions used for the UV-LED curing process.

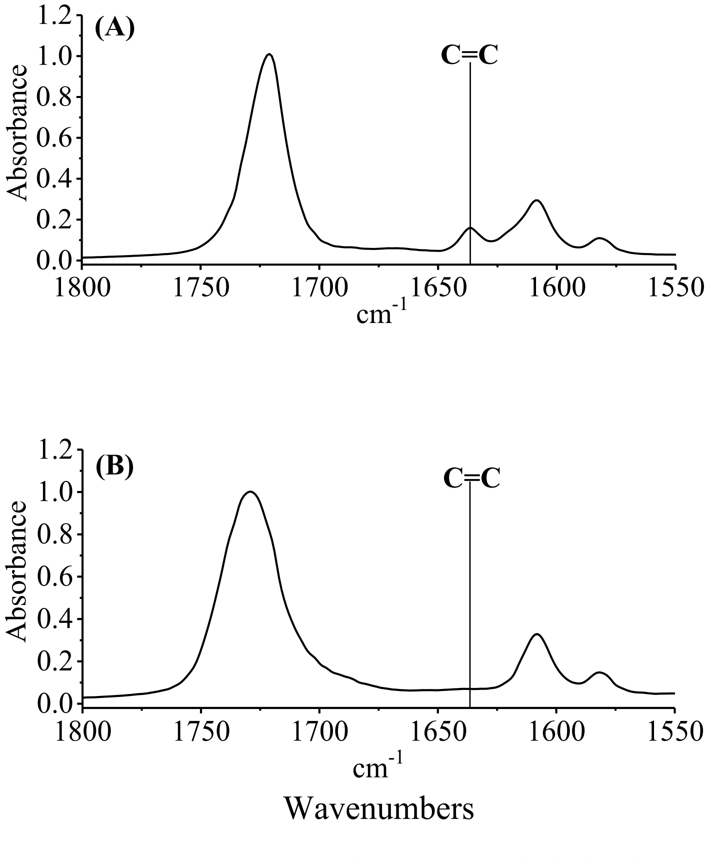

Figure 4.2. FTIR-ATR spectra of EB150 containing 0.50 wt% of Biochar, before (A) and after (B) exposure to the UV-LED radiation. The flattening of the band of the acrylic double bonds, located at about 1635 cm^{-1}, is a clear indication of the completeness of the UV-LED curing process.

Furthermore, the FTIR-ATR spectra highlight that the presence of filler in curable formulation does not affect the efficiency of the curing reaction since both of Biochar and MWCNTs at different loadings do not limit the penetration of the UV-LED light [3]. Since the filler does not hinder the progress of curing, the whole set of cured film composites shows the same spectroscopic behaviour: the acrylic double bond results undetectable after the exposure to the UV-LED light as shown for the sample with 0.5% of Biochar. Since the peak irradiance is focused on 4.8 W/cm^2, the coating film exposed to a UV-LED light source receives for 2 seconds an energy density of 10 J/cm^2, according to the exposure conditions depicted in the third chapter.

In addition to a qualitative analysis, FTIR-ATR technique provides a quantitative value since it allows determining the conversion degree by the integration of the double bond band area of the uncured formulation A_0 and the cured coating film A_D according to the following equation:

$$C_D = \frac{A_0 - A_D}{A_0}$$

The relation above confirmed that the degree of conversion for both unfilled and filled composite films is about 96%, as expected.

4.2 Morphological characterization

4.2.1 Morphology of Biochar and MWCNTs

The morphology of the two carbon-based fillers was investigated by FESEM in order to evaluate their micro-scale features (i.e. size and shape). The micrographs, collected at different magnification, are shown in figure 4.3, where the morphological structure of the Biochar (a-b) and MWCNTs (c-d) is evident.

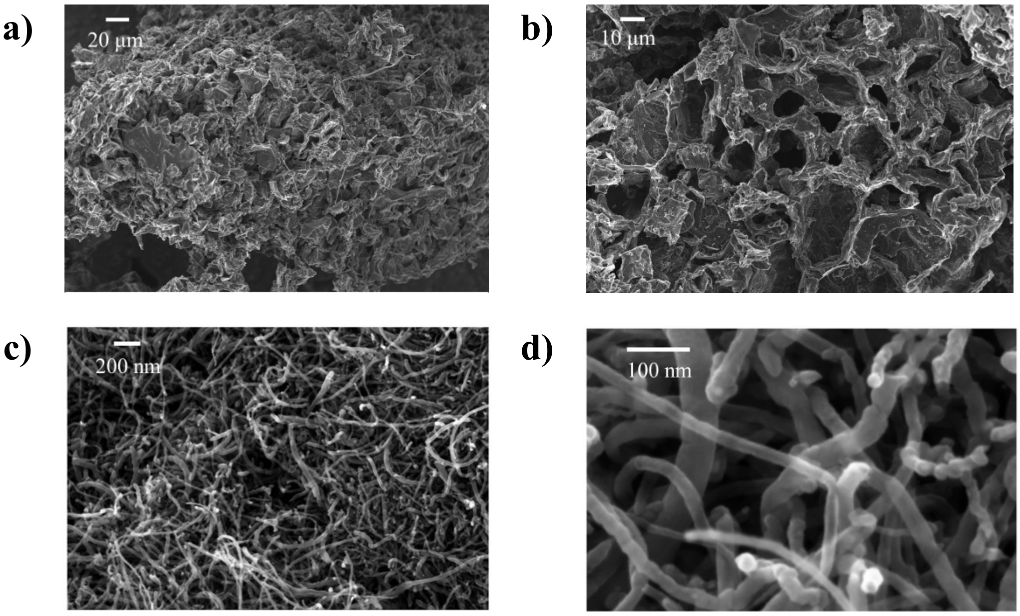

Figure 4.3. FESEM captures of Biochar (a,b) and multiwalled carbon nanotubes (MWCNTs; c,d) at different magnifications. It is worthy to note the highly porous structure of Biochar.

Since their different precursors and chemical processing treatments, the two fillers appear extremely different in size and shape.

Biochar, as product of pyrolysis of spent coffee grounds, is affected by the operating conditions. Besides, the morphological structure of the Biochar is strictly dependent on the temperature. As reported by *Giorcelli et al.*, Biochar morphology varies from a flaked collapsed structure to a porous architecture according to the processing temperature [115]. The first structure, at relatively lower temperature, is promoted by the release of volatiles; the second one is a carbonaceous structure derived by the degradation of lignin, cellulose and hemicellulose at highest temperature due to the release of higher amounts of gaseous products [115]. Such sponge-like porous structure characterizes the employed Biochar, in which any single grain, with size of 200-300 µm, displays pores with average radius of about 10-15 µm. The pores are separated each one by carbon lamellae having a thickness between 1 and 2 µm as micrographs in figure 4.3 (a-b) reveal. According to the International Union of Pure and Applied Chemistry (IUPAC), the FESEM micrograph shown in figure 4.3 (b) shows macropores since their diameter is larger than 50.0 nm. The porosity is one of the most important properties of Biochar, as it is correlated to other physical properties, including the specific surface area (SSA) that represents the total surface area per gram (unit: m^2/g) and depends on the distribution of size and volume pores: as the size and distribution of pore increase, the specific surface area increases as well [78]. A high value of specific surface area provides several advantages when Biochar is employed as filler in polymer matrix. *Khan et al.* found superior mechanical properties for composites reinforced with Biochar. The high mechanical performance was attributed to the transfer of the applied stress from the polymer to the Biochar particles, due to its high specific surface area that contribute to improve the adhesion and dispersion of the filler in polymer matrix. On the other hand, the high surface area of the particles was responsible for the generation of agglomeration at higher filler content (i.e. 2 wt.%) [113]. In order to increase the surface to volume ratio and allow achieving a good dispersion in the polymer matrix at the highest loadings, Biochar was subjected to a ultrasonication treatment to reduce the particle size. The increasing of surface to volume ratio plays a key role to enhance the properties of nanocomposites that are dependent on the interfacial interaction with the polymer matrix.

As shown in figure 4.3 (c-d), MWCNTs micrographs are agglomerates of entangled, curved and intertwined tubes that deviate from the idealized cylinder shape. The agglomerates, attributed to the CVD synthesis process, are promoted by physical entanglements due to structural defects resulting from the growth process of MWCNTs and the action of van der Walls forces among the nanotubes. Besides, the strength between agglomerates increases with increasing the purity of MWCNTs in comparison with nanotubes characterized by amorphous structure on their surface [175]. FESEM images show that MWCNTs, in the characteristic “combed yarn” structure, have a highly variable average diameter ranging from 10 to 50 nm, a length in the order of magnitude of micro-meters and they arrange in micrometric scale agglomerates (more than 1μm). The arrangement of MWCNTs affects their dispersion in the polymer matrix, since the high cohesive strengths among the nanofillers compromise the interaction between polymeric chains and carbon nanotubes, as well as the quality of final composites. Furthermore, MWCNTs diffuse in hydrophobic polymeric resin forming secondary agglomerations (clusters) that contribute to reduce the interface between nanofiller and the host material. Among the techniques suitable to disperse efficiently MWCNTs in liquid polymeric matrix, ultrasonication is the most common method, as it is able to disintegrate the secondary agglomerations. Ultrasonication is a mixing method that exploits high shear loads generated by micrometrical air bubbles that are able to fragment the clusters of MWCNTs. The shear forces, able to overcome the van der Walls forces, allow improving the dispersion of MWCNTs, leading the disentanglement of agglomerates and improving the distribution in acrylic polymeric resin without compromising the size of the nanofillers [24].

4.2.2 Morphology of cured coating composites

The morphological analyses on the fractured surfaces of the coating film composites shown in figure 4.4 have, firstly, the aim to illustrate and investigate the effect of the ultra-sonication on the dispersion degree of the filler in the polymer matrix, as well as the influence of the filler on polymeric structure network. To this aim, the fractured surface of the unfilled coating film (EB150), shown in figure 4.4 (a,b), is compared with the polymer based composites at 1 wt.% of Biochar (c), 1 wt.% of MWCNTs (d) and 1 wt.% of the mixture containing Biochar and MWCNTs (e). The micrographs reveal that ultrasonication is suitable to disperse uniformly the filler in the polymer matrix: local nanometric agglomerates appear in the system containing MWCNTs, whose dispersion improves in the hybrid system where the nanofillers are combined with the Biochar.

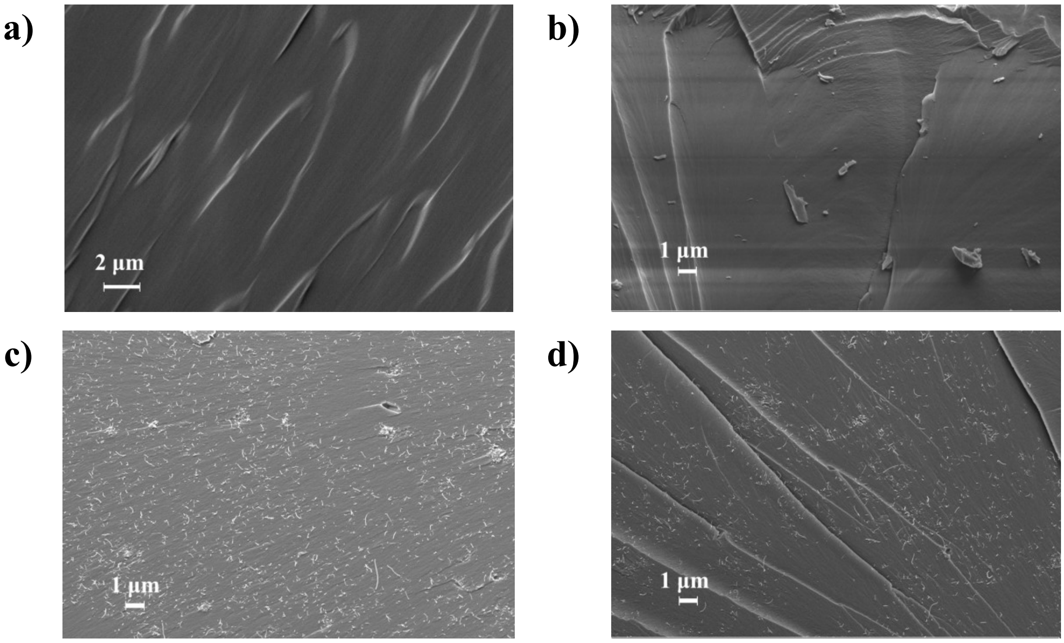

Figure 4.4. FESEM captures of UV-LED cured films (filler loading: 1 wt%): unfilled EB150 (a); EB150 + Biochar (b); EB150 + MWCNTs (c) and EB150 + Biochar/MWCNTs (d). All the filled UV-LED cured films show a good dispersion of the two carbonaceous fillers.

The micrographs in figure 4.5 at higher magnifications provide details on the filler dispersion and the fracture behaviour of the coating composites. The micrographs in figure 4.5 (a,b) display the fracture surface of the unfilled sample that shows the river lines typical of the brittle fracture that, in appearance, is retained in the crack region of the analysed film composites. However, the presence of the filler in polymer matrix affects the fracture behaviour of the composite films: the smooth and uniform surface of the neat film is not found in the composite films.

The micrographs depicted in figure 4.5 (c,d) indicate that Biochar, anchored in the polymeric resin, hinders the propagation of cracks and promote the surface mechanical interlocking [176,177]. The Biochar results homogeneously dispersed in the matrix since during the compounding process the uncured resin could get into the macro-pores of the Biochar, hence forming an interconnecting network. Furthermore, the porous structure of the Biochar provides continuity between the interphases, which the toughness fracture behaviour of the composite films is dependent on [178]. Because of its non-polar nature, the Biochar results in good affinity with the hydrophobic organic matrix in which it is well incorporated thanks to the strong van der Waals forces that act between the filler and the host polymeric matrix. These forces allow protecting the polymeric matrix as the stress is absorbed by the Biochar particles and, thus, limit the molecular movements of the polymer chains [177,179].

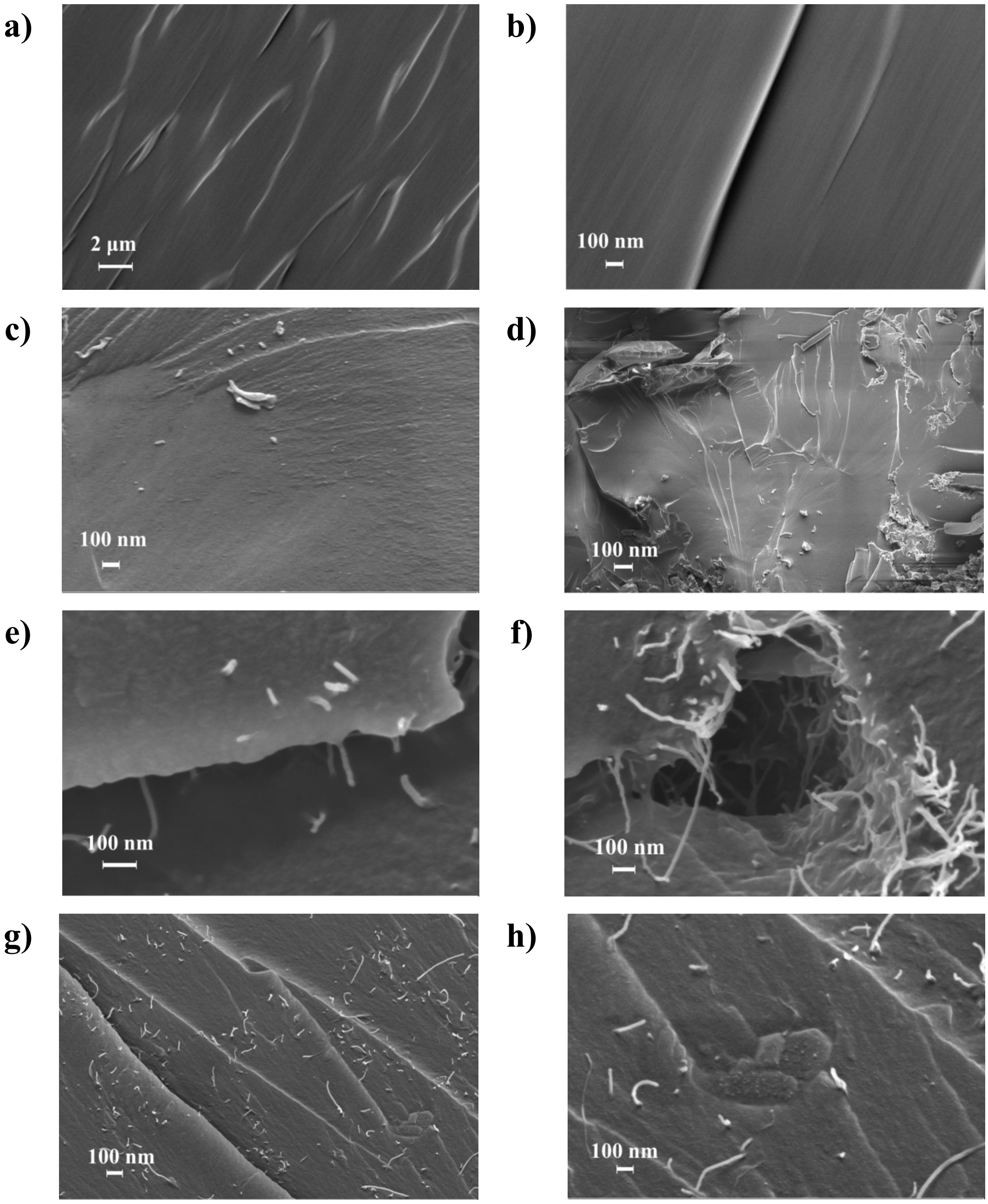

Figure 4.5. FESEM micrographs of UV-LED cured films show: the brittle fracture of the unfilled EB150 (a,b); the interconnecting network of Biochar based composites at 1.0 wt.% (c,d), the toughness fracture of MWCNTs containing composites at 1.0 wt.% (e,f); the shuttle effect of the Biochar in hybrid systems provides the disentanglement of MWCNTs agglomerates (g,h).

The micrographs in figure 4.5 (e,f) show the surface fracture of MWCNTs reinforced sample and the influence of the filler on the brittle behaviour of the acrylic resin. The use of MWCNTs as filler is well established, because of their remarkable interfacial properties and the increasing in mechanical performance of the host polymeric matrix. The improving of the fracture toughness is the main effect of the addition of MWCNTs in the thermosetting resin. The toughness behaviour of the MWCNTs containing sample is ascribed to the pull-out mechanism based on the propagation of the fracture in correspondence of the carbon nanotubes [180]. As shown in figure 4.5 (f), the propagation of the fracture involves the separation of the MWCNTs from the polymeric matrix as a result of the energy absorbed by the filler. As the separation occurs, the constraint in the matrix are relieved and plastic voids are generated. As a consequence of the pull-out mechanism, figure 4.5 (e) shows the bridging effect that occurs during the fatigue crack. Both the pull-out and bridging effects, as result of the energy absorption, are responsible for the increasing of the toughness. However, the reduction of the carbon nanotubes length can be attributed to a fracture process induced by the friction between polymer and the MWCNTs, rather than by a pulling out effect [181]. Furthermore, the fracture surface reveals a certain degree of curvature of the MWCNTs that, by the overlapping contact points, contributes to the generation of a conductive network due to the tunnelling effect [182]. This effect is induced by the percolation behaviour of the MWCNTs that form an interconnected network at a certain filler loading known as percolation threshold. However, the electrical percolation could involve the formation of network MWCNTs agglomeration [183]. The presence of local agglomerates visible in micrograph in figure 4.5 (f) could have a detrimental effect on the mechanical and thermal properties. These drawbacks could be overcome by exploiting the synergistic effect of MWCNTs and Biochar that can be used to develop a hybrid system. The idea is to combine the advantages of the two fillers in order to improve the overall performance of the polymeric composites. Since in literature the combination of two fillers is well-established to improve the desired properties of thermosetting composites, in the present thesis the ternary system Biochar/MWCNTs/EB150 was investigated [184-186].

Figure 4.5 (g,h) shows the fractured surfaces of the acrylic system, in which Biochar and MWCNTs (weight ratio 1:1) are incorporated. As expected, Biochar improves the dispersion of MWCNTs in acrylic resin because of the absence of aggregates. The improvement in dispersion of MWCNTs within the acrylic resin is ascribed to the shuttle effect of Biochar that provides the disentanglement of the nanofiller agglomerates and favours their dispersion in the polymer matrix. The shuttle effect of Biochar can be attributed to its aromatic nature: the graphitic structure of the Biochar interacts, through van der Waals forces, with that of MWCNTs. The junction between the two graphitic structures, promoted by the π-π interaction, is the result of the bridging effect of MWCNTs between the adjacent particles of Biochar. Both Biochar and MWCNTs are embedded in the acrylic resin where a new conductive network can take place with the MWCNTs acting as flexible pathway between the high surface area of Biochar particles. Besides, these particles provide the shortcutting effect of the nanofiller length, therefore the distance between MWCNTs is not constant in the polymeric network.

4.3 Rheological behaviour

Rheological characterization is an effective method to assess the correlation between structure-properties of polymeric composites. The rheological response of the composites, subjected to the external forces, depends on the filler dispersion in polymer matrix, polymer-filler interaction and the imposed stress. Besides, the incorporation of the filler in polymer matrix significantly affects both viscoelastic behaviour and steady shear viscosity [24].

In order to investigate the effect of the filler on the rheological properties of the uncured thermosetting resin, complex viscosity of the unfilled EB150 is compared with that of composite curable mixtures. In figure 4.6 (a-c), the complex viscosity of EB150 and its mixtures at different loadings of Biochar, MWCNTs and Biochar/MWCNTs is plotted as a function of the frequency.

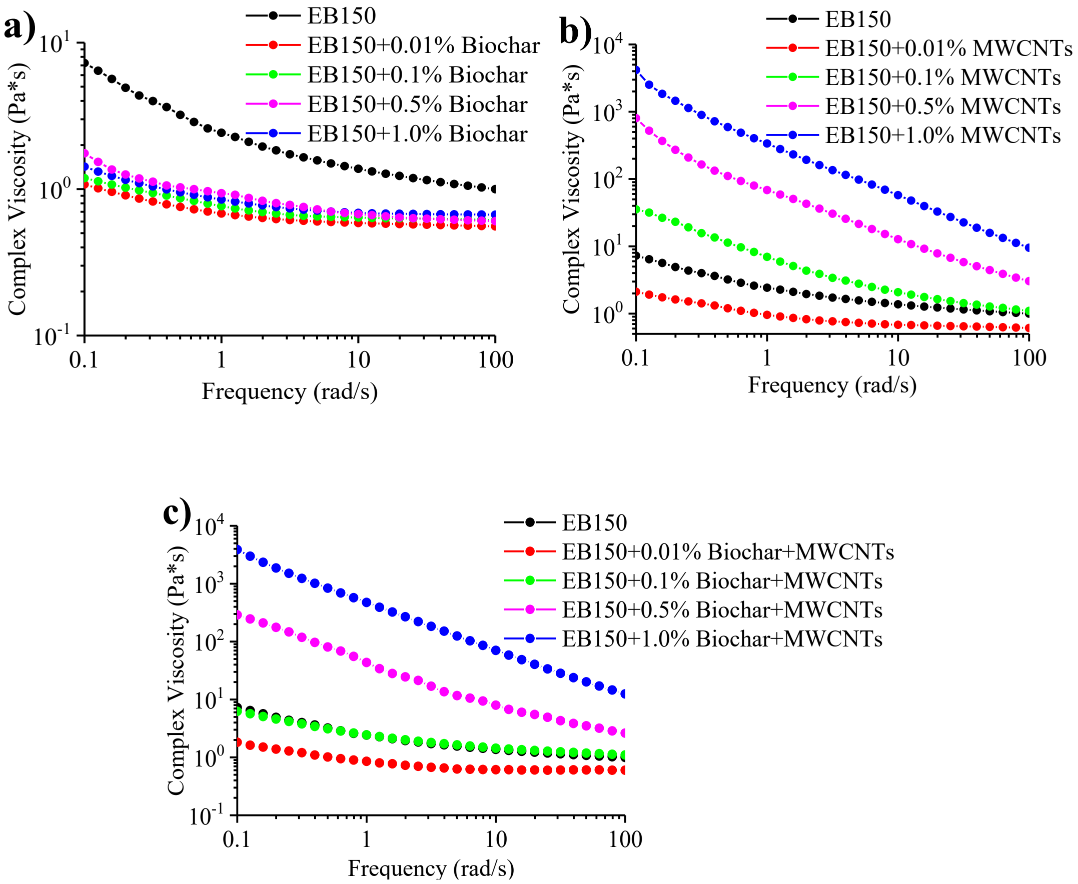

Figure 4.6. Complex viscosity vs. frequency curves for unfilled EB150 and EB150/Biochar (a) and EB150/MWCNTs (b) and EB150/Biochar+MWCNTs (c) at different loadings ranging from 0.01 to 1.00 wt.%.

The rheological measurements reveal that the complex viscosity is affected by the content and morphology of the fillers. The unfilled resin shows a pseudo-plastic behaviour, since the complex viscosity decreases as the shear strain amplitude increases. This characteristic, known as "shear thinning", is typical of non-Newtonian fluids with viscoelastic properties [187]. However, from low to high frequencies, the difference of complex viscosity is about one order of magnitude. As the filler is added to the resin, the complex viscosity of EB150 changes according to the morphology and loading of the fillers.

With respect to EB150, the Biochar containing dispersion causes the decreasing of about one order of magnitude of the complex viscosity, regardless of the filler content. The decrease of complex viscosity is ascribed to the destruction of the intermolecular bonds between the filler particles and the polymer matrix, formed in the liquid dispersion. As the shear force is applied, the distance between Biochar particles increases since the rolling of the filler particles promotes the flowing of the polymeric chains and the decrease of complex viscosity. As the shear rate increases, the interaction between the particles decreases, meanwhile the complex viscosity decreases as well, because of the effect of the shear thinning behaviour. Unlike the unfilled resin, the shear thinning behaviour is limited at the lowest frequencies: in fact, the complex viscosity slightly decreases up to 10 rad/s, after that it remains constant, reaching a sort of equilibrium at about 0.6 Pa*s.

In addition to the interlocking between fillers and polymeric matrix, also the filler size affects the rheological behaviour of the thermosetting composites [188]. This correlation is revealed by the comparison of the system containing Biochar with that containing MWCNTs: being equal the filler loading, from micro- to nano-fillers the complex viscosity of the liquid formulation increases. Thanks to the nanometric size and the higher surface area of MWCNTs, keeping the same filler volume, the number of particles increases as well as the interactions between filler particles and polymer matrix and among the filler particles [188]. As the filler loading increases, the interaction between MWCNTs increases as well as the viscosity of the formulation. In particular, in the system containing MWCNTs, the complex viscosity increases by three order of magnitude as the filler content increases from 0.1 to 1.0 wt.%. However, at 0.01 wt.% of MWCNTs, the weak matrix-filler interaction prevails on the effect of particle size and the complex viscosity decreases below that of unfilled resin. In addition, from the lowest to the highest filler loadings, the shear thinning behaviour becomes stronger: the addition of MWCNTs in thermosetting resin provides a viscoelastic behaviour as result of the formation of a microstructured component [189,190]. Thanks to their shear thinning effect, the MWCNTs dispersions show non-Newtonian behaviour, correlated to the filler particles interaction. As the filler content increases, the inter-particles interaction becomes stronger and it generates a 3D network that allows the yielding transition. Due to the non-Newtonian and viscoelastic effect, the microstructure in the liquid formulation can be dismantled in shear flow promoting the disentanglement of the MWCNTs aggregates and the shear thinning behaviour as a result of MWCNTs deflocculation [187,190]. Besides, at the highest frequencies, the difference between the composites formulations and the unfilled resins diminishes as a similar dispersion occurs at greater frequency shear. Furthermore, the lack of Newtonian plateau indicates that the MWCNTs composite dispersions, regardless of the filler loading, show a solid-like behaviour at rest as consequence of microstructure network [191]. In addition, in the system containing MWCNTs ranging from 0.1 to 1.0 wt.%, the higher complex viscosity at higher shear rate is ascribed to the formation of percolated structure formed by carbon nanotubes. As the shear rate increases, the percolated structure breaks down and at the highest frequencies the viscosity becomes similar for all the analysed dispersions [190].

A similar trend is detected also in the hybrid acrylic system containing both Biochar and MWCNTs. However, the complex viscosity of the liquid formulation shows two main trends as a function of the shear rate: one approaches that of EB150 at low filler loadings and the other is close to EB150+1.0% MWCNTs at high filler loadings. At the lowest filler loading, the negligible amount of both Biochar and MWCNTs promotes the decrease of complex viscosity below that of EB150 as observed also for the dispersions containing Biochar or MWCNTs at 0.01 wt.%. The synergistic action of the lubrication effect of Biochar and the MWCNTs-polymeric matrix interaction at the lowest filler content, are responsible for the decrease of the complex viscosity. As the content of Biochar and MWCNTs mixture increases up to 0.1 wt. %, the complex viscosity increases as well, and its trend, as a function of the frequency, overlaps that corresponding to the unfilled resin. Compared to the MWCNTs containing system with the same filler content, the hybrid formulation shows a lower complex viscosity. This behaviour is ascribed to the shuttle effect of the Biochar on the MWCNTs particles: the interaction between the graphitic structure of the two carbon fillers promotes the dispersion of MWCNTs in the acrylic system and the interaction between fillers and polymer matrix. For the dispersions containing Biochar and MWCNTs from 0.1 to 0.5 wt.%, the complex viscosity increases by two order of magnitude; meanwhile, the stronger shear thinning behaviour is ascribed to the formation of an interconnected network. This effect, attributed to the prevailing effect of MWCNTs aggregation, is intensified at the highest filler loading since the complex viscosity increases by one order of magnitude with respect to the system containing 0.5wt.% of the two carbonaceous fillers. In both cases, the high shear rates favour the dispersion of MWCNTs aggregates: in fact, the complex viscosity of composite formulation approaches that of the unfilled resin tested at the lowest frequency.

Chapter 5

Thermal properties of the UV-LED cured films

5.1 Differential scanning calorimetry (DSC) analyses

DSC analyses is a valuable technique to study the structural relaxation and glass transition temperature (T_g) of the amorphous polymers, subjected to a controlled temperature program. The thermal transitions of polymeric material are detected in a thermogram where the heat difference between the reference and the sample is plotted as function of the temperature. The thermograms shown in figures 5.1, 5.2 and 5.3 refer to the composite films at different loadings of the Biochar, MWCNTs and the mixture of Biochar/MWCNTs respectively, in comparison with unfilled EB150. Since thermosets polymers are infusible materials, no endothermic phenomena are detected upon the glass transition temperature during the first and second heating ramp. This behavior has been observed for all the analyzed samples.

The cross-linked nature and the glassy state of the samples are the main aspects of the UV-LED cured films that are subjected to a structural relaxation through the glass transition region. The structural relaxation is attributed to the glassy nature of the amorphous materials that evolves from non-equilibrium to a meta equilibrium state during the heating process. This conversion leads the rearrangements of the molecular segments promoted by the free volume and the molecular mobility of the polymer chains. Such evolution can be monitored in terms of enthalpy and T_g, correlated to the thermal histories of the material that is subjected, during the thermal analysis, to a temperature program in static or dynamic condition. The T_g values of thermosets are affected by the crosslinking density, length of the chains between crosslinks and possible unreacted species within the polymer network. As heating occurs, thermosets undergo to the enthalpy relaxation through the T_g region characterized by a non-equilibrium state. The T_g, corresponding to the polymeric transition state from glassy to viscous-liquid behavior, provides a reversible change of physical properties including modulus, heat capacity and elasticity. The mobility of the polymeric chains affects also the heat capacity: approaching to the T_g, the molecular groups, absorbing potential and kinetic energy, are able to rearrange in a low energy conformation. As the heat capacity increases, in correspondence of the T_g, a second order transition occurs: no heat is generated or absorbed but a change in mechanical properties is observed.

The DSC thermograms reported in figures 5.1-5.3 show an endothermic peak, in the first heating ramp, superimposed to the T_g as the effect of the structural relaxation. The relaxation structure of the glassy state is known also as enthalpy recovery: during the heating, the sample is subjected to the recovery of enthalpy and the network structure approaches to the liquid equilibrium as consequence of the chain mobility. The relaxation process occurs to relieve the excess of the molecular stress, attributed to the fast UV-LED curing process that has frozen the polymer chains into an unfavorable high energy conformation. The degree of relaxation process can be evaluated by measuring the excess of enthalpy of the endothermic curve.

The DSC trace provides a discontinuity of heat capacity in correspondence of T_g, detected at the inflection curve point. The endothermic peak, superimposed to the T_g in the first heating ramp, disappears during the second heating trace. As the molecular stress is removed, the discontinuity of heat capacity is only attributed to the T_g. Indeed, in the second heating trace, the endothermic phenomena related to the structural relaxation disappear as the effect of the removing of the previous thermal history of the sample. Since the low conformation energy, the T_g values are higher in the second heating run. Determined at the midpoint of the heat capacity, the glass transition temperatures ranging from 70 to 77 °C are not significantly affected by carbon fillers and their different loadings in UV-LED cured samples.

However, the addition of nanoparticles in polymer matrix involves the changing of the bulk properties. In particular, the T_g values, connected to the mobility of the polymeric chains, is affected by the interaction of polymer matrix with the nanoparticle surface in the interphase region. The interphase region is influenced by the filler size: while the micrometric Biochar particles form a small interphase region between filler and polymeric matrix, the interphase of MWCNTs has a crucial importance due to the high surface to volume ratio of the nanoparticles. Moreover, in thin films, the change of T_g is connected to the confinement effect that, linked to the small inter-particles distance, is independent on the gyration radius of the polymer chains. However, the concept of the cooperatively rearranging regions can be assumed to describe a thin film system densely packed in which the center-mass of chain polymer involves also the motion of the close segments. For this reason, the interaction between polymer-filler surface affect also the dynamics in the closest polymer segments up to hundred nanometers in the polymer film [192].

According to *Putz et al.*, two models can explain the alteration of the T_g of thermosetting nanocomposites. The increasing of the T_g, in a low cross-linked network, is attributed to the restricted mobility of the polymeric chains as consequence of the interaction between the nanoparticles and the thermosetting matrix. As the density system increases, the T_g of the thermosetting matrix decreases or remains unchanged. This effect can be attributed to the disruption of the crosslinking network, since the steric limitation reduces the number of functional groups that could able to react. In addition to the steric limitation, the changes in T_g depend on the interphase region: the decrease of T_g depends on the repulsive interfacial interaction, its increase is related to the attractive interactions that slow down the dynamics in the polymeric system.

Since a maximum T_g change of 2°C was detected in the system containing the mixture of Biochar/MWCNTs, probably a weak interphase results from the attractive π stacking interaction between the aromatic groups of the EB150 and the surface of the MWCNTs and Biochar. On the other hand, the increasing of crosslinking density of the systems containing MWCNTs and Biochar is responsible of the unchanged T_g values of the thermosetting matrix. The increasing of the crosslinking density leads to the decrease of the interfacial interactions and the interphase region that has a negligible effect on the T_g values.

In particular, in high crosslinked networks, the change of the physical and thermal properties by the introduction of nanoparticles impacts on the formation of the percolated interphase as well as on the thermal conductivity of the system [192].

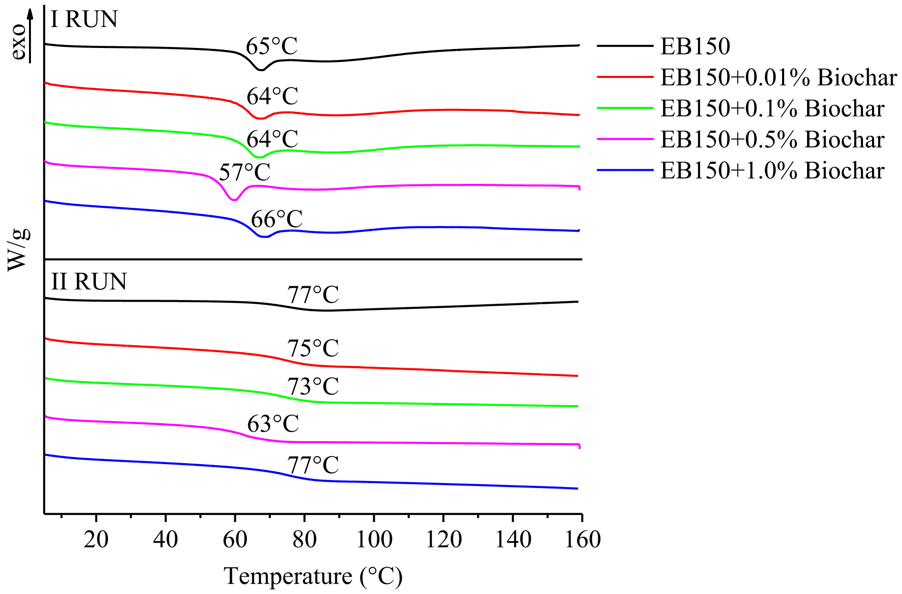

Figure 5.1. Differential scanning calorimetry (DSC) traces (1st and 2nd heating up) for UV-LED cured EB150 and its composites with different Biochar loadings.

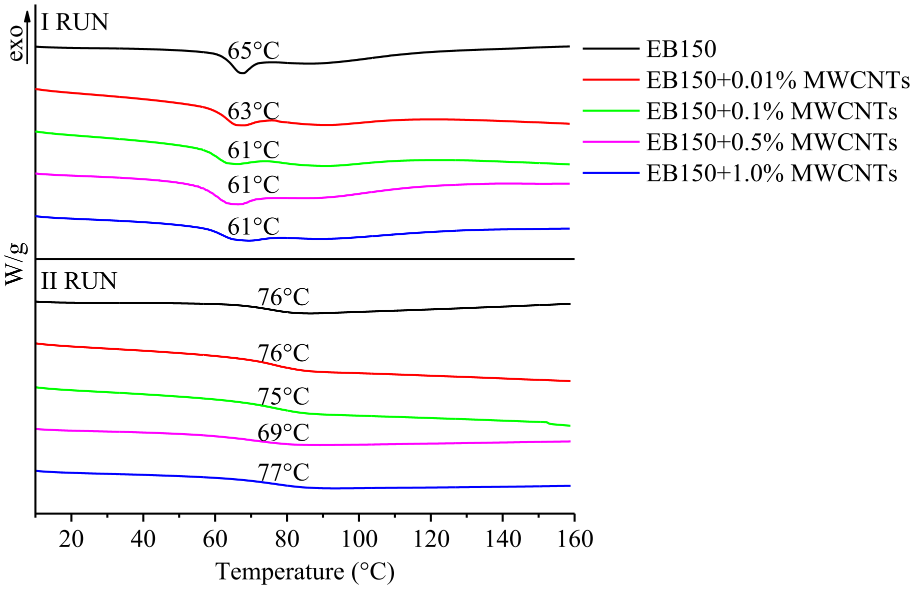

Figure 5.2. Differential scanning calorimetry (DSC) traces (1st and 2nd heating up) for UV-LED cured EB150 and its composites with different MWCNTs loadings.

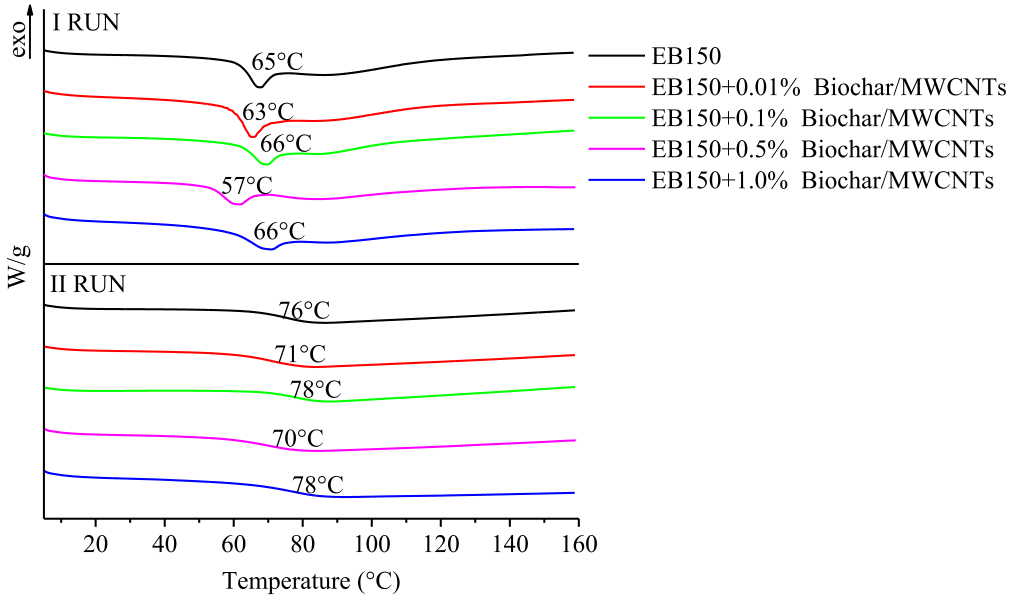

Figure 5.3. Differential scanning calorimetry (DSC) traces (1st and 2nd heating up) for UV-LED cured EB150 and its composites with different Biochar/MWCNTs loadings.

5.2 Thermo-gravimetric analyses (TGA)

The thermal stability of the UV-LED cured samples was evaluated using thermo-gravimetric analysis (TGA) as described in paragraph 3.1.2, according to the method explained in 3.9.5. TGA, performed in inert or oxidative atmosphere, aims at investigating the effect of the Biochar, MWCNTs and the mixture of Biochar/MWCNTs on the thermal degradation behaviour of the acrylic thermosetting matrix. The TGA results are represented in two different graphs where the percentage weight loss (%) and its first derivative (%/°C), respectively named TG and DTG curve, are plotted as a function of the temperature (°C).

The TGA and DTG curves of the EB150 film and its composites under nitrogen atmosphere are similar to that of sample containing 0.5% of Biochar, reported as example in figure 5.4 (a-b). Since in the thermo-gravimetric plot a constant slope characterizes each thermal decomposition step, in nitrogen atmosphere the degradation process occurs in a single step as shown in figure 5.4 (a). However, the degradation steps that occur in overlapped temperature range or that are attributed to the poor mass loss, are hardly to detect. On the other hand, DTG curve, shown in figure 5.4 (b), allows determining the transformation steps displayed as a peak corresponding to the maximum weight loss rate ($T_{max\%}$). As depicted in figure 5.4 (b), the $T_{max\%}$ of the sample EB150+0.5% Biochar occurs at 445°C.

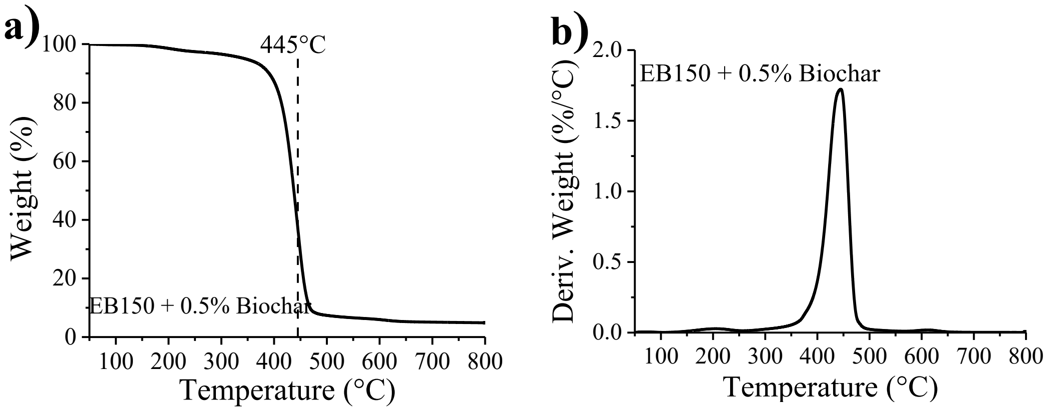

Figure 5.4. Thermal degradation curve (a) and derivative thermal degradation curve (b) of EB150+0.5% Biochar obtained with TGA test under nitrogen atmosphere.

In order to evaluate the effect of the filler content on the thermal stability of the polymeric matrix, the TG and DTG profiles of the neat cured resin and the Biochar-based composite coatings at different filler content are compared in figure 5.5 (a-b). All the samples show a single degradation step and weight loss with temperature higher than 90%. The degradation behaviour of the loaded thermosetting resin suggests that the Biochar content negligibly affects the thermal stability of the host polymer matrix as derived from the overlapping of curves and the almost constant residue (about 5%) of the composite coatings. The slight increasing levels of char at 700°C, reported in table 5.1, are probably attributed to the filler content: since the Biochar is not able to interact chemically with the thermosetting resin, it does not impact the mass loss process of the host polymer matrix.

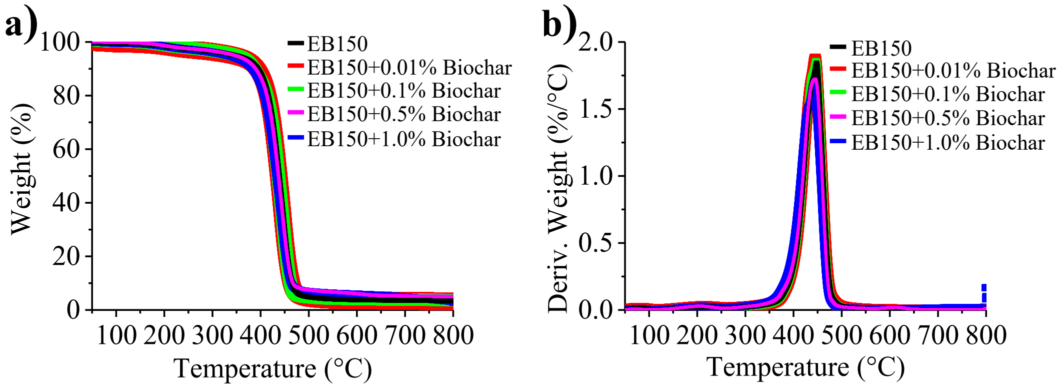

Figure 5.5. Thermal degradation curve (a) and derivative thermal degradation curve (b) of EB150 and its composites at different loading of Biochar obtained with TGA test under nitrogen atmosphere.

The effect of the filler type on the thermal stability of the thermosetting resin is depicted in figure 5.6 (a-b) representing the TG and DTG curves of the neat cured resin and the composite coating films. In figure 5.6 the selected composites, differ each other for the filler type (Biochar, MWCNTs and Biochar/MWCNTs) incorporated in the polymer matrix at 0.5 wt.%. As observed previously for the Biochar based composite coatings, the samples show a single degradation step, during which a significant mass loss (higher than 90%) occurs. As it is emerged, the filler type does not affect the degradation process of the hosting polymer: Biochar and MWCNTs, both as single and mixed fillers, do not interact chemically with the polymer matrix but act as inert additives within the selected temperature range.

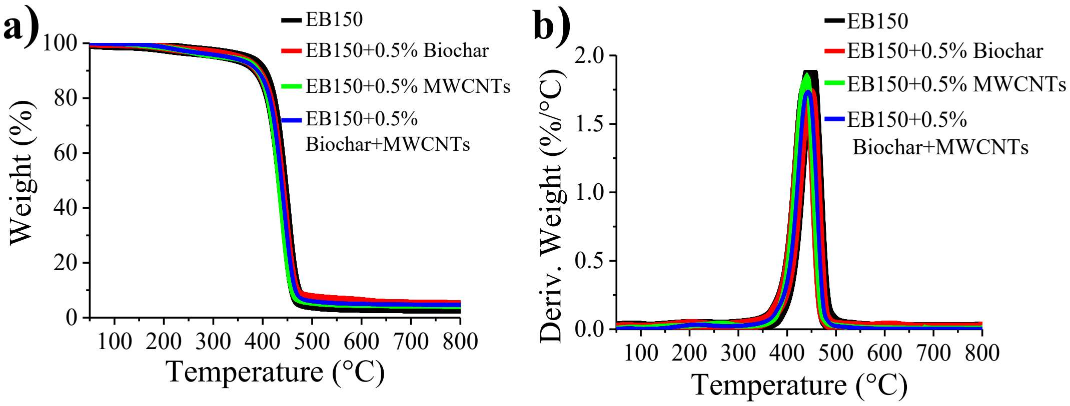

Figure 5.6. Thermal degradation curve (a) and derivative thermal degradation curve (b) of EB150 and its composites containing 0.5% Biochar, 0.5% MWCNTs and 0.5% Biochar/MWCNTs obtained with TGA test under nitrogen atmosphere.

The degradation behaviour of the composite coatings containing different loadings of Biochar, MWCNTs and Biochar/MWCNTs were studied in detail to evaluate $T_{max\%}$. This value is compared with the $T_{max\%}$ of neat EB150 and its composite films in table 5.1. In addition to $T_{max\%}$, in table 5.1, $T_{10\%}$ and $T_{50\%}$, i.e. the temperatures, at which 10% and 50% weight loss occur respectively, are reported for each sample. The comparison between the composite samples with different loadings of Biochar, MWCNTs and Biochar/MWCNTs confirms that both filler type and its loading do not affect significantly the thermal degradation behaviour of EB150, since the values of $T_{10\%}$, $T_{50\%}$ and $T_{max\%}$, located respectively at about 390, 430 and 440°C, are close to that of unfilled EB150.

The data collected in table 5.1 also report the residue (wt.%) at T_{max} and at 700°C. Although the degradation behaviour of the composite films is unchanged with respect to that of EB150, the residues at T_{max} and 700°C increase by about 3 and 1% as compared with the unfilled resin, according to the higher filler content.

Table 5.1. Thermal stability of the UV-LED EB150 film and its composites in nitrogen atmosphere (experimental error: ±0.5 wt.%, ±1°C).

			Atmosphere: N_2			
Filler	**Filler Loading (wt.%)**	**$T_{10\%}$ (°C)**	**$T_{50\%}$ (°C)**	**$T_{max\%}$ (°C)**	**Residue @T_{max} (wt.%)**	**Residue 700°C (wt.%)**
-	0.00	395	439	448	34.6	3.6
Biochar	0.01	393	438	445	36.5	3.4
	0.1	393	438	447	34.1	3.2
	0.5	391	437	445	37.4	5.1
	1.0	383	432	441	36.2	4.8
MWCNTs	0.01	393	439	447	35.5	3.6
	0.1	394	440	449	33.7	3.7
	0.5	392	434	441	37.5	4.1
	1.0	395	438	444	39.0	5.0
Biochar/MWCNTs	0.01	394	439	448	34.4	3.6
	0.1	391	437	445	36.7	3.5
	0.5	390	438	443	40.3	4.8
	1.0	388	434	440	38.9	4.7

The thermo-oxidative degradation process is displayed in figure 5.7, where the TGA (a) and DTG (b) curves of EB150+0.5% Biochar are shown as an example. As the sample containing 0.5% of Biochar revealed, the degradation steps of the unfilled EB150 and its composite films, under oxidative atmosphere, occurs according to three steps. The degradation steps are associated with the stretches of TGA curve at constant slope and the peaks corresponding to the T_{max} on the DTG curve. Due to the correspondence with the T_{max}, the three degradation steps are detected on the DTG curve and occur at $T_{1max\%}$, $T_{2max\%}$ and $T_{3max\%}$ temperatures that are collected in table 5.2 for each sample.

The thermo-oxidative degradation process of the thermosetting composite coatings involves the formation of carbonaceous products obtained from the dehydration of the backbone polymer network. The carbonaceous materials, consisting of polyaromatic species, are characterized by a layered structure that could be responsible for the heat resistance of the thermosetting material. The formation of carbonaceous material is characterized by the surface oxidation of the sample with the generation of cracks and the oxidative breakdown of the cured thermosetting network. At higher temperatures, the complete degradation of the carbonaceous material and the formation of char residue occur as the result of the thermo-oxidative reactions. In particular, during the dehydrogenation process, the C/O ratio decreases due to the dealkylation of hydrocarbons with the release of volatiles and the formation of polyaromatic species. These steps correspond to the maximum weight loss rate at about 400 and 500°C respectively, as observed in figure 5.7 (a-b). Moreover, at higher temperature (>450°C) the oxides, formed on the coating surface, are probably responsible for the improved thermo-oxidative stability of the samples as they act as heat barrier and oxygen insulator.

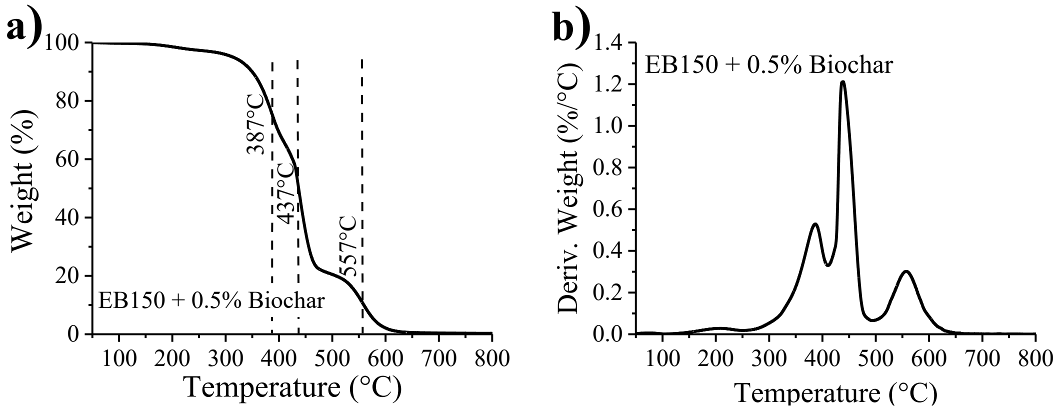

Figure 5.7. Thermal degradation curve (a) and derivative thermal degradation curve (b) of EB150+0.5% Biochar obtained with TGA test under air atmosphere.

In detail, the first degradation step occurs at about 375°C and can be attributed to the decomposition of the low molecular weight structure such as dimers and trimers. The second step was found at about 440°C and involves the main degradation of the polymer network. The third degradation step takes place at higher temperatures (at about 560°C) as a consequence of a further oxidation of the previous degradation products with the consequent formation of CO and CO_2. The three degradation steps are not significantly affected by the filler type and its loading, since they occur at temperatures close to those of EB150.

The comparison between the thermo-oxidative degradation curves of the composite films at different Biochar loadings allows assessing the influence of the filler content on the thermal stability of the neat cured resin. In figure 5.8 (a-b), the TG and DTG profiles suggest that the thermo-oxidative process of the composite coatings retraces the behaviour of the neat resin characterized by three main degradation steps in correspondence of the changes in curve slopes. The appreciable overlapping of the curves in figure 5.8 reveals a negligible influence of the Biochar on the thermo-oxidative stability of cured network as the almost constant residues at 700°C, reported in table 5.2 demonstrate, despite a slight increase of the char yield observed at 1.0 wt.% of Biochar loading, as compared to the neat resin.

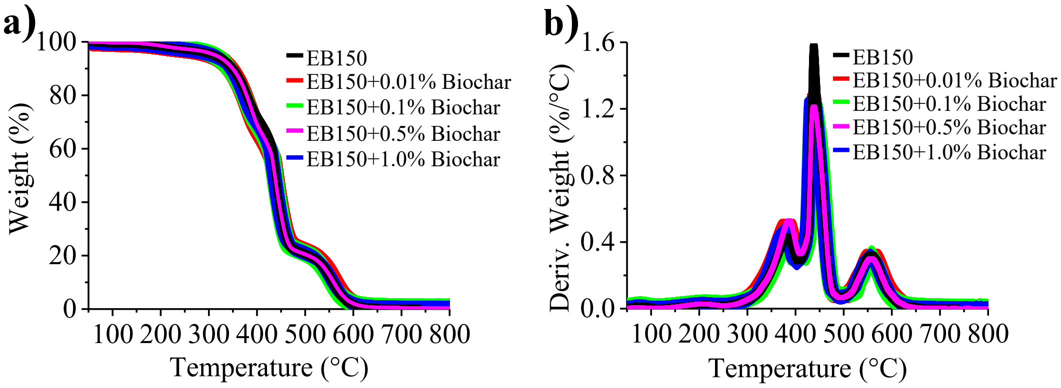

Figure 5.8. Thermal degradation curve (a) and derivative thermal degradation curve (b) of EB150 and its composites at different loading of Biochar obtained with TGA test under oxidative atmosphere.

The influence of the filler type on the thermo-oxidative degradation behaviour of thermosetting matrix is depicted in figure 5.9 (a-b), where the TG and DTG curves of the samples differing each other for the filler type are shown: in particular, the composite films containing Biochar, MWCNTs and Biochar/MWCNTs, at the same loading, are compared with the unfilled resin. Similar to the Biochar-based composite coatings, the samples in figure 5.9 show the same degradation behaviour of the neat resin characterized by three steps. The overlapped TG and DTG curves indicate that Biochar and MWCNTs, both as single and mixed fillers, are not effective to improve the thermo-oxidative stability of the polymer network. However, a slight improving in thermal stability is observed for the sample containing MWCNTs that may be responsible of the higher char yield at 700°C in comparison with the samples containing Biochar and Biochar/MWCNTs, having the same filler loading.

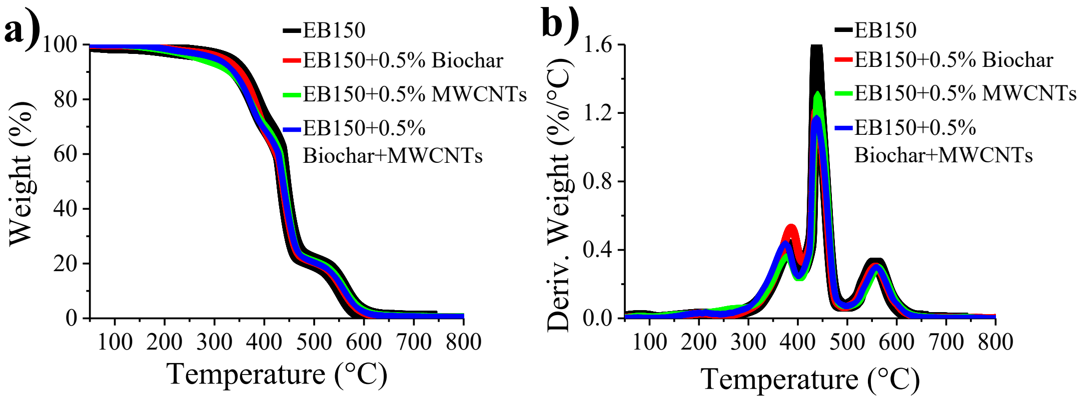

Figure 5.9. Thermal degradation curve (a) and derivative thermal degradation curve (b) of EB150 and its composites at 0.5% Biochar, 0.5% MWCNTs and 0.5% Biochar/MWCNTs obtained with TGA test under oxidative atmosphere.

Table 5.2 summarizes the temperatures where 10% ($T_{10\%}$) and 50% ($T_{50\%}$) of mass is loss, both extrapolated from the TGA curves. Such data indicate that the degradation behaviour of the composite films results almost unchanged with respect to the unfilled resin. In fact, the presence of the filler does not enhance the thermal stability of the thermosetting resin since the temperatures corresponding to 10 and 50% of weight loss, respectively at 340 and 440°C, are close to those of EB150. As observed in nitrogen atmosphere for the composites with the highest filler content, the residue at 700°C increases by about 0.4%.

In conclusion, the TGA confirms the previous DSC evaluation: since the presence of the filler in thermosetting matrix does not hinder the molecular mobility of the polymer chains, the thermal stability of the composite films is not impacted.

Table 5.2. Thermo-oxidative stability of the UV-LED EB150 film and its composites in air atmosphere (experimental error: ±0.5 wt.%, ±1°C).

		Atmosphere: Air					
Filler	**Filler Loading (wt.%)**	**$T_{10\%}$ (°C)**	**$T_{50\%}$ (°C)**	**$T_{1max\%}$ (°C)**	**$T_{2max\%}$ (°C)**	**$T_{3max\%}$ (°C)**	**Residue 700°C (wt.%)**
-	0.00	349	439	382	438	557	0.3
Biochar	0.01	346	440	382	437	559	0.3
	0.1	342	438	380	438	557	0.4
	0.5	350	437	387	437	557	0.4
	1.0	340	439	373	439	557	0.7
MWCNTs	0.01	341	437	382	436	556	0.2
	0.1	342	440	383	439	559	0.3
	0.5	331	441	378	440	565	0.8
	1.0	335	434	379	438	558	0.8
Biochar/MWCNTs	0.01	346	440	382	437	559	0.3
	0.1	342	438	380	438	557	0.4
	0.5	339	437	377	438	559	0.6
	1.0	340	439	373	439	557	0.7

5.3 Dynamic mechanical thermal analyses (DMTA)

Dynamic mechanical thermal analysis (DMTA) allows investigating the viscoelastic behaviour of the UV-LED cured EB150 and its composite films. DMTA measures the deformation of UV-LED cured films subjected to an oscillating force in order to detect the effect of the fillers and their loadings on the viscoelastic properties of the acrylic thermosetting matrix as described in chapter 3. The deformation of the material is expressed in terms of storage modulus (E'), loss modulus (E'') and loss factor (tanδ) corresponding to the ratio between the loss and storage moduli (E''/E'). Besides, E' corresponds to the mechanical energy that is stored by the material under load, E'' provides the energy that, during the deformation test, is converted to heat; tanδ represents the comparison between the dissipated and storage energy amount. E' and E'' are evaluated as a function of the temperature as reported in figure 5.10 (a) where, as an example, the viscous-elastic behaviour of the sample containing 0.1 wt.% of Biochar is shown. In figure 5.10 (b), tanδ is plotted as a function of the temperature. The graph allows determining in correspondence of the curve maximum, the glass transition temperature (T_g), above which the motion of polymeric chain occurs.

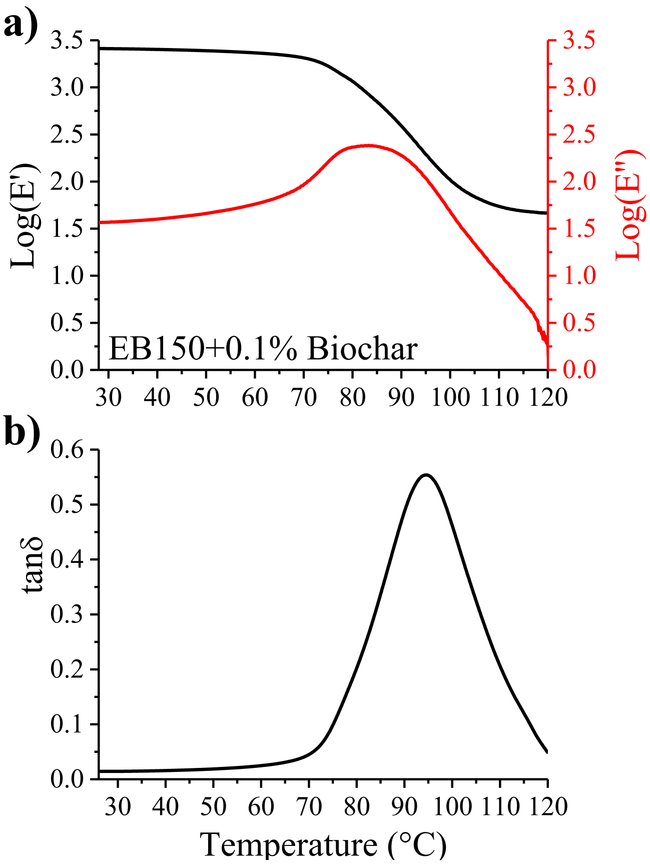

Figure 5.10. Log scale of storage modulus and loss modulus as a function of the temperature (a) and tanδ as a function of the temperature (b) of EB150+0.1% Biochar.

The graph in Figure 5.10 (a) shows the solid-state transition: the molecules, from a compressed state at lower temperatures, gain enough free volume at higher temperatures, at which the motion of the atoms, both in the backbone chain and in the side chains is promoted. With increasing temperature, E′ modulus decreases slightly, until the T_g region is reached, where large-scale motion is favoured. Since the change in physical properties occurs during the transition from glassy to rubbery state, T_g represents the main feature of the polymeric material. Known also as α transition, T_g corresponds to the E′ drop onset in figure 5.10 (a) and the peak of the tanδ curve in figure 5.10 (b). However, the T_g values from the two modes differ of about 25°C considering the same test run.

Above the T_g region, E′ modulus drops up to the rubbery plateau, whose length is dependent on the molecular weight between the crosslinks. As the heating continues, the UV-LED cured film begins to degrade since the crosslinks in polymer network hinder the slipping and the flowing between the chains.

Since the loading and type of filler may affect the viscoelastic properties of the thermosetting matrix, the E′ and tanδ values of the composite films are compared with the neat resin in figure 5.11 (a-d). The fillers could act as crosslinking sites that may hinder the segmental motion of the polymer chains impacting the viscoelastic properties of the matrix.

In particular, figure 5.11 (a-b) shows the influence of the Biochar loading on the storage and tanδ of the thermosetting matrix. Compared to the neat resin, a negligible improvement of E′ in glassy region of the composite coatings is observed in figure 5.11 (a), proving that the Biochar loadings do not affect significantly the stiffness of the thermosetting matrix. The tanδ curves in figure 5.11 (b) indicate that the samples have similar profiles: both the Biochar based composite coatings and the neat resin show a narrow peak in correspondence of the transition region, above which tanδ collapses as the rubbery region is reached. Moreover, the almost constant peak values with the increase of the Biochar content indicate that the composite samples, irrespective of the filler loading, are characterized by the same degree of the molecular mobility of the polymer chains in comparison with the neat resin.

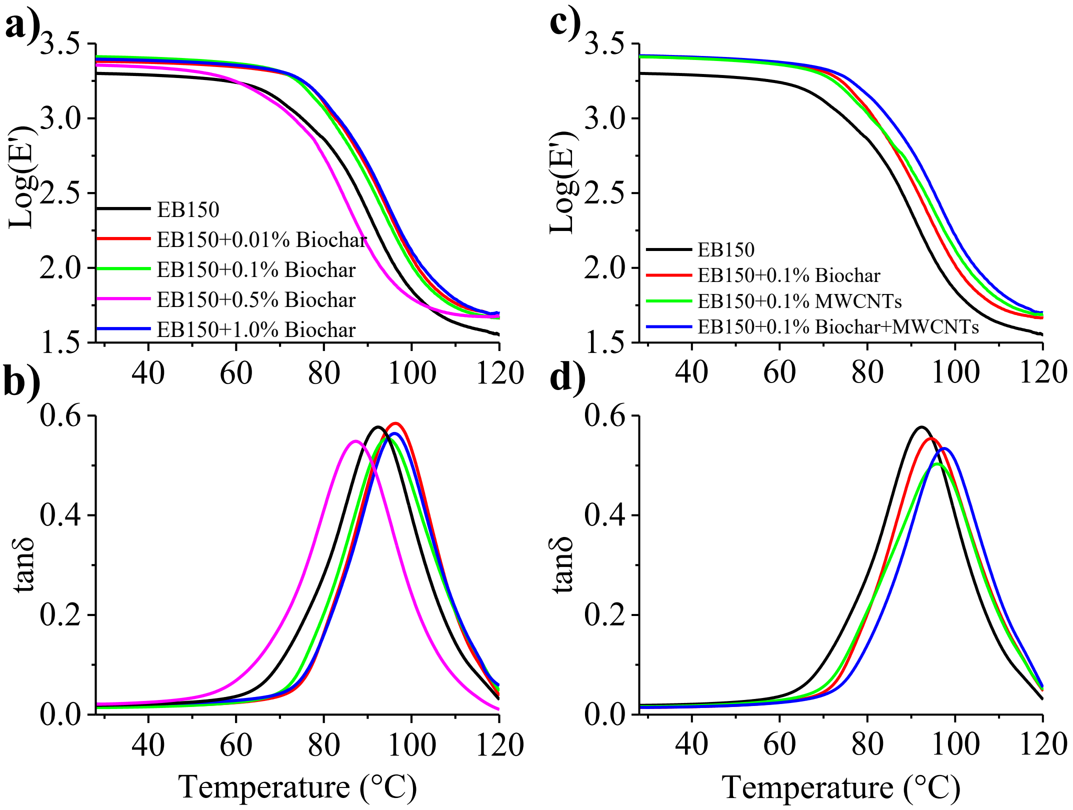

Figure 5.11. Log scale of storage modulus and tanδ as a function of the temperature of EB150 and its composites at different Biochar loadings (a-b) on the left, Log scale of storage modulus and tanδ as a function of the temperature of EB150 and its composites at 0.1% Biochar, 0.1% MWCNTs and 0.1% Biochar/MWCNTs (c-d) on the right.

The effect of the filler type on the viscoelastic properties of the polymeric matrix is shown in figure 5.11 (c-d): E′ and tanδ curves of the neat resin are compared with the composite films that differ each other as far as the filler type (Biochar, MWCNTs and Biochar/MWCNTs) is considered. In particular, figure 5.11 (c-d) shows the profiles of the composite films at the same filler loading (i.e. 0.1 wt.%) in order to better appreciate the comparison between the types of additives. The overlapping of the E′ curves of the composite film suggests that the different types of filler do not affect the storage modulus of the neat resin.

As it is emerged, the viscoelastic properties of the sample at 0.1 wt.% of Biochar are comparable with the samples that, whit the same filler loading, contain the MWCNTs and Biochar/MWCNTs. The analogous E′ trends of the studied composite systems indicate that Biochar and MWCNTs, both as single fillers and mixed together, are not sufficiently effective to impart a significant improvement of the stiffness in the glassy state of the composite coatings. The introduction of filler, irrespective of the types, does not provide the reinforcement of the polymeric chains since both the Biochar and MWCNTs are not able to chemically interact with the polymer crosslinking network as the almost constant E′ values in figure 5.11 (c) demonstrate.

The T_g values in figure 5.11 (d) prove that the introduction of the fillers, irrespective of the type, marginally affect the crosslinking density and the molecular motion of the polymer network. The tanδ curves are characterized by a single narrow peak, however a slight increase of the T_g values of the composite films is indicative of the higher crosslinking density with respect to the neat resin. In order to investigate the effect of the fillers on the acrylic resin before and after the T_g region, the values of E′ modulus at 30°C in the glassy region and 100°C in the rubbery region, were determined. The E′ values of UV-LED cured composite films, collected in table 5.3, are close to that of the EB150 since they are not significant affected by the presence of the filler both at 30 and 100°C. A slight decrease of E′ is detected for the samples that contain MWCNTs and Biochar/MWCNTs at the highest loading. The negligible variation of the E′ modulus has a considerable relevance in the curing process, since the addition of MWCNTs and Biochar particles does not affect the curing behaviour of the acrylic resin.

Table 5.3. Logarithm of E′ at 30 and 100°C and Tg (°C) obtained from the maximum peak of the tanδ for the UV-LED cured EB150 and its composites

Filler	**Filler Loading (wt.%)**	**LogE'(Pa) @ 30°C**	**LogE'(Pa) @ 100°C**	**Tg (°C)**
-	0.00	3.41	2.01	92
Biochar	0.01	3.38	2.07	96
	0.1	3.41	2.02	95
	0.5	3.35	2.08	95
	1.0	3.39	2.11	96
MWCNTs	0.01	3.42	2.09	95
	0.1	3.41	2.12	96
	0.5	3.26	1.89	95
	1.0	2.57	1.47	98
Biochar/MWCNTs	0.01	3.41	2.01	94
	0.1	3.41	2.21	98
	0.5	3.27	2.08	97
	1.0	3.03	1.90	98

Despite the reinforcing effect appears in well dispersed composite system, this requirement is not self-evident. On one hand, the cluster nature of the MWCNTs compromises the mechanical performance of the polymeric composites due to the reduced particle aspect ratio. On the other hand, the sonication process used to increase the interfacial region MWCNTs/matrix, may alter the particles and their aspect ratio. Besides, the presence of inherent aggregates in polymer matrix could act as stress concentrators and provide some crack in the matrix. As the effect of simultaneously event, the improved mechanical properties of the nanocomposites are not realised. A similar behaviour was found also by *Starkova et al.*, who studied a thermosetting epoxy system, to which MWCNTs were added at different loadings from 0.1 to 1.0 wt.%; the influence was negligible on both E′ modulus and T_g values [193].

However, the negligible E′ modulus in the system containing Biochar is probably ascribed to the lower content of the Biochar with respect to the analogous system studied by *Matykiewicz*. The author noticed an improving of E′ modulus as the content of the Biochar in epoxy resin ranged from 2.5 to 10 wt.% with respect to the unfilled system without reducing its T_g, similar for all system studied [194].
Table 5.3 collects, in addition to the E′ modulus, the T_g values determined in correspondence of the maximum peak of tanδ, for each sample. It is noteworthy a difference between the T_g values obtained from DSC and those one found with DMTA, lower of about 20°C. This discrepancy is ascribed to the different operating principles that the two techniques are based on. The T_g values, indeed, are strictly dependent on the operating conditions according to the analytical methodology: in DMTA, the T_g is connected to the applied stress, heating rate and frequency and in DSC to the heating or cooling rate. However, while the T_g values from DSC of UV-LED composite films remain almost unchanged respect to the neat resin, T_g from DMTA slightly increase of few grades (4-6°C) with respect to the unfilled resin (92°C), regardless of the filler loadings. These results are consistent with those reported in literature that suggest a slight increase or almost unchanged T_g values of cured composites containing MWCNTs in comparison with the unfilled sample [195-197]. On the other hand, the incorporation of MWCNTs could provide to the decrease of the T_g values respect to the cured neat resin [198,199]. The reason of the discrepancy between the results is probably ascribed to the effect of different parameters that, acting simultaneously, contribute to the final value of the T_g. The T_g is affected by the aspect ratio, the packing density and purity of the MWCNTs as well as the interaction of the filler particles with the polymer matrix. Because of the high aspect ratio of the MWCNTs particles, the extra free volume generated by the interface MWCNTs/matrix contributes to the large-scale motion of the chain molecules, leading to lower T_g values. As the content of MWCNTs increases, the aggregation of the MWCNTs is responsible for the lowering of the T_g as well: the increase of the interactions between MWCNTs rather than between filler and polymer matrix does not hinder the polymeric chain motion since no restrictions are imposed by the interaction with the nanoparticles. On the other hand, the physical hindrance of the MWCNTs is responsible for the increase of the T_g because of the reduced mobility of acrylic resin [200].
In addition to the filler/matrix interaction, also the operating parameters of the curing process affect the T_g values: a higher crosslinking density corresponds to higher T_g values [197].
Since the T_g values of composite films are higher or almost unchanged with respect to the unfilled system, from the above it appears that the fillers are well dispersed in the polymer matrix and they do not affect the curing process of the resin.

Chapter 6

Thermal conductive and optical properties of the UV-LED cured films

6.1 Thermal conductivity

The incorporation of carbon fillers into a thermosetting matrix is a possible method to improve the thermal conductivity of the insulating polymers [201]. The heat transfer, attributed to phonons, could be schematized by cooperative vibration modes among the adjacent atoms. On one hand, inside crystalline structures, the atoms are organized as long range ordered structures, such as the periodic lattice. Such structures are able to transfer efficiently the cooperative vibrations and thus the thermal energy. On the other hand, in the amorphous structure, characteristic of many polymeric materials, the cooperative vibrational modes are hindered: the random-distributed nature of the polymer chains and, thus, the lack of long rage ordered structure are responsible for the poor thermal conductivity of polymers. In a polymeric composite, the heat transfer is favoured by the formation of a continuous network between the fillers [202]. Such network is formed at a critical filler loading, known as percolation threshold, above which the heat conduction pathway in the polymer matrix is promoted by the contact between the adjacent particles [202].

Since the ordered crystalline structure of the carbon filler is correlated to its graphitization grade, both Biochar and MWCNTs are suitable candidates to enhance the thermal conductivity of the insulating acrylic thermosetting matrix, which they are dispersed in. In particular, the phonon transport occurs through the graphitic structure, where both the free length path and the number of vibrational modes are higher with respect to the amorphous polymer.

Adopting the Transient Plane Source technique described in paragraph 3.5 and the operating conditions illustrated in the section 3.9.7, the thermal conductivity of the UV-LED cured composite films was investigated. The thermal conductivity of unfilled EB150 (about 0.11 W/mK, figure 6.1) is compared with its composites at different loading of the Biochar (a), MWCNTs (b) and the mixture of Biochar/MWCNTs (c).

Despite the incorporation of the carbonaceous fillers, the thermal conductivity of the carbon-based composites is not always predictable. In fact, multiple factors including filler type, size and shape as well as its interaction with polymer matrix may influence the thermal conductivity of the polymer composites.

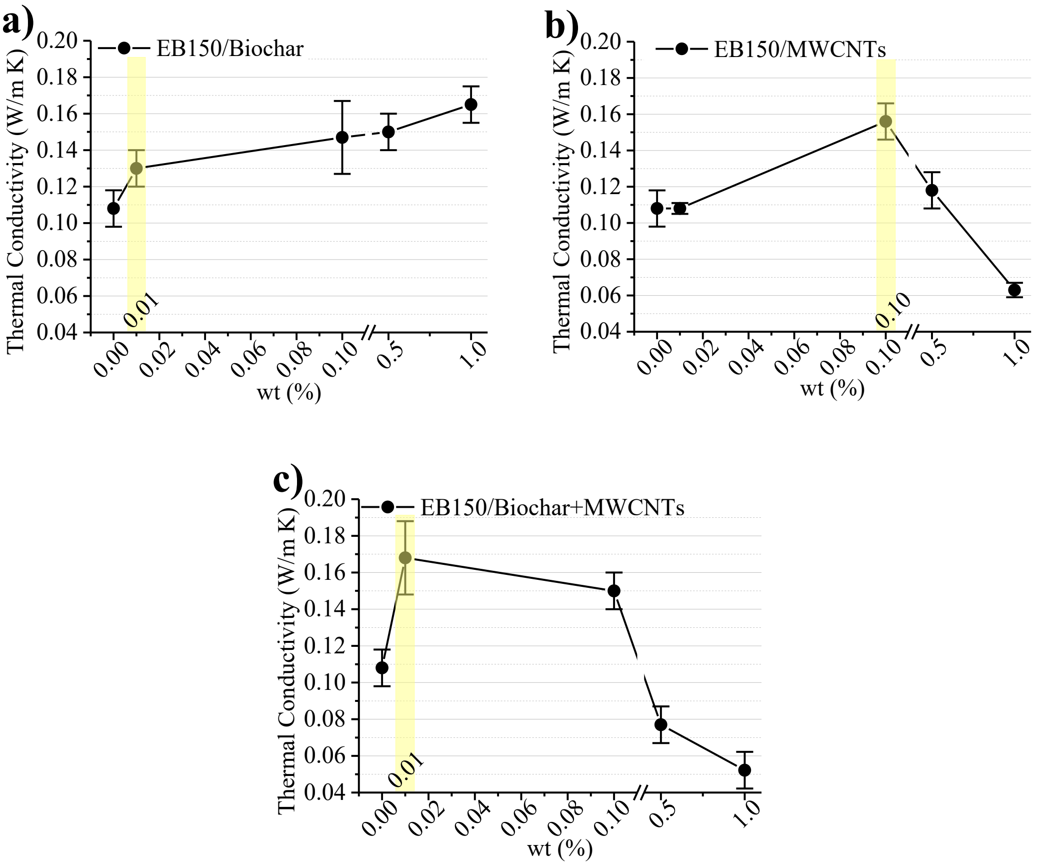

Figure 6.1. Thermal conductivity of the UV-LED cured EB150 and its composite films as a function of filler loading: (a) with Biochar, (b) with MWCNTs, (c) with Biochar/MWCNTs. Different trend can be observed according to the filler type and loading.

The Biochar and MWCNTs, both individually and in hybrid systems, differently affect the thermal conductivity of the thermosetting matrix as shown in figure 6.1 (a-c).

Despite the slight variation of thermal conductivity with respect to unfilled EB150, it is worthy to note the effect of the size and shape of the two fillers on the formation of the conductive pathway [201,202]. First of all, the comparison between the Biochar and MWCNTs systems reveals that the percolation threshold is reached at the lowest filler loading (namely at 0.01 wt.% for Biochar and at 0.1

wt.% for MWCNTs). Above the percolation threshold, the thermal conductivity increases with the Biochar content whereas decreases below unfilled EB150 as the MWCNTs loading increases. The two different trends are probably ascribed to the filler-matrix interaction connected to the micrometric and nanometric particle sizes of the Biochar and MWCNTs, respectively. From micro to nano sized particles, the interface area between filler and polymer matrix increases and the interfacial boundary scattering may overcome the phonon transport. Besides, the reduced interfacial resistance in the micro-composites is probably responsible for the formation of a conductive network at lower Biochar content with respect to the MWCNTs counterpart. On one hand, as Biochar content increases, the interconnection between the filler particles may prevail over the interfacial interaction, providing the enhancing of the thermal transport. On the other hand, MWCNTs based composites show an apparent decrease of thermal conductivity above the percolation threshold. The discrepancy between the two systems could be explained in terms of filler dispersion in polymeric matrix: while the Biochar particles are homogeneously dispersed also at highest filler loading, the MWCNTs form micrometric isolated bundles, as FESEM analysis revealed. The influence of the dispersion state on the thermal conductivity arouses controversial opinions in literature since the experimental tests provide, in some cases, opposite results [201]. However, according to *Burger et al.*, in a poor dispersed system, the large distance among the isolated agglomerates, at a relatively low loading, is more detrimental with respect to the interfacial interaction filler-polymer matrix in a system better dispersed [201]. This hypothesis is in agreement with *Safdari et al.* that studied CNTs based epoxy composites, for which the thermal conductivity reaches a plateau at 1.0 wt.% of filler loading and then decreases. The authors attributed this behavior to the formation of CNTs agglomerates that may hinder the improvement of the thermal conductivity. Furthermore, they explained that the flexibility of the CNTs induces the nanoparticles bending during the mixing process, hence reducing their length and the effective aspect ratio. As the length of CNTs decreases, the filler/matrix interfaces increase, as well as the thermal resistance [185]. In addition, the decreased thermal conductivity can be attributed to the structure of the MWCNTs. In fact, the nanowire type particles show an improved interface-scattering efficiency due to the higher cross-plane interface ratio in comparison with other nanoparticles [203]. In addition to the interfacial properties, the decrease of the thermal conductivity of the MWCNTs based composites can be ascribed to the air trapped in the micropores of the composite film. During the TPS analysis, the heat is transferred within the film from the MWCNTs to the air that possesses a low thermal conductivity (0.026 W/mK), hence providing, in addition to the convection mechanism, the decrease of the local temperature as well as the rise of heat transfer resistance [204].

When Biochar and MWCNTs are combined, the thermal conductivity as a function of the filler loading follows the trend shown in figure 6.1 (c). The hybrid system displays an intermediate behavior with respect to the composites with Biochar and MWCNTs as individual fillers. The hybrid composite is similar to the Biochar system at lower filler loading as the percolation threshold is reached at

0.01 wt.%. Since the thermal conductivity reaches a plateau at the percolation threshold, the hybrid system behavior at the higher filler loading is close to that of MWCNTs: the thermal conductivity decreases below the neat EB150 as filler content increases. However, the thermal conductivity at 0.01 wt.% of the mixed fillers is the highest (about 0.17 W/mK) also in comparison with the previously analyzed systems, regardless of the filler loadings. As reported in literature, the hybrid systems show an enhanced thermal conductivity when compared to the individual counterpart because the mixed fillers are able to build a thermally conductive network that reduces the interfacial resistance between filler and polymer matrix [141, 185, 204, 205]. Thanks to the improvement of contact between particle surface, both the thermal resistance and the system viscosity decrease: the mixed fillers provide a more efficient percolating hybrid composite network and maximize the packing density [141, 204]. In the Biochar/MWCNTs composites, the highest thermal conductivity at the lowest filler content could be promoted by conductive bridge through the π-π stacking of the Biochar and MWCNTs graphitic structure. However, above the percolation threshold, the thermal behavior is close to the MWCNTs based composite at the highest filler loadings, as the nanoparticles aggregation and the interfacial thermal resistance increase, as well as the system viscosity. *Im et al.* attributed the increase of the thermal resistance of a graphene oxide-carbon nanotube hybrid epoxy composites system to the agglomeration or bending of the MWCNTs. As the MWCNTs loading increased, the interfacial resistance increased as well as the phonon scattering density, due to the lack of an interconnected structure with the graphene oxide [203].

6.2 Electrical conductivity

The electrical conductivity of polymer composites, analogously to the previously discussed thermal conductivity, actually occurs by the generation of a three-dimensional percolation network containing conductive fillers. The minimum filler concentration, known as percolation threshold, is necessary to impart conductive properties to the polymeric matrix. Unlike the thermal conductivity based on the phonon transfer, the tunneling-percolation effect is used to explain the electrical behavior of carbon filler reinforced polymeric composites [60, 206]. The electrical conductivity, according to tunneling-percolation theory, is based on the electron hopping between close conductive particles, spanning in a polymer matrix. However, the electron tunneling does not require the tight contact between the filler particles as in the phonon conduction: indeed, an interparticle gap of some nanometers does not compromise the electrical conductivity. This divergence justifies that the percolation threshold to achieve the electrical conductivity is lower than that necessary to ensure thermal conductivity [207].

In addition to thermal conductivity purposes, carbon fillers are also employed for improving the electrical conductivity of polymer matrix. As carbon rich materials, both Biochar and MWCNTs are able to generate an electron conductive pathway in the thermosetting matrix improving its electrical conductivity. The electrical conductivity of the carbon-based composite films was determined according to the two-probe method described in paragraph 3.9.8. The electrical conductivity, plotted in figure 6.2 as logarithmic resistance, is reported for each set of composite systems at different loading of Biochar (a), MWCNTs (b) and Biochar/MWCNTs (c). The electrical conductivity of the UV-LED composite films depends on the graphitic-like structure of the Biochar and MWCNTs, their loading, aspect ratio and interaction with the polymeric matrix. As expected, the percolation threshold is reached at the lowest filler loading independently from the filler type. According to the tunneling effect, the nanometric interparticle distance does not compromise the electrical transport between the close fillers. However, two different trends can be observed for Biochar and MWCNTs systems: above the percolation threshold, the electrical resistance of the Biochar based composite is almost constant as the filler content increases, whereas it lowers as the MWCNTs loading increases.

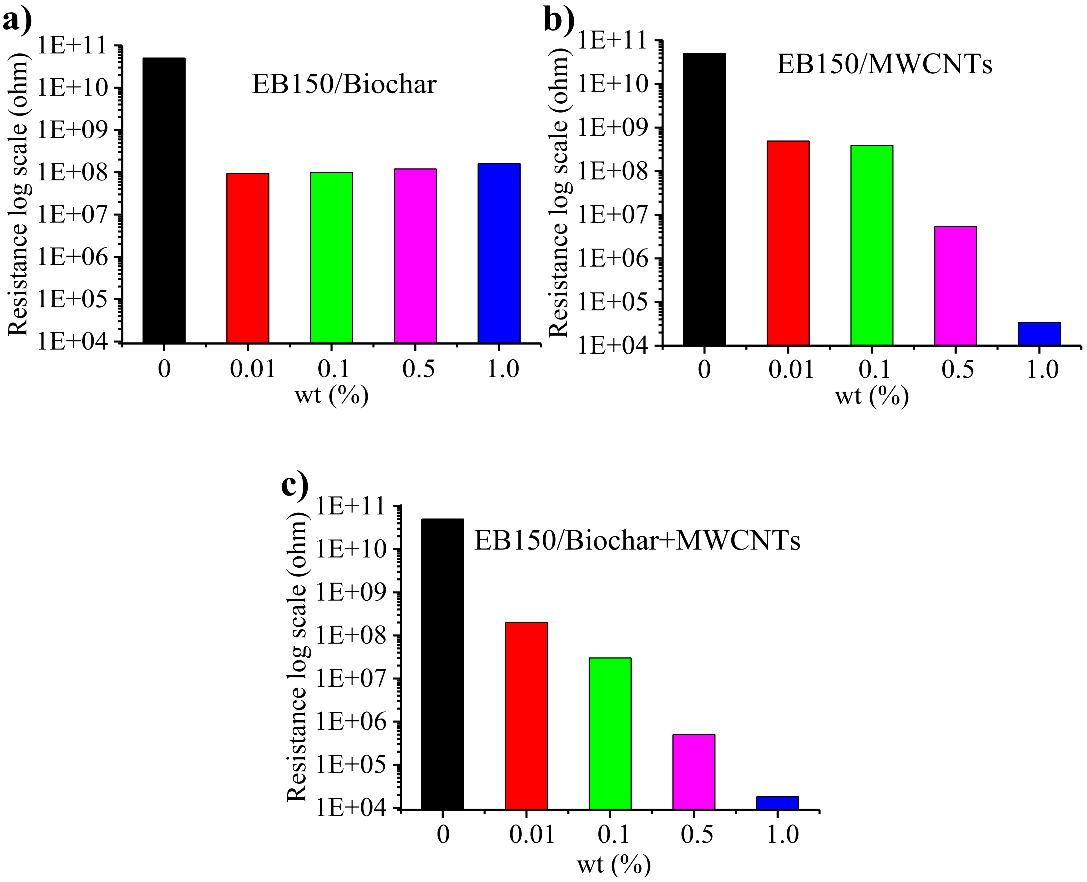

Figure 6.2. Electrical resistance in logarithmic scale of the UV-LED cured EB150 and its composites at different loading of Biochar (a), MWCNTs (b) and Biochar/MWCNTs (c). The hybrid system shows the lower electrical resistance respect to the Biochar and MWCNTs based composites.

In the system containing Biochar, the resistance of the composite decreases by two order of magnitude with respect to that of unfilled EB150, measured as about $5 \cdot 10^{10}$ Ω, irrespectively of the filler loading. These results are in agreement with those found by *Poulose et al.*, who determined the surface resistance of the polypropylene system containing 5, 10 and 15 wt.% of Biochar obtained by pyrolysis process of date palm waste at 700°C. The surface resistance values of the sample containing 5 wt.% of Biochar (2.0×10^{11} Ω/cm^2) decrease by about three order of magnitude with respect to the neat sample (2.0×10^{14} Ω/cm^2). As the Biochar content increases, the surface resistance decrease is not drastic: the surface resistivity decreases from 1.4×10^{11} Ω/cm^2 to 5.0×10^{10} Ω/cm^2, as Biochar content increases from 10 to 15 wt.%. The negligible resistance variation was attributed to the ash content that could reduce the formation of the continuous conductive network [208]. Besides, according to *Li et al.*, at 70 wt.% of Biochar, obtained through a carbonization process of bamboo wastes at 700°C, the electrical conductivity of polymeric composites increases by six order of magnitude respect to the neat UHMWPE [109].

Conversely to the Biochar system, the resistance of the MWCNTs based composites decreases as the filler content increases: the electrical resistance decreases from one to six order of magnitude as MWCNTs content increases. A similar trend was observed also by *Earp et al.* who determined a decreasing of the electrical resistance from one to three order of magnitude of the CNTs based epoxy composite as the filler increases from 0.014 to 2 wt.% [209]. In addition, the enhanced electrical conductivity of MWCNTs based composites also at low filler loadings are ascribed to the high aspect ratio of the nanoparticles as well as to their tendency to agglomerate [210]. It is worthy to note that the electrical conductivity, unlike the thermal one, is favored by the formation of the MWCNTs bundles, in which the interaction between carbon nanotube particles is promoted [211]. *Aguilar et al.* proved that, at low filler loading, in a film of 150-200 μm thickness, the agglomeration size is not large enough to allow the electrical conductivity through-thickness film. Moreover, the same authors found that the system with micrometric bundles showed, above the percolation threshold, enhanced electrical conductivity with respect to the film with MWCNTs uniformly dispersed. The improved electrical conductivity of the system in the agglomerate state is determined by the junction between the nanoparticles, whose tunneling distance, necessary to allow the electron hopping, is about 5-30 nm. As the MWCNTs concentration increases, the nanoparticle junction per unit area increases as well and the electron flowing through the conductive network is facilitated [211].

When the MWCNTs are combined with Biochar, the electrical conductivity follows the trend shown in figure 6.2 (c): in particular, it lowers as Biochar/MWCNTs loading increases. However, the hybrid system shows higher conductivity than the single MWCNTs system, being equal the filler content. A similar behavior was observed by *Li et al.*, who measured the electrical conductivity of an epoxy system containing CNTs and graphene nanoplatelets. They found that the electrical conductivity of the hybrid system improves by about 100 times compared to the single graphene nanoplatelets counterpart. The authors ascribe this behavior to the formation of CNTs agglomerates, responsible for the generation of multiple electron pathways through the two fillers [186]. Similarly, *Sumfleth et al.* explained the enhancement of the electrical conductivity of the hybrid epoxy system containing carbon black and MWCNTs. In this latter case, the carbon black aggregates shortcut the MWCNTs branches to form addition conductive pathways, in which the higher tunneling contact between the fillers and the lower electric resistance through MWCNTs branches contribute to increase the electrical conductivity [185]. The same hypothesis was used to explain the improvement of the electrical conductivity of the analyzed Biochar/MWCNTs system. The synergistic effect between Biochar and MWCNTs provides the formation of the interconnected network that facilitates the electron transfer throughout the polymer network: the MWCNTs, able to build conducting channels, reduce the gap between the Biochar particles, improving the electrical conductivity above the percolation threshold. Furthermore, the combination with the Biochar, in addition to the improvement of the MWCNTs dispersion in polymer matrix, prevents the damages due to the sonication process, such as the decrease of the nanoparticles aspect ratio. The presence of the Biochar particles could prevent the breaking of the MWCNTs that, during the sonication process, are subjected to high vibrational power. In the hybrid system the Biochar, preventing the direct exposure of the MWCNTs to the high mixing power, preserve the length of the nanoparticles required to build the bridges between the fillers and ensure the effective electron conductivity [212].

6.3 Optical properties

Incorporating fillers into a polymeric matrix is considered an effective strategy to obtain composites with specific optical properties. In particular, the interest is directed to the development of composites, in which the high UV-shielding efficiency is combined with the visible light transparency. As Biochar and MWCNTs are incorporated in the polymeric matrix, their influence on the optical properties of the composite films were investigated. The UV-Vis spectroscopy measurements, performed according to the operating conditions described in the third chapter, provide the UV-Vis transmittance spectra reported in figure 6.3 for each set of composite film at different loading of the Biochar (a), MWCNTs (b) and Biochar/MWCNTs (c). The three graphs in figure 6.3 reveal the influence of the filler type and loading, as well as of their dispersion degree in the thermosetting matrix, on the optical properties of the composite films. On the wide wavelength spectrum, three ranges can be detected corresponding to the UV (200-400 nm), Visible (400-800 nm) and IR (800-1000 nm) region.

The optical behavior of the three polymeric composite systems is compared with that of unfilled EB150 film characterized by poor UV shielding properties and transparency in the whole visible light region. This behavior is retained in Biochar based composite films, as also at the highest filler content the transmittance in the visible light range is kept at 50%.

Conversely, the introduction of the MWCNTs leads to a significant change of the optical properties of the unfilled resin, which are more evident as the filler content increases. While the UV and visible transparency are not affected at the lowest filler loading, as the filler content increases, the MWCNTs clustering phenomena contribute to the UV shielding effect. Besides, at the highest MWCNTs loadings the transmittance drops down to zero on the whole wavelength spectrum, indicating the total UV and visible light absorption because of the incorporation of the MWCNTs.

In the hybrid system, the combination of the Biochar and MWCNTs exhibits two opposite behaviors compared to unfilled EB150. With low filler loadings (0.01-0.1 wt.%), the system is characterized by poor UV shielding effect and visible light transparency with transmittance retained up to 40%, similarly to the Biochar composite system. As the filler concentration increases (0.5-1.0 wt.%), the UV and visible light are absorbed on the whole spectrum and the transmittance of the hybrid system is close to zero, analogously to the MWCNTs containing systems. The low transmittance of the hybrid films is attributed to the scattering effect rather than the MWCNTs light absorption. This result indicates that the scattering effect of the MWCNTs prevails on the visible light transparency retained in the Biochar based composite films [213].

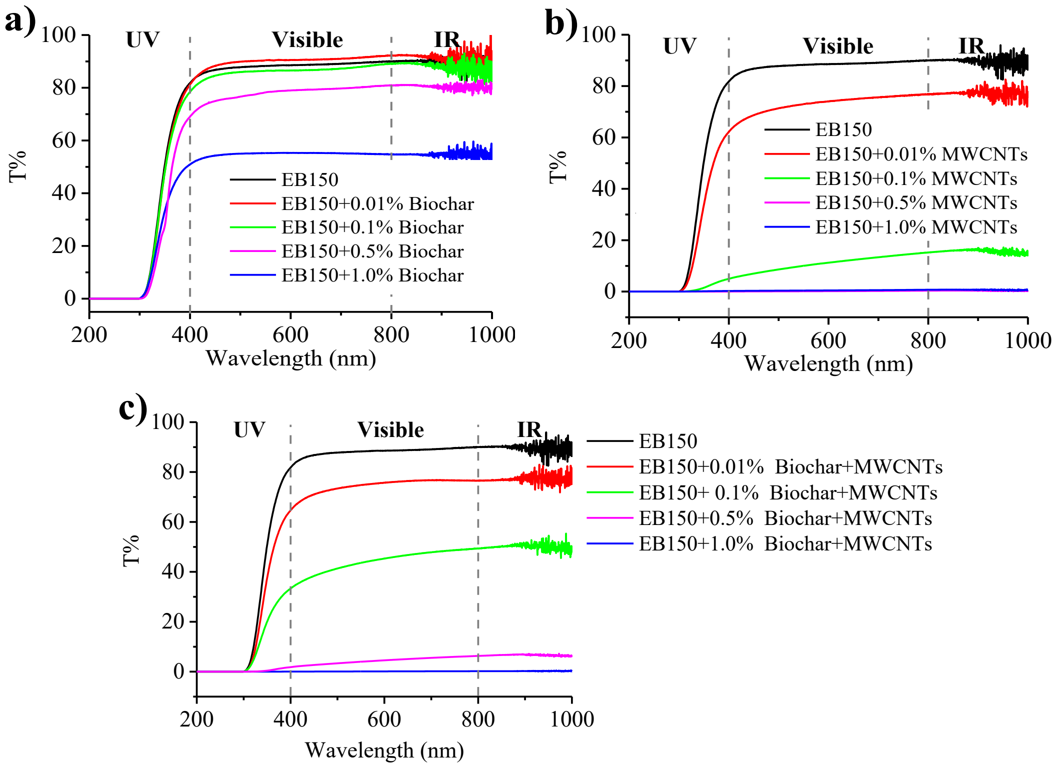

Figure 6.3. UV-Vis spectra of films containing (a) Biochar, (b) MWCNTs, (c) Biochar/MWCNTs in concentration ranging from 0.01 to 1.00 wt.%.

Conclusions

In this dissertation, the UV-LED curing technology was exploited as an effective method to design carbon-based composite coatings. The ethoxy-acrylate resin, used as polymeric matrix, was reinforced with Biochar and MWCNTs, investigated as carbon-rich fillers. Biochar and MWCNTs, both as single and mixed (1:1 weight ratio) fillers, were incorporated in the host polymer at different loadings, ranging from 0.01 to 1.0 wt.%. The three systems were thoroughly studied to investigate the influence of the filler type and loadings on the effectiveness of the UV-LED curing process and the structure-property relationships of the obtained composite films.

Since its cost-effective and eco-friendly benefits, UV-LED curing was selected as a suitable alternative to the conventional thermal curing processes. The combination between the exposure factors and the formulation components was crucial to ensure the effectiveness of the UV-LED curing process. In particular, the energy density and irradiance as well as the content of the photo-initiator resulted effective to ensure the depth curing of the acrylic system. The operating conditions were found suitable also when Biochar and MWCNTs were added to the curable formulation: the filler loadings, up to 1.0 wt.%, did not affect the completeness of the UV-LED curing process as proved by FTIR analysis.

After having been incorporated in the curable formulation by sonication, Biochar and MWCNTs exhibited different filler-polymer matrix interactions depending on their particle size and shape. The morphology is correlated to the precursor of the two carbon fillers: Biochar was obtained by the pyrolysis of the spent coffee grounds, MWCNTs by CVD synthesis of the hydrocarbons. According to the different nature of the two fillers, the morphological analysis revealed the sponge-like structure of the micrometric Biochar particles and the combed yarn structure of the nanometric MWCNTs. During the dispersion process, the Biochar particles were embedded in the polymer matrix that was able to get into the macro-pores of the filler, hence forming an interconnected network. The high surface-volume ratio of the nanometric MWCNTs particles was found responsible for the large filler-polymer matrix interphase region that contributed to the generation of the micrometric clusters at the highest filler loadings. The dispersion of MWCNTs was improved when the nanometric fillers were combined with the Biochar particles that exerted a shuttle effect by interacting with the graphitic surface of the nanoparticles, through π-π stacking.

The Biochar particles, combined with the MWCNTs, were also responsible for the decrease of the complex viscosity of the curable system, through a lubrication effect on the polymer chains. When Biochar was combined with MWCNTs, the lubrication effect of the Biochar prevailed over the nanoparticle interactions at low filler loadings: with increasing MWCNTs content, the complex viscosity increased as well, because of stronger nanoparticle interactions. The latter caused the formation of the MWCNTs clusters that impacted on the macroscopic properties of the UV-LED cured composite coatings. Since the addition of the Biochar was not effective to enhance the MWCNTs dispersion at the highest filler loadings, the improvement of the mechanical performance of the composite films was negligible. Similarly, in the Biochar based composite coatings, the selected filler loadings were not enough to improve the storage modulus of the UV-LED cured composite films.

The MWCNTs bundles impacted also the thermal conductivity of the UV-LED composite films. Above the percolation threshold, the thermal conductivity decreased as a consequence of the formation of micrometric MWCNTs clusters, which is detrimental for the thermal transport. Conversely, the homogeneous dispersion of the Biochar particles in the polymer matrix allowed increasing the thermal conductivity as a function of the filler content. When combined with the MWCNTs, the Biochar improved the thermal conductivity at the lowest filler content but, above that, nanoparticles agglomeration phenomena occurred, which hindered the thermal transport.

The clustering phenomena, disadvantageous for the thermal transport, promoted the electrical conductivity of the composite films: in particular, a decrease of the resistance up to three order of magnitude was observed with the increase of the MWCNTs content. Besides, while the electrical conductivity of the Biochar based composites remained almost unchanged above the percolation threshold, it increased as the two fillers were incorporated together. Indeed, the concurrent presence of both the fillers in the hybrid system accounted for the formation of an interconnected network through the π-π stacking, promoting the transfer of the electrons and, thus, improving the electrical conductivity with respect to the single filler composite counterparts.

The MWCNTs aggregates influenced also the optical properties of the hybrid film that retained the transparency to the visible light only at the lower filler loading, as observed also in the MWCNTs based composite films. Conversely, the homogenous dispersion of the Biochar in the thermosetting resin favoured the retention of the 50% of transmittance at the highest filler loading.

As this study revealed, the formation of the MWCNTs bundles limited the property performance of the composite coatings. The prevailing filler-filler interaction over that of filler-polymer matrix was detrimental for the mechanical and optical properties as well as for the thermal conductivity. Besides, the increase of the complex viscosity with the MWCNTs content could compromise the handling and the processing of the curable formulation. Once again, these drawbacks were overcome combining the Biochar particles with the MWCNTs: at the lower filler loading, the Biochar accounted for the improvement of the MWCNTs dispersion and promoted the lubrication of the curable formulation. Since the Biochar in the composite system was effective only at the lower filler loading, future investigations could be addressed to the optimization of the weight ratio between the two carbon fillers. A higher Biochar/MWCNTs weight ratio could be advantageous to determine synergism between the two carbon fillers: a better dispersion of the MWCNTs could impart to the polymer matrix higher mechanical and optical properties, as well as thermal conductivity.

The Biochar, added as single carbon filler into the polymer matrix, provided also promising results: in comparison with the MWCNTs, it was responsible for a higher thermal conductivity and more effective optical properties. Such advanced performances suggest that further investigations could be focused on the application of the Biochar as alternative to the MWCNTs. In particular, increased Biochar loadings could be considered to design composite films with superior mechanical properties as well as higher thermal and electrical conductivity. Future developments may include the functionalization of the Biochar particles in order to promote the adhesion between the filler and polymer matrix and, thus, the increase of the T_g and the thermal stability of the host polymer.

The Biochar as carbon filler provides interesting perspectives as its properties, connected to the pyrolysis operating conditions, could be finely tuned. In particular, the Biochar with higher thermal and electrical conductivity could be obtained processing the biomass at higher temperature, which the graphitization grade of the pyrolysis by-product is dependent on. Besides, a wide range of lignocellulosic precursors, both from anthropogenic and biogenic wastes, can be selected for pyrolysis processes, converting the biomasses in high value-added materials, in addition to the spent coffee ground. As biomass-derived product, the Biochar represents, therefore, a valuable resource: in fact, it is an eco-friendly and inexpensive material that could be exploited as sustainable alternative to the more expensive fossil-fuel carbon fillers, promoting the implementation of the circular economy concept.

References

[1] C. Dreyer, F. Mildner, Application of LEDs for UV-Curing, *III-Nitride Ultraviolet Emitters*, 15 (2016) 415-434.

[2] A. Javadi, H. S. Mehr, M. Sobani, M. D. Soucek, Cure-on-command technology: A review of the current state of the art, *Progress in Organic Coatings* 100 (2016) 2-31.

[3] X. Wang, Y. Feng, Li Zhang, I. Protsak, R. Jamali, Y. Shu, P. Pal, Z.Wang, J. Yang, D. Zhang, Fast-cured UV-LED polymer materials filled with high mineral contents as wear-resistant, antibacterial coatings, *Chemical Engineering Journal* 382 (2020)122927.

[4] Y. Muramoto, M. Kimura, S. Nouda, Development and future of ultraviolet light-emitting diodes: UV-LED will replace the UV lamp, *Semiconductor Science and Technology* 29 (2014) 084004.

[5] W. A. Green, Industrial photoinitiators: A technical guide, *Taylor and Francis Group*, LLC (2010).

[6] K.D. Jandt, R.W. Millsc, A brief history of LED photopolymerization, *Dental Materials*, 29 (2013) 605-617.

[7] C. Dietlin, S. Schweizer, P. Xiao, J. Zhang, F. M. Savary, B. Graff, J.P. Fouassier, J. Lalevée, Photopolymerization Upon LEDs: New Photoinitiating Systems and Strategies, *Polymer Chemistry* 6 (2015) 3895-3912.

[8] K. C. Anyaogu, A.A. Ermoshkin, D. C. Neckers, A. Mejiritski, O. Grinevich, A. V. Fedorov, Performance of the Light Emitting Diodes Versus Conventional Light Sources in the UV Light Cured Formulations, *Journal of Applied Polymer Science* 105 (2007) 803–808.

[9] F.K. Yam, Z. Hassan, Innovative advances in LED technology, *Microelectronics Journal* 36 (2005) 129–137.

[10] S.L. McDermott, J.E. Walsh, R.G. Howard, A comparison of the emission characteristics of UV-LEDs and fluorescent lamps for polymerisation applications, *Optics & Laser Technology* 40 (2008) 487–493.

[11] F. A. Rueggeberg, State-of-the-art: Dental photocuring—A review, Dental Materials 27 (2011) 39-52.

[12] D.L. Leonard, D.G. Charlton, H.W. Roberts et al., Polymerization efficiency of LED curing lights. *J. Esthet. Restor. Dent.* 14 (2002) 286–295.

[13] C. Kurachi, A.M. Tuboy, D.V. Magalhães et al., Hardness evaluation of a dental composite polymerized with experimental LED-based devices. *Dent. Mater.* 17 (2001) 309–317

[14] K.S. Vandewalle, H.W. Roberts, J.L. Nadrus et al., Effect of light dispersion of LED curing lights on resin composite polymerization. *J. Esthet. Restor. Dent.* 17 (2005) 244–255.

[15] J.W. Stansbury, Curing dental resins and composites by photopolymerization. *J. Esthet. Dent.* 12 (2000) 300–308.

[16] J.G. Kim, C.M. Chung, Trifunctional methacrylate monomers and their photocured composites with reduced curing shrinkage, water sorption, and water solubility. *Biomaterials* 24 (2003) 3845–3851.

[17] C.N. Bowman, N.B. Cramer, J.W. Stansbury, Recent advances and developments in composite dental restorative materials. *J. Dent. Res.* 90 (2011) 402–416.

[18] H. Wang, X. Miao, M. Zhu et al., Synthesis of dental resins using diatomite and nano-sized SiO2 and TiO2. *Prog. Nat. Sci.* 22 (2012) 94–99.

[19] M. Zhu, F. Liu, R. Wang et al., Novel Ag nanocrystals based dental resin composites with enhanced mechanical and antibacterial properties. Prog. Nat. Sci. 23 (2013) 573–578.

[20] Jack L. Ferracane, Resin composite—State of the art, *Dental Materials* 27 (2011) 29–38.

[21] V. Landry, B. Riedl, P. Blanchet, Nanoclay dispersion effects on UV coatings curing. *Prog. Org. Coat.* 62 (2008) 400–408.

[22] C. Decker, L. Keller, K. Zahouily et al., Synthesis of nanocomposite polymers by UV-radiation curing. *Polymer* 46 (2005) 6640–6648.

[23] D. Zhao, S. Liu, Y. Wu, T. Guan, N. Sun, B. Ren, Self-healing UV light-curable resins containing disulfide group: Synthesis and application in UV coatings, *Progress in Organic Coatings* 133 (2019) 289-298.

[24] D. Puglia, J. M. Kenny, Chapter 7 - Structure-property relationships of thermoset nanocomposites, *Thermosets (Second Edition) Structure, Properties, and Applications* (2018) 231-276.

[25] A. Martin, S. Teychené, S. Camy, J. Aubin, Fast and inexpensive method for the fabrication of transparent pressure-resistant microfluidic chips, *Microfluid Nanofluid* 20 (2016) 92.

[26] E. A. Kandirmaz, Printing of UV-curable transparent conductive polymer composite, *Journal of Macromolecular Science, Part A: Pure and Applied Chemistry* 57 (2019) 139–144.

[27] X. Li, Z. Liu, P. Hong, L. Chen, X. Liu, Synthesis of organic and inorganic hybrid nanoparticles as multifunctional photoinitiator and its application in UV-curable epoxy acrylate-based coating systems, *Progress in Organic Coatings* 141 (2020) 105565.

[28] S.V. Asmussen, C. I. Vallo, Facile preparation of silver-based nanocomposites via thiol-methacrylate ‘click’ photopolymerization, *European Polymer Journal* 79 (2016) 163–175.

[29] C.E. Hoyle, T. Roper, B. Pan, C. Nason, T.Y. Lee, T. Turner, S. Jönsson, Advances in the polymerization of thiol–ene formulations. *RadTech NA: Bethesda, MD*, 1 (2003) 573–578.

[30] M. R. Zonca Jr., B. Falk, J. V. Crivello, LED-Induced Thiol-Ene Photopolymerizations, *Journal of Macromolecular Science*, A 41 (2004), 741–756.

[31] P. Loginos, A. Patsidis, V. Georgakilas, UV-Cured Poly (Ethylene Glycol) Diacrylate/Carbon Nanostructure Thin Films. Preparation, Characterization, and Electrical Properties, *J. Compos. Sci.* 4 (2020) 4.

[32] G. Malucelli, Synthesis and Characterization of UV-LED Curable Nanocomposite Coatings, *Current Organic Chemistry* 21 (2017) 2314-2321.

[33] M. Hubert, C. Dimas, P. Orava, J. Koo, High power UV LED array for curing photoadhesives, *Applications of Photonic Technology* 5260 (2003) 163-167.

[34] X. Zhang, Y. Duan, X. Zhao, D. Li, UV stepwise cured fabrication of glass fiber/acrylate composites: Effects of exposure dose on curing uniformity and interlaminar shear strength, *Journal of Composite Materials*, 50 (2016) 1395-1401.

[35] N. Bhattacharjee, A. Urrios, S. Kang, A. Folch, The upcoming 3D-printing revolution in microfluidics, *Lab on a Chip* 16 (2016) 1720-1742.

[36] F.P.W. Melchels, J. Feijen, D.W. Grijpma, A review on stereolithography and its applications in biomedical engineering, *Biomaterials* 31 (2010) 6121–6130.

[37] R. Xie, D. Li, Research on the curing performance of UV-LED light based stereolithography, *Optics & Laser Technology* 44 (2012) 1163–1171.

[38] B.H. Kang, S.Y. Shin, Experiment of solidifying photo sensitive polymer by using UV LED, in *Proceedings of the SPIE 7266*, *Optomechatronic Technologies*, San Diego (2008).

[39] M. W. M. Cunico, J. de Carvalho, Development of novel additive manufacturing technology: an investigation of a selective composite formation process, *Rapid Prototyping Journal* 22 (2016) 51 – 66.

[40] M. Faes, J. Vleugels, F. Vogeler, E. Ferraris, Extrusion-based additive manufacturing of ZrO2 using photoinitiated polymerization, *CIRP Journal of Manufacturing Science and Technology* 14 (2016) 28-34.

[41] S. Abele, F. Q. Nie, F. Foret, B. Paulla, M. Macka, UV-LED photopolymerised monoliths, *Analyst* 133 (2008) 864-866.

[42] R. Schwalm, The UV curing process, in: R. Schwalm (Ed.), UV Coatings, Elsevier, Amsterdam, Chapter 2 (2007) 19–61.

[43] P. Mills, Robotic UV Curing for Automotive Exterior Applications: A cost-effective and technically viable alternative for UV curing, *North American Automotive UV Consortium Report* (2005).

[44] G. A. Thommes, V. J. Webers, Spectral response of photosensitive systems. General effect of radiation attenuation throughout coating thickness, *Journal of imaging science* 29 (1985) 112-116.

[45] N. Seao, UV coating: Basic, Recent Development and New Application RadTech Asia, Osaka (1991) 478–484.

[46] P. I. Dolez, Application of nanomaterials in textile coatings and finishes, *Nanomaterials-Based Coatings* (2019) 139-169.

[47] M. Rallini, M. Natali, M. Monti, J.M. Kenny, L. Torre, Effect of alumina nanoparticles on the thermal properties of carbon fibre-reinforced composites, *Fire Mater.* 38 (2014) 339–355.

[48] J. Lin, C.M. Ma, W. Tai, W. Chang, C. Tsa, Carbon fiber reinforced phenolic resin/silica ceramer composites-processing, mechanical and thermal properties, *Polym.Compos.* 27 (2) (2000) 305–311.

[49] D.L. Chung, Electromagnetic interference shielding effectiveness of carbon materials, *Carbon* 39 (2001) 279–285.

[50] S.Y. Yang, W.N. Lin, Y.L. Huang, H.W. Tien, J.Y. Wang, C.C.M. Ma, S.M. Li, Y.S. Wang, Synergetic effects of graphene platelets and carbon nanotubes on the mechanical and thermal properties of epoxy composites, *Carbon* 49 (2011) 793–803.

[51] M. Hussain, A. Nakahira, K. Niihara, Mechanical property improvement of carbon fiber reinforced epoxy composites by Al_2O_3 filler dispersion, *Mater. Lett.* 26 (1996) 185–191.

[52] A.L. Higginbotham, J.R. Lomeda, A.B. Morgan, J.M. Tour, Graphite oxide flameretardant polymer nanocomposites, *ACS Appl. Mater. Interfaces* 1 (10) (2009) 2256–2261.

[53] F. Laoutid, L. Bonnaud, M. Alexandre, J.M. Lopez-Cuesta, P. Dubois, New prospects in flame retardant polymer materials: from fundamentals to nanocomposites, *Mater. Sci. Eng. R* 63 (2009) 100–125.

[54] Y.W. Mai, Z.-Z. Yu, Polymer Nanocomposites, Woodhead Publishing Ltd, Cambridge, England, 2006.

[55] J.J. Luo, I.M. Daniel, Characterization and modeling of mechanical behavior of polymer/clay nanocomposites, *Compos. Sci. Technol.* 63 (11) (2003) 1607–1616.

[56] D. Ciprari, K. Jacob, R. Tannenbaum, Characterization of polymer nanocomposite interphase and its impact on mechanical properties, *Macromolecules* 39 (19) (2006) 6565–6573.

[57] V. Kovacevic, S. Lucic, M.J. Leskovac, Morphology and failure in nanocomposites. Part I: structural and mechanical properties, *Adhes. Sci. Technol.* 16 (2002) 1343–1365.

[58] R. Qiao, L.C. Brinson, Simulation of interphase percolation and gradients in polymer nanocomposites, *Compos. Sci. Technol.* 69 (3–4) (2009) 491–499.

[59] L. Wang, K. Wang, L. Chen, Y. Zhang, C. He, Preparation, morphology and thermal/mechanical properties of epoxy/nanoclay composite, *Compos. Part A* 37 (2006) 1890–1896.

[60] K. Kunz, B. Krause, B. Kretzschmar, L. Juhasz, O. Kobsch, W. Jenschke, M. Ullrich, P. Pötschke, Direction Dependent Electrical Conductivity of Polymer/Carbon Filler Composites, *Polymers* 11 (2019) 591-18.

[61] M. Aravand, S. V. Lomov, I. Verpoest, L. Gorbatikh, Evolution of carbon nanotube dispersion in preparation of epoxy-based composites: From a masterbatch to a nanocomposite, *eXPRESS Polymer Letters* 8 (2014) 596–608.

[62] Y. Cui, S. Kumar, B.R. Kona, D. van Houcke, Gas barrier properties of polymer/clay nanocomposites, *RSC Adv.* 5 (2015) 63669–63690.

[63] Y.Y. Huang, E.M. Terentjev, Dispersion of carbon nanotubes: mixing, sonication, stabilization, and composite properties, *Polymers* 4 (2012) 275–295.

[64] D. Puglia, L. Valentini, I. Armentano, J.M. Kenny, Effects of single-walled carbon nanotube incorporation on the cure reaction of epoxy resin and its detection by Raman spectroscopy, *Diam. Relat. Mater.* 12 (2003) 827–832.

[65] M. Monti, I. Armentano, G. Faiella, V. Antonucci, J.M. Kenny, L. Torre, M. Giordano, Toward the microstructure–properties relationship in MWCNT/epoxy composites: percolation behavior and dielectric spectroscopy, *Compos. Sci. Technol.* 96 (2014) 38–46.

[66] B.X. Yang, K.P. Pramoda, G.Q. Xu, S.H. Goh, Mechanical reinforcement of polyethylene using polyethylene-grafted multiwalled carbon nanotubes, *Adv. Funct. Mater.* 17 (13) (2007) 2062–2069.

[67] J. Zhu, H.Q. Peng, F. Rodriguez-Macias, J.L. Margrave, V.N. Khabashesku, A. M. Imam, K. Lozano, E.V. Barrera, Reinforcing epoxy polymer composites through covalent integration of functionalized nanotubes, *Adv. Funct. Mater.* 14 (7) (2004) 643–648.

[68] M. Hosur, R. Barua, S. Zainuddin, A. Kumar, J. Trovillion, S. Jeelani, Effect of Processing Techniques on the Performance of Epoxy/MWCNT Nanocomposites, *J. Appl. Polym. Sci.* 127 (2013) 4211-4224.

[69] H. Kim, A.A. Abdala, C.W. Macosko, Graphene/polymer nanocomposites, *Macromolecules* 43 (2010) 6515–6530.

[70] S. Liu, V. S. Chevali, Z. Xu, D. Hui, H. Wang, A review of extending performance of epoxy resins using carbon nanomaterials, *Composites Part B* 136 (2018) 197-214.

[71] M. J. Yee, N.M. Mubarak, E.C. Abdullah, M. Khalid, R. Walvekar, R. R. Karri, S. Nizamuddin, A. Numanb, Carbon nanomaterials based films for strain sensing application—A review, *Nano-Structures & Nano-Objects* 18 (2019) 100312-16.

[72] A.A. Balandin, S. Ghosh, W. Bao, I. Calizo, D. Teweldebrhan, F. Miao, C.-N. Laus, Superior thermal conductivity of single-layer graphene, *Nano Lett.* 8 (2008) 902–907.

[73] C. Lee, X. Wei, J.W. Kysar, J. Hone, Measurement of the elastic properties and intrinsic strength of monolayer graphene, *Science* 321 (2008) 385–388.

[74] K.S. Novoselov, A.K. Geim, S.V. Morozov, D. Jiang, M.I. Katsnelson, I.V. Grigorieva, S. V. Dubonos, A. A. Firsov, Two-dimensional gas of massless Dirac fermions in graphene, *Nature* 438 (2005) 197.

[75] U.K. Sur, Graphene: A rising star on the horizon of materials science, *Int. J. Electrochem.* 2012 (2012).

[76] D. D. L. Chung, Review Graphite, *Journal of Materials Science* 37 (2002) 1475-1489.

[77] M.H. Al-Saleh, U. Sundararaj, Review of the mechanical properties of carbon nanofiber/polymer composites, *Composites A* 42 (2011) 2126–2142.

[78] W.-T. Tsai, The potential of pyrolysing exhausted coffee residue for the production of Biochar, *Handbook of Coffee Processing By-Products* (2017) 299-322.

[79] V. Strezov, M. Patterson, V. Zymla, K. Fisher, T. J. Evans, P. F. Nelson, Fundamental aspects of biomass carbonisation, *J. Anal. Appl. Pyrolysis* 79 (2007) 91–100.

[80] A.V. Bridgwater, Review of fast pyrolysis of biomass and product upgrading, *Biomass and Bioenergy* 38 (2012) 68-94.

[81] X. Cao, K.S. Ro, J.A. Libra, C.I. Kammann, I. Lima, N. Berge, et al., Effects of biomass types and carbonization conditions on the chemical characteristics of hydrochars, *J. Agric. Food Chem.* 61 (39) (2013) 9401.

[82] K. Wiedner, C. Rumpel, C. Steiner, A. Pozzi, R. Maas, B. Glaser, Chemical evaluation of chars produced by thermochemical conversion (gasification, pyrolysis and hydrothermal carbonization) of agro-industrial biomass on a commercial scale, *Biomass Bioenergy* 59 (2013) 264-278.

[83] S. Malghani, G. Gleixner, S.E. Trumbore, Chars produced by slow pyrolysis and hydrothermal carbonization vary in carbon sequestration potential and greenhouse gases emissions, *Soil Biol. Biochem.* 62 (2013) 137.

[84] R. S. Gabhi, D. W. Kirk, C. Q. Jia, Preliminary investigation of electrical conductivity of monolithic Biochar, *Carbon* 116 (2017) 435-442.

[85] Y. Chen, X. Zhang, W. Chen, H. Yang, H. Chen, The structure evolution of Biochar from biomass pyrolysis and its correlation with gas pollutant adsorption performance, *Bioresource Technology* 246 (2017) 101–109.

[86] R. Ktori, P. Kamaterou, A. Zabaniotou, Spent coffee grounds valorization through pyrolysis for energy and materials production in the concept of circular economy, *Materials Today: Proceedings* 5 (2018) 27582–27588.

[87] S. K. Karmee, A spent coffee grounds based biorefinery for the production of biofuels, biopolymers, antioxidants and biocomposites, *Waste Management* 72 (2018) 240–254.

[88] D. R. Vardon, B. R. Moser, W. Zheng, K. Witkin, R. L. Evangelista, T. J. Strathmann, K. Rajagopalan, B. K. Sharma, Complete Utilization of Spent Coffee Grounds To Produce Biodiesel, Bio-Oil, and Biochar, *Sustainable Chem. Eng.* 1 (2013) 1286−1294.

[89] F. R. Oliveira, A. K. Patel, D. P. Jaisi, S. Adhikari, H. Lu, S. K. Khanal, Environmental application of Biochar: Current status and perspectives, *Bioresource Technology* 246 (2017) 110–122.

[90] W.-T. Tsai, S.-C. Liu, C.-H. Hsieh, Preparation and fuel properties of Biochars from the pyrolysis of exhausted coffee residue, *Journal of Analytical and Applied Pyrolysis* 93 (2012) 63–67.

[91] J. S. Cha, S. H. Park, S.-C. Jung, C. Ryu, J.-K. Jeon, M.-C. Shin, Y.-K. Park, Production and utilization of Biochar: A review, *Journal of Industrial and Engineering Chemistry* 40 (2016) 1–15.

[92] C. Kourmentza, Ch.N. Economou, P. Tsafrakidou, M. Kornaros, Spent coffee grounds make much more than waste: Exploring recent advances and future exploitation strategies for the valorization of an emerging food waste stream, *Journal of Cleaner Production* 172 (2018) 980-992.

[93] J. McNutt, Q. S. He, Spent coffee grounds: A review on current utilization, *Journal of Industrial and Engineering Chemistry* 71 (2019) 78–88.

[94] R. Campos-Vega, G. Loarca-Piña, H. A. Vergara-Castañeda, B. D. Oomah, Spent coffee grounds: A review on current research and future prospects, *Trends in Food Science & Technology* 45 (2015) 24-36.

[95] A. Kovalcik, S. Obruca, I. Marova, Valorization of spent coffee grounds: A review, *Food and Bioproducts Processing* 110 (2018) 104-119.

[96] T. E. Rufford, D. Hulicova-Jurcakova, Z. Zhu, G. Q. Lu, Nanoporous carbon electrode from waste coffee beans for high performance supercapacitors, *Electrochemistry Communications* 10 (2008) 1594–1597.

[97] P. Fu, S. Hu, L. Sun, J. Xiang, T. Yang, A. Zhang, J. Zhang, Structural evolution of maize stalk/char particles during pyrolysis, *Bioresource Technology* 100 (2009) 4877–4883.

[98] Y. Chen, H. Yang, X. Wang, S. Zhang, H. Chen, Biomass-based pyrolytic polygeneration system on cotton stalk pyrolysis: Influence of temperature, *Bioresource Technology* 107 (2012) 411–418.

[99] K. Zeng, D. P. Minh, D. Gauthier, E. Weiss-Hortala, A. Nzihou, G. Flamant, The effect of temperature and heating rate on char properties obtained from solar pyrolysis of beech wood, *Bioresource Technology* 182 (2015) 114–119.

[100] G. R. Surup, H. K. Nielsen, M. Heidelmann, A. Trubetskaya, Characterization and reactivity of charcoal from high temperature pyrolysis (800–1600 °C), *Fuel* 235 (2019) 1544–1554.

[101] A. B. Fuertes, M. Camps Arbestain, M. Sevilla, J. A. Maciá-Agulló, S. Fiol, R. López, R. J. Smernik, W. P. Aitkenhead, F. Arce, F. Macias, Chemical and structural properties of carbonaceous products obtained by pyrolysis and hydrothermal carbonisation of corn stover, *Australian Journal of Soil Research*, 48 (2010) 618–626.

[102] M. Giorcelli, P. Savi, A. Khan, A. Tagliaferro, Analysis of Biochar with different pyrolysis temperatures used as filler in epoxy resin composites, *Biomass and Bioenergy* 122 (2019) 466–471.

[103] J.R. Dennison, M. Holtz, G. Swain, Raman Spectroscopy of Carbon Materials, *Spectroscopy* 11(8) (1996) 38-45.

[104] X. Li, J.-I. Hayashi, C.-Z. Li, FT-Raman spectroscopic study of the evolution of char structure during the pyrolysis of a Victorian brown coal, *Fuel* 85 (2006) 1700–1707.

[105] Y. Zhao, D. Feng, Y. Zhang, Y. Huang, S. Sun, Effect of pyrolysis temperature on char structure and chemical speciation of alkali and alkaline earth metallic species in Biochar, *Fuel Processing Technology* 141, (2016) 54-60.

[106] J. Bourke, M. Manley-Harris, C. Fushimi, K. Dowaki, T. Nunoura, M.J. Antal, Do All Carbonized Charcoals Have the Same Chemical Structure? 2. A

Model of the Chemical Structure of Carbonized Charcoal, Ind. *Eng. Chem. Res.* 46 (2007) 5954-5967.

[107] G. R. Surup, M. Foppe, D. Schubert, R. Deike, M. Heidelmann, M. T. Timkod, A. Trubetskaya, The effect of feedstock origin and temperature on the structure and reactivity of char from pyrolysis at 1300–2800 °C, *Fuel* 235 (2019) 306–316.

[108] M. Bartoli, M. A. Nasir, P. Jagdale, E. Passaglia, R. Spiniello, C. Rosso, M. Giorcelli, M. Rovere, A. Tagliaferro, Influence of pyrolytic thermal history on olive pruning Biochar and related epoxy composites mechanical properties, *Journal of Composite Materials* 20 (2019) 1-11.

[109] S. Li, X. Li, Q. Deng, D. Li, Three kinds of charcoal powder reinforced ultra-high molecular weight polyethylene composites with excellent mechanical and electrical properties, *Materials and Design* 85 (2015) 54–59.

[110] Q. Zhang, M. U. Khan, X. Lin, H. Cai, H. Lei, Temperature varied Biochar as a reinforcing filler for high-density polyethylene composites, *Composites Part B* 175 (2019) 107151-107158.

[111] S. Li, A. Huang, Y.-J. Chen, D. Li, L.-S. Turng, Highly filled Biochar/ultra-high molecular weight polyethylene/linear low density polyethylene composites for high-performance electromagnetic interference shielding, *Composites Part B* 153 (2018) 277–284.

[112] M. Giorcelli, A. Khan, N. M. Pugno, C. Rosso, A. Tagliaferro, Biochar as a cheap and environmental friendly filler able to improve polymer mechanical properties, *Biomass and Bioenergy* 120 (2019) 219–223.

[113] A. Khan, P. Savi, S. Quaranta, M. Rovere, M. Giorcelli, A. Tagliaferro, C. Rosso, C. Q. Jia, Low-Cost Carbon Fillers to Improve Mechanical Properties and Conductivity of Epoxy Composites *Polymers* 9 (2017) 642.

[114] P. Jagdale, D. Ziegler, M. Rovere, J. M. Tulliani, A. Tagliaferro, Waste Coffee Ground Biochar: A Material for Humidity Sensors, *Sensors* 19 (2019) 801.

[115] M. Giorcelli, M. Bartoli, Development of Coffee Biochar Filler for the Production of Electrical Conductive Reinforced Plastic, *Polymers* 11 (2019) 1916-17.

[116] S. Iijima, Helical microtubules of graphitic carbon, *Letters to Nature* 34 (1991) 56-58.

[117] Á. Kukovecz, G. Kozma, Z. Kónya, Multi-Walled Carbon Nanotubes, *Springer Handbook of Nanomaterials*, 40 (2013) 147-188.

[118] L. Liu, H. Zhou, R. Cheng, W.J. Yu, Y. Liu, Y. Chen, et al., High-yield chemical vapor deposition growth of high-quality large-area AB-stacked bilayer graphene*, ACS nano* 6 (2012) 8241–8249.

[119] A. Oberlin, M. Endo, T. Koyama, Filamentous growth of carbon through benzene decomposition, *J Cryst Growth* 32(3) (1976) 335–49.

[120] J. H. Lehman, M. Terrones, E. Mansfield, K. E. Hurst, V. Meunier, Evaluating the characteristics of Multiwall Carbon Nanotubes, *Carbon* 49 (2011) 2581-2602.

[121] L. Guadagno, M. Raimondo, L. Vertuccio, C. Naddeo, G. Barra, P. Longo, P. Lamberti, G. Spinelli, M.R. Nobile, Morphological, rheological and electrical properties of composites filled with carbon nanotubes functionalized with 1-pyrenebutyric acid, *Composites Part B* 147 (2018) 12–21.

[122] M. Endo, K. Takeuchi, T. Hiraoka, T. Furuta, T. Kasai, X. Sun, et al. Stacking nature of graphene layers in carbon nanotubes and nanofibers, *J Phys Chem Solids* 58(11) (1997) 1707–12.

[123] S. Osswald, M. Havel, Y. Gogotsi, Monitoring oxidation of multiwalled carbon nanotubes by Raman spectroscopy, *J. Raman Spectrosc.* 38 (2007) 728–736.

[124] A. M. Rao, E. Richter, S. Bandow, B. Chase, P. C. Eklund, K. A. Williams, et al. Diameter-selective Raman scattering from vibrational modes in carbon nanotubes. *Science* 275(5297) (1997) 187–91.

[125] X. Zhao, Y. Ando, L. C. Qin, H. Kataura, Y. Maniwa, R. Saito Characteristic Raman spectra of multiwalled carbon nanotubes *Physica B* 323(1–4) (2002) 265–6.

[126] M.G. Donato, G. Messina, S. Santangelo, S. Galvagno, C. Milone, A. Pistone, Aid of Raman spectroscopy in diagnostics of MWCNT synthesised by Fe-catalysed CVD *J Phys Conf Ser* 61(1) (2007) 931–5.

[127] R.A. DiLeo, B.J. Landi, R.P. Raffaelle, Purity assessment of multiwalled carbon nanotubes by Raman spectroscopy *J Appl Phys* 101(6) (2007) 064301-1–5.

[128] B. Scheibe, E. Borowiak-Palen, R. J. Kalenczuk, Oxidation and reduction of multiwalled carbon nanotubes preparation and characterization. *Mater Charact* 61(2) (2010) 185–191.

[129] M. Endo, Y. A. Kim, Y. Fukai, T. Hayashi, M. Terrones, H. Terrones, and M. S. Dresselhaus, Comparison study of semi-crystalline and highly crystalline multiwalled carbon nanotubes, *Applied Physics Letters* 79 (2001) 1531-1533.

[130] R. Andrews, D. Jacques, D. Qian, E.C. Dickey, Purification and structural annealing of multiwalled carbon nanotubes at graphitization temperatures, *Carbon* 39 (2001) 1681–1687.

[131] Y.A. Kim, T. Hayashi, K. Osawa, M.S. Dresselhaus, M. Endo, Annealing effect on disordered multi-wall carbon nanotubes, *Chemical Physics Letters* 380 (2003) 319–324.

[132] P.A. Thrower, The study of defects in graphite by transmission electron spectroscopy, *Chem Phys Carbon* 5 (1969) 217–319.

[133] A.J. Stone, D.J. Wales, Theoretical studies of icosahedral C60 and some related species, *Chem Phys Lett* 128(5–6) (1986) 501–3.

[134] A. Peigney, Ch. Laurent, E. Flahaut, R.R. Bacsa, A. Rousset, Specific surface area of carbon nanotubes and bundles of carbon nanotubes, *Carbon* 39 (2001) 507–514.

[135] Q.-H. Yang, P.-X. Hou, S. Bai, M.-Z. Wang, H.-M. Cheng, Adsorption and capillary of nitrogen in aggregated multi-walled carbon nanotubes, *Chemical Physics Letters* 345 (2001) 18-24.

[136] Z. Kónya, J. Zhu, K. Niesz, D. Mehn, I. Kiricsi, End morphology of ball milled carbon nanotubes, *Carbon* 42 (2004) 2001–2008.

[137] W. D. Shen, B. Jiang, B. S. Han, S. S. Xie, Investigation of the radial compression of carbon nanotubes with a scanning probe microscope. *Phys RevLett* 84(16) (2000) 3634–7.

[138] M. M. J. Treacy, T. W. Ebbesen, J. M. Gibson, Exceptional high Young's modulus observed for individual carbon nanotubes, *Nature* 381 (1996) 678-680.

[139] I. Palaci, S. Fedrigo, H. Brune, C. Klinke, M. Chen, E. Riedo, Radial Elasticity of Multiwalled Carbon Nanotubes, *Physical Review Letters* 94 (2005)175502-4.

[140] M.-F. Yu, O. Lourie, M. J. Dyer, K. Moloni, T. F. Kelly, R. S. Ruoff, Strength and Breaking Mechanism of Multiwalled Carbon Nanotubes Under Tensile Load, *Science* 287 (2000) 637-640.

[141] Z. Han, A. Fina, Thermal conductivity of carbon nanotubes and their polymer nanocomposites: A review, *Progress in Polymer Science* 36 (2011) 914–944.

[142] Y. Ando, X. Zhao, H. Shimoyama, G. Sakai, K. Kaneto, Physical properties of multiwalled carbon nanotubes, *International Journal of Inorganic Materials* 1 (1999) 77–82.

[143] D.J. Yang, S.G. Wang, Q. Zhang, P.J. Sellin, G. Chena, Thermal and electrical transport in multi-walled carbon nanotubes, *Physics Letters A* 329 (2004) 207–213.

[144] M. Gaillard, H. Mbitsi, A. Petit, E. Amin-Chalhoub, C. Boulmer-Leborgne, N. Semmar, E. Millon, J. Mathias, S. Kouassi, Electrical and thermal characterization of carbon nanotube films, *Journal of Vacuum Science & Technology B* 29 (2011) 041805-8.

[145] D. J. Yang, Q. Zhang, G. Chen, S. F. Yoon, J. Ahn, S. G. Wang, Q. Zhou, Q. Wang, J. Q. Li, Thermal conductivity of multiwalled carbon nanotubes, *Physical Review B* 66 (2002) 165440-6.

[146] W. Lin, J. Shang, W. Gu, C.P. Wong, Parametric study of intrinsic thermal transport in vertically aligned multi-walled carbon nanotubes using a laser flash technique, *Carbon* 50 (2012) 1591-1603.

[147] P. Kim, L. Shi, A. Majumdar, P. L. McEuen, Thermal Transport Measurements of Individual Multiwalled Nanotubes, *Physical Review Letters* 87 (2001) 215502-4.

[148] T. Y. Choi, D. Poulikakos, J. Tharian, U. Sennhauser, Measurement of thermal conductivity of individual multiwalled carbon nanotubes by the 3-ω method, *Applied Physics Letters* 87 (2005) 013108-3.

[149] R. Prasher, Thermal boundary resistance and thermal conductivity of multiwalled carbon nanotubes, *Physical Review B* 77 (2008) 075424-11.

[150] H. Xie, A. Cai, X. Wang, Thermal diffusivity and conductivity of multiwalled carbon nanotube arrays, *Physics Letters A* 369 (2007) 120–123.

[151] E. Frackowiak, K. Metenier, V. Bertagna, F. Beguin, Supercapacitor electrodes from multiwalled carbon nanotubes, *Appl. Phys. Lett.* 77 (2000) 2421-2423.

[152] S. Bose, R.A. Khare, P. Moldenaers: Assessing the strengths and weaknesses of various types of pretreatments of carbon nanotubes on the properties of polymer/carbon nanotubes composites: A critical review, *Polymer* 51(5) (2010) 975–993.

[153] P. Verge, S. Benali, L. Bonnaud, A. Minoia, M. Mainil, R. Lazzaroni, P. Dubois: Unpredictable dispersion states of MWNTs in HDPE: A comparative and comprehensive study, *Euro. Polymer J.* 48(4) (2012) 677–683.

[154] X.L. Xie, Y.W. Mai, X.P. Zhou: Dispersion and alignment of carbon nanotubes in polymer matrix, a review, *Mater. Sci. Eng. R* 49(4) (2005) 89–112.

[155] G.W.H. Höhne, W.F. Hemminger, HJ. Flammersheim, Types of Differential Scanning Calorimeters and Modes of Operation. In: *Differential Scanning Calorimetry. Springer, Berlin, Heidelberg* (2003).

[156] S. Mutlur, Thermal Analysis of Composites Using DSC, In: *Advanced Topics in Characterization of Composites* (2004).

[157] C. De Blasio, Basic Principles of Thermogravimetric Analysis, Fundamentals of Biofuels Engineering and Technology, *Green Energy and Technology*, Springer Nature Switzerland AG (2019).

[158] S. Vyazovkin, Thermogravimetric Analysis, Characterization of Materials, John Wiley & Sons, Inc. (2012).

[159] R. E. Wetton, R. D. L. Marsh, J. G. Van-de-Velde, Theory and Application of Dynamic Mechanical Thermal Analysis, *Thermochimica Acta*, 175 (1991) 1-11.

[160] K. P. Menard, N. Menard, Dynamic Mechanical Analysis, *Encyclopedia of Analytical Chemistry*, *JohnWiley & Sons, Ltd.* (2017).

[161] H. Förster, UV/VIS Spectroscopy, *Mol. Sieves* 4 (2004) 337–426.

[162] M. H. Penner, Basic Principles of Spectroscopy, *Springer International Publishing* (2017).

[163] P. J. Larkin, Chapter 3 - Instrumentation and Sampling Methods, *Infrared and Raman Spectroscopy (Second Edition)* (2018) 29-61.

[164] G. Rame, B. Lendl, Attenuated Total Reflection Fourier Transform Infrared Spectroscopy, Encyclopedia of Analytical Chemistry, *John Wiley & Sons, Ltd.* (2013).

[165] D. Semnani, Chapter 7-Geometrical characterization of electrospun nanofibers, *Electrospun Nanofibers* (2017) 151-180.

[166] J. Pawley, The Development of Field-Emission Scanning Electron Microscopy for Imaging Biological Surfaces, *Scanning* 19 (1997) 324-336.

[167] H. A. Barnes, A Handbook of Elementary Rheology, University of Wales Institute of Non-Newtonian Fluid Mechanics, Aberystwyth (2000).

[168] H. Zhang, M.-J. Li, W.-Z. Fang, D. Dan, Z.-Y. Li, W.-Q. Tao, A numerical study on the theoretical accuracy of film thermal conductivity using transient plane source method, *Applied Thermal Engineering* 72 (2014) 62-69.

[169] A. Elkholy, H. Sadek, R. Kempers, An improved transient plane source technique and methodology for measuring the thermal properties of anisotropic materials, *International Journal of Thermal Sciences* 135 (2019) 362–374.

[170] A. R. Blythe, Electrical Resistivity Measurements of Polymer Materials, *Polymer Testing* 4 (1984) 195-209.

[171] Y. Singh, Electrical Resistivity Measurements: A review, *International Journal of Modern Physics: Conference Series* 22 (2013) 745–756.

[172] A. P. Schuetze, W. Lewis, C. Brown, W. J. Geerts, A laboratory on the four-point probe technique, *American Journal of Physics* 72 (2004) 149-153.

[173] F. M. Smits, Measurement of Sheet Resistivities with the Four-Point Probe, *The Bell System Technical Journal* 34 (1955) 712-718.

[174] P. Carion, A. Ibrahim, X. Allonas, C. Croutxé-Barghorn, G. L'Hostis, Frontal Free-Radical Photopolymerization of Thick Samples: Applications to LED-Induced Fiber-Reinforced Polymers, *Inc. J. Polym. Sci., Part A: Polym. Chem.* 57 (2019) 898–906.

[175] I. Alig, P. Pötschke, D. Lellinger, T. Skipa, S. Pegel, G. R. Kasaliwal, T. Villmow, Establishment, morphology and properties of carbon nanotube networks in polymer melts, *Polymer* 53 (2012) 4-28.

[176] D. Matykiewicz, Biochar as an effective filler of Carbon Fiber reinforced Bio-Epoxy composites, *Processes* 8 (2020) 724-737.

[177] M. Giorcelli, A. Khan, N. M. Pugno, Carlo Rosso, Alberto Tagliaferro, Biochar as a cheap and environmental friendly filler able to improve polymer mechanical properties, *Biomass and Bioenergy* 120 (2019) 219–223.

[178] M. Bartoli, M. Giorcelli, C. Rosso, M. Rovere, P. Jagdale, Alberto Tagliaferro, Influence of Commercial Biochar Fillers on Brittleness/Ductility of Epoxy Resin Composites, *Appl. Sci.* 9 (2019) 3109-3112.

[179] S. Li, A. Huang, Y.-J. Chen, D. Li, L.-S. Turng, Highly filled Biochar/ultra-high molecular weight polyethylene/linear low density polyethylene composites

for high-performance electromagnetic interference shielding, *Composites* Part B 153 (2018) 277–284.

[180] B. Ashrafi, J. Guan, V. Mirjalili, Y. Zhang, L. Chun, P. Hubert, B. Simard, C. T. Kingston, O. Bourne, A. Johnston, Enhancement of mechanical performance of epoxy/carbon fiber laminate composites using single-walled carbon nanotubes, *Composites Science and Technology* 71 (2011) 1569–1578.

[181] T. H. Hsieh, A. J. Kinloch, A. C. Taylor, I. A. Kinloch, The effect of carbon nanotubes on the fracture toughness and fatigue performance of a thermosetting epoxy polymer, J Mater Sci 46 (2011) 7525–7535.

[182] T. Takeda, Y. Shindo, Y. Kuronuma, F. Narita, Modeling and characterization of the electrical conductivity of carbon nanotube-based polymer composites, *Polymer* 52 (2011) 3852-3856.

[183] J.K.W. Sandler, J.E. Kirk, I.A. Kinloch, M.S.P. Shaffer1, A.H. Windle, Ultra-low electrical percolation threshold in carbon-nanotube-epoxy composites, *Polymer* 44 (2003) 5893–5899.

[184] J. Sumfleth, X. C. Adroher, K. Schulte, Synergistic effects in network formation and electrical properties of hybrid epoxy nanocomposites containing multi-wall carbon nanotubes and carbon black, *J Mater Sci* 44 (2009) 3241–3247.

[185] M. Safdari, M. S. Al-Haik, Synergistic electrical and thermal transport properties of hybrid polymeric nanocomposites based on carbon nanotubes and graphite nanoplatelets, *Carbon* 64 (2013) 111-121.

[186] J. Li, P.-S. Wong, J.-K. Kim, Hybrid nanocomposites containing carbon nanotubes and graphite nanoplatelets, *Materials Science and Engineering A* 483–484 (2008) 660–663.

[187] A.Y. Malkin, Non-Newtonian viscosity in steady-state shear flows, *Journal of Non-Newtonian Fluid Mechanics* 192 (2013) 48–65.

[188] J.-H. Lee, C.-M. Um, I. Lee, Rheological properties of resin composites according to variations in monomer and filler composition, *Dental Materials* 22 (2006) 515–526.

[189] M. Abdalla, D. Dean, D. Adibempe, E. Nyairo, P. Robinson, G. Thompson, The effect of interfacial chemistry on molecular mobility and morphology of multiwalled carbon nanotubes epoxy nanocomposite, *Polymer* 48 (2007) 5662-5670.

[190] S. S. Rahatekar, K. K. K. Koziol, S. A. Butler, J. A. Elliott, M. S. P. Shaffer, M. R. Mackley, A. H. Windle, Optical microstructure and viscosity enhancement for an epoxy resin matrix containing multiwall carbon nanotubes, *J. Rheol.* 50 (2006) 599-610.

[191] S. Beun, C. Bailly, J. Devaux, G. Leloup, Rheological properties of flowable resin composites and pit and fissure sealants, *Dental Materials* 24 (2008) 548-555.

[192] K. W. Putz, M. J. Palmeri, R. B. Cohn, R. Andrews, L. C. Brinson, Effect of Cross-Link Density on Interphase Creation in Polymer Nanocomposites, *Macromolecules* 41 (2008) 6752-6756.

[193] O. Starkova, S.T. Buschhorn, E. Mannov, K. Schulte, A. Aniskevich, Creep and recovery of epoxy/MWCNT nanocomposites, *Composites: Part A* 43 (2012) 1212–1218.

[194] D. Matykiewicz, Biochar as an Effective Filler of Carbon Fiber Reinforced Bio-Epoxy Composites, Processes 8 (2020) 724-737.

[195] A. K. Chakraborty, T. Plyhm, M. Barbezat, A. Necola, G. P. Terrasi, Carbon nanotube (CNT)–epoxy nanocomposites: a systematic investigation of CNT dispersion, *J Nanopart Res* 13 (2011) 6493–6506.

[196] L. Guadagno, B. De Vivo, A. Di Bartolomeo, P. Lamberti, A. Sorrentino, V. Tucci, L. Vertuccio, V. Vittoria, Effect of functionalization on the thermo-mechanical and electrical behavior of multi-wall carbon nanotube/epoxy composites, *Carbon* 49 (2011) 1919-1930.

[197] L. Guadagno, L. Vertuccio, A. Sorrentino, M. Raimondo, C. Naddeo, V. Vittoria, G. Iannuzzo, E. Calvi, S. Russo, Mechanical and barrier properties of epoxy resin filled with multi-walled carbon nanotubes, *Carbon* 47 (2009) 2419-2430.

[198] K. Tao, S. Yang, J. C. Grunlan, Y.-S. Kim, B. Dang, Y. Deng, R. L. Thomas, B. L. Wilson, X. Wei, Effects of Carbon Nanotube Fillers on the Curing Processes of Epoxy Resin-Based Composites, *Journal of Applied Polymer Science* 102, (2006) 5248–5254.

[199] T. Zhou, X. Wang, X. Liu, D. Xiong, Influence of multi-walled carbon nanotubes on the cure behaviour of epoxy-imidazole system, *Carbon* 47 (2009) 1112-1118.

[200] S. G. Prolongo, M. R. Gude, A. Ureña, The Curing Process of Epoxy/Amino-Functionalized MWCNTs: Calorimetry, Molecular Modelling, and Electron Microscopy, *Journal of Nanotechnology* Article ID 420432, (2010) 1-11.

[201] N. Burger, A. Laachachi, M. Ferriol, M. Lutz, V. Toniazzo, D. Ruch Review of thermal conductivity in composites: Mechanisms, parameters and theory, *Progress in Polymer Science* 61 (2016) 1–28.

[202] H. Chen, V. V. Ginzburg, J. Yang, Y. Yang, W. Liu, Y. Huang, L. Du, B. Chen, Thermal conductivity of polymer-based composites: Fundamentals and applications, *Progress in Polymer Science* 59 (2016) 41–85.

[203] H. Im, J. Kim, Thermal conductivity of a graphene oxide–carbon nanotube hybrid/epoxy composite, *Carbon* 50 (2012) 5429-5440.

[204] Wen-Tai Hong, Nyan-Hwa Tai, Investigations on the thermal conductivity of composites reinforced with carbon nanotubes, *Diamond & Related Materials* 17 (2008) 1577–1581.

[205] A. Yu, P. Ramesh, X. Sun, E. Bekyarova, M. E. Itkis, R. C Haddon, Enhanced Thermal Conductivity in a Hybrid Graphite Nanoplatelet – Carbon Nanotube Filler for Epoxy Composites, *Adv. Mater.* 20 (2008) 4740–4744.

[206] S. Liu, V. S. Chevali, Z. Xu, D. Hui, H. Wang, A review of extending performance of epoxy resins using carbon nanomaterials, *Composites Part B* 136 (2018) 197-214.

[207] Z. Antar, J.F. Feller, H. Noël, P. Glouannec, K. Elleuch, Thermoelectric behaviour of melt processed carbon nanotube/graphite/poly(lactic-acid) conductive biopolymer nanocomposites (CPC), *Materials Letters* 67 (2012) 210–214.

[208] A. M. Poulose, A. Y. Elnour, A. Anis, H. Shaikh, S.M. Al-Zahrani, J. George, M. I. Al-Wabel, A. R. Usman, Y. S. Ok, D. C.W. Tsang, A. K. Sarmah, Date palm biochar-polymer composites: An investigation of electrical, mechanical, thermal and rheological characteristics, *Science of the Total Environment* 619–620 (2018) 311–318.

[209] B. Earp, J. Simpson, J. Phillips, D. Grbovic, S. Vidmar, J. McCarthy, C. C. Luhrs, Electrically Conductive CNT Composites at Loadings below Theoretical Percolation Values, Nanomaterials 9 (2019) 491-518.

[210] F. H. Gojny, M. H.G. Wichmann, B. Fiedler, I. A. Kinloch, W. Bauhofer, A. H. Windle, K. Schulte, Evaluation and identification of electrical and thermal conduction mechanisms in carbon nanotube/epoxy composites, *Polymer* 47 (2006) 2036–2045.

[211] J. O. Aguilar, J. R. Bautista-Quijano, F. Avilés, Influence of carbon nanotube clustering on the electrical conductivity of polymer composite films, *eXPRESS Polymer Letters* 4, (2010) 292–299.

[212] Z.A. Ghaleb, M. Mariatti, Z.M. Ariff, Synergy effects of graphene and multiwalled carbon nanotubes hybrid system on properties of epoxy nanocomposites, *Journal of Reinforced Plastics and Composites*, 36 (2017) 685-695.

[213] M. Havel, K. Behler, G. Korneva, Y. Gogotsi, Transparent Thin Films of Multiwalled Carbon Nanotubes Self-Assembled on Polyamide 11 Nanofibers, *Adv. Funct. Mater.* 18 (2008) 2322-2327.

Publications

V. Strongone, M. Bartoli, P. Vitthal Jagdale, R. Arrigo, A. Tagliaferro, G. Malucelli, Preparation and characterization of UV-LED curable acrylic films containing biochar and/or multiwalled carbon nanotubes: effect of the filler loading on the rheological, thermal and optical properties, *Polymers* 12, 796-811, 2020.

D. Duraccio, **V. Strongone**, M. G. Faga, F. Auriemma, F. D. Mussano, T. Genova, G. Malucelli, The role of different dry-mixing techniques on the mechanical and biological behavior of UHMWPE/alumina-zirconia composites for biomedical applications, *European Polymer Journal* 120, 109274-109282, 2019.

D. Duraccio, **V. Strongone**, G. Malucelli, F. Auriemma, C. De Rosa, F. D. Mussano, T. Genova, M. G. Faga, The role of alumina-zirconia loading on the mechanical and biological properties of UHMWPE for biomedical applications, *Composites Part B: Engineering* 164, 800-808, 2019.

Proceedings

V. Strongone, G. Malucelli, Biochar as promising carbon filler to functionalize UV-LED curable nanocoatings, Polychar 27 World Forum on Advanced Materials, Napoli, 14-17 October 2019.

V. Strongone, Preparazione e caratterizzazione di coatings funzionali contenenti filler carboniosi mediante UV-LED curing, Macrogiovani 2019, Napoli, 1-2 Luglio 2019.

V. Strongone, D. Duraccio, G. Malucelli, Synthesis and characterization of UV-LED curable nanocomposite coatings, XXIII Convegno Nazionale dell'Associazione di Scienza e Tecnologia delle Macromolecole, Catania, 9-12 Settembre 2018.

D. Duraccio, **V. Strongone**, A. Fioravanti, G. Malucelli, Hybrid piezoelectric films functionalized with ZnO nanostructures and cellulose nanocrystals, XXIII Convegno Nazionale dell'Associazione di Scienza e Tecnologia delle Macromolecole, Catania, 9-12 Settembre 2018.